SYNTHESIS OF GRAPHENE-BASED NANOMATERIALS AND THEIR OPTOELECTRONIC APPLICATIONS

LAI SIN KI

Ph.D

The Hong Kong Polytechnic University
2018

The Hong Kong Polytechnic University

Department of Applied Physics

Synthesis of Graphene-Based Nanomaterials and Their Optoelectronic Applications

Lai Sin Ki

A thesis submitted in partial fulfillment of the
requirements for the degree of Doctor of Philosophy

July 2017

Certificate of originality

I hereby declare that this thesis is my own work and that, to the best of my knowledge and belief, it reproduces no material previously published or written, nor material that has been accepted for the award of any other degree or diploma, except where due acknowledgement has been made in the text.

________________________ (Signed)

_______Lai Sin Ki_______ (Name of candidate)

Abstract

Carbon nanomaterials have, for a long history, been intensively applied in electronics and optoelectronics due to their high functionality, stability and the abundance of raw material. They span from the 2D graphene, to the 1D carbon nanotubes and the quasi-0D carbon quantum/nano- dots, including fullerenes. The bandgap in the above nanomaterials vary from zero in the semi-metallic graphene to a bandgap deep into the UV region for the 0D graphene quantum dots. The wide range of bandgap and electrical properties of carbon nanomaterials through dimension reduction may allow selective detection for desirable spectral range of light and optimization in the figures of merit of photodetectors respectively, which make carbon nanomaterials promising for photo-sensing application.

In this project, graphene oxide (GO) has been applied to demonstrate broadband photodetection from near infrared to deep ultraviolet. The bandgap of the multi-layer GO nanosheets could be gradually varied by thermal annealing. This was achieved by the removal of oxygen functional groups and restoration of the sp^2 hybridization in graphene oxide progressively by controlling the annealing temperature. Electronic properties of the GO could be tuned simultaneously during annealing, which could allow the performance of the photodetectors to be optimized

through a trade-off between the magnitude of dark current and carrier mobility, in which the detectivity and response time of the device would be affected respectively. A satisfactory responsivity in the order of mA^{-1} and fast response time in the range of ms were obtained from the devices with an active layer thickness of ~70 nm.

The graphene quantum dots (GQDs) were chemically functionalized with solution-processable organic conducting polymers. The conducting polymer-GQDs composite showed an enhanced photocurrent by an order of magnitude and also a faster response time as compared to non-functionalized GQDs. Under observation at high magnification, the conducting polymer was revealed to connect the GQDs effectively which could facilitate conduction of charge carriers among the GQDs via the high mobility conducting polymer instead of a greatly hindered electrical transport through hopping of charge carriers among quantum dots in the non-functionalized case. This enables carriers to be harvested more effectively in the composite to give larger photocurrent and faster response time.

The heterostructure of large-area graphene with uniformly distributed graphitic carbon nitride nanosheets with ~200 nm in lateral size exhibited synergistic effect for efficient near ultraviolet photodetection and demonstrated a large photocurrent that could also be useful for photoelectrochemcial applications where efficient photocurrent generation is also highly demanded. When heterostructure is adopted, the band alignment between the two components determine the charge transport across the interface. It helps the separation of electron-hole pairs which contribute to more efficient photocurrent generation and thus is of fundamental importance. This is distinctly different from single-component photodetector where photocurrent is usually found only at the metal-semiconductor junction where Schottky barrier may be formed and barrier property is the commonly investigated subject in that case. The charge transfer property at the graphene/carbon nitride interface was systematically analyzed in our devices to elucidate the electrical conduction process for photodetection.

List of Publications

1. S. K. Lai, L. Tang, Y. Y. Hui, C. M. Luk and S. P. Lau, A deep ultraviolet to near-infrared photoresponse from glucose-derived graphene oxide, J. Mater. Chem. C, 2014, 2, 6971.
2. S. K. Lai, C. M. Luk, L. Tang, K. S. Teng and S. P. Lau, Photoresponse of polyaniline-functionalized graphene quantum dots, Nanoscale, 2015, 7, 5338.
3. P. Tian, L. Tang, J. Xiang, Z. Sun, R. Ji, S. K. Lai, S. P. Lau, J. Kong, J. Zhao, C. Yang and Y. Li, Solution processable high-performance infrared organic photodetector by iodine doping, RSC Adv., 2016, 6, 45166.
4. S. K. Lai, C. Xie, K. S. Teng, Y. Li, F. Tan, F. Yan and S. P. Lau, Polymeric carbon nitride nanosheets/graphene hybrid phototransistors with high responsivity, Adv. Opt. Mater., 2016, 4, 555.
5. X. Guo, L. Tang, J. Xiang, R. Ji, K. Zhang, S. K. Lai, J. Zhao, J. Kong and S. P. Lau, Solution processable organic/inorganic hybrid ultraviolet photovoltaic detector, AIP Adv., 2016, 6, 055318.
6. F. Qian, X. Li, L. Tang, S. K. Lai, C. Lu and S. P. Lau, Potassium doping: tuning the optical properties of graphene quantum dots, AIP Adv., 2016, 6, 075116.
7. Y. Cai, L. Tang, J. Xiang, R. Ji, S. K. Lai, S. P. Lau, J. Zhao, J. Kong and K. Zhang,

High performance ultraviolet photodetectors based on ZnO nanoflakes/PVK heterojunction, Appl. Phys. Lett., 2016, 109, 073103.

8. F. Tan, T. Li, N. Wang, S. K. Lai, C. C. Tsoi, W. Yu and X. Zhang, Rough gold films as broadband absorbers for plasmonic enhancement of TiO_2 photocurrent over 400-800 nm, Sci. Rep., 2016, 6, 33049.
9. Y. Wang, R. Fullon, M. Acerce, C. E. Petoukhoff, J. Yang, C. Chen, S. Du, S. K. Lai, S. P. Lau, D. Voiry, D. O'Carroll, G. Gupta, A. D. Mohite, S. Zhang, H. Zhou and M. Chhowalla, Solution-processed MoS_2/organolead trihalide perovskite photodetectors, Adv. Mater., 2017, 29, 1603995.
10. F. Qian, X. Li, L. Tang, S. K. Lai, C. Lu and S. P. Lau, Selenium quantum dots: preparation, structure and properties, Appl. Phys. Lett., 2017, 110, 053104.
11. X. Guo, L. Peng, L. Tang, J. Xiang, R. Ji, K. Zhang, C. M. Luk, S. K. Lai, R. Wan, Y. Duan and S. P. Lau, Large-area uniform electron doping of graphene by Ag film, AIP Adv., 2017, 7, 045209.
12. Y. Li, Z. Hu, S. Lin, S. K. Lai, W. Ji and S. P. Lau, Giant anisotropic Raman response of encapsulated ultrathin black phosphorus by uniaxial strain, Adv. Funct. Mater., 2017, 27, 1600986.

Acknowledgements

Sincere gratitude would have to be given to my supervisor, Prof. S. P. Lau, for he has provided high degree of freedom to students, and with great endurance and patience, allowing students not only to pursuing greatness in intellectual studies, but also in different aspects of life. I would also like to give my heartily gratitude to Ms. Ng Sheung Mei Theresa and Mr. Wong Hon Fai, for their assistance, technical support and useful discussions. They always provided help in for example, improving the equipment, and helped tackled difficulties I encountered in my work, without them I would not have been able to continue my work with less obstacles. Special thanks are given to Prof. M. Chhowalla, for his valuable supervision during my visit to Rutgers University.

Many other people have provided assistance and support during my study, some of them include Prof. Tang Libin, Prof. Teng Kar Seng, Dr. Li Yanyong, Dr. Lin Shenghuang, Dr. Hui Yeung Yu Edwin, Dr. Luk Chi Man Simon, Dr. Chui Ying San Wasili, Ms. Yau Hei Man, Mr. Rogee Lukas, Dr. Chan Ngai Yui Vincent, Dr. Lui Hardy, Dr. Wong Terrence, Dr. Lu Wei. Thanks for their help or technical support.

Last but not least, I have to thank my family, including my parents, siblings and relatives, who had provided unlimited support to me at all times.

Table of Contents

List of Figures

List of Tables

Chapter 1 Introduction

1.1 Background and motivation

Carbon nanomaterials have, for decades, been attracting intensive attention from the scientific community. Key breakthroughs include the discovery of C60 fullerene in 1985 [1] and macroscopic synthesis of carbon nanotubes in 1991 [2]. C60 fullerene is now widely adopted in solution-processed organic solar cells as electron acceptor due to its high electron affinity [3]. Carbon nanotubes have been used as high-strength material [4], and investigated as interconnects in integrated circuit owing to its high break-down current density [5]. The renaissance of carbon nanomaterials continued through the first successful isolation of graphene, a monolayer of graphite, in 2004 [6], which also opened up the popular field of 2D materials study since then.

Graphene was first obtained by mechanical exfoliation, which is not a scalable production method and the yield is low. People then turned to explore other ways that could produce graphene in large amount. This leads to the development of the modified Hummer's method [7, 8]. In this method, harsh chemistry is employed to oxidize the graphite powders. The oxygen-containing functional groups adhere onto the basal plane enlarge the interplanar distance of graphite. The oxygen functional groups are hydrophilic in nature, thus the layers repel each other and readily dispersed in water, producing monolayer GO with good dispersability. GO can be converted to graphene by chemical reduction using e.g. hydrazine. This chemical route enables the production of graphene in gram-scale at a time, but the graphene obtained suffer from a large number of defects.

Graphite has a small band overlap of ~40 meV, and become zero bandgap as it evolves to single layer graphene [9]. Upon chemical treatment, the resulting graphene oxide is insulating [10]. This shows that chemical modification is one effective way to tailor the band structure of graphene.

The absence of bandgap in graphene has restricted its application as channel in field effect transistors, and also in optoelectronics. Another approach to open a band gap is to further increase the quantum confinement effect in graphene, since more boundary conditions would lead to more forbidden states in energy. This intuitively leads to the study of graphene nanoribbons [11], and subsequently, GQDs. In particular, GQDs can be mass-produced in green and facile way to get photoluminescence (PL) that is not found in graphene and the PL is strong enough to be detected without the need of confocal setup [12]. This brought graphene-based materials into the field of optoelectronics.

In addition to band gap engineering through dimension reduction, bandgap of carbon nanomaterials can also be chemically modified using numerous methods to provide them with even higher flexibility. Chemical functionalization of carbon with other elements like oxygen, nitrogen, boron, phosphorus etc. have been widely reported. Incorporation of other elements disrupt the sp^2 coordination in graphene which inevitably opens a band gap in graphene. The bandgap in chemically modified graphene depends on the sp^2 domain size retained in graphene, and therefore can also be tuned for a wide range.

The large variation of electrical properties in carbon nanomaterials also allow the design of heterostructure based on all-carbon nanomaterials that can result in a synergistic effect in photo-detecting application. Graphene, with its unique quantum property where the electrons behave like Dirac fermions, does not have appreciable selectivity in optical absorption from infra-red to ultraviolet. Moreover, the high conductivity makes graphene having an extremely low on-off ratio upon optical excitation which also hinder its application in photodetection. However, it can complement discretized quantum dots and nanosheets to mitigate the ineffective charge conduction by hopping in quantum dots and nanosheets that are not compactly packed.

Another popular carbon nanomaterials that has caught special attention in photochemical reaction is polymeric graphitic carbon nitride [13]. It also has a layered structure with atomic planes stacked by van der Waals attraction. It exhibits photoluminescence like GQDs but with a bandgap that lies just outside of the ultraviolet regime, thus make it a good candidate as the active material in visible-blind ultraviolet photodetectors if further quantum confinement is employed to increase its bandgap for an appropriate extent, which is promising due to its layered structure.

In view of the wide range, tunable band gap in graphene-based nanomaterials, which also implies tunable electrical and optical properties, in this thesis, focus is placed on the optoelectronic application of graphene-related nanomaterials, specifically, for the application of photodetectors. The capability of tailoring the carbon nanostructures to fulfill the need from broadband photodetection to selective detection in certain frequency range were revealed by the use of various types of photodetectors and field effect transistors made from carbon nanostructures in this project. Together with other intriguing properties of carbon materials, including the ease and low cost of fabrication, rich chemistry, high stability both to oxygen and chemicals, it is anticipated that the carbon nanostructures are suitable candidate for electronics and optoelectronics.

Photodetectors are widely used in our daily life. They detect photons ranging from radio wave to X-ray and gamma ray in the electromagnetic spectrum. Photodetector array, which contains numbers of photodiode, each representing a pixel and arranged like elements in a matrix, are employed to provide images. Photodetectors find applications in digital cameras, video recorders, satellites or space telescopes that rely on the detection of X-ray or far-infrared, fiber-optic communications for data transmission, retina prosthesis, infrared video camera for night vision, thermography, receiver in remote controls, pollution detection using UV detectors, IR sensitive motion detectors like those in automatic doors, collision detectors in cars etc. [14, 15]. Downsizing or miniaturization of photodetectors is also in huge demand [16], with more photodetectors being packed in each unit space in the hope to increasing the resolution of an image and reducing the power consumption of the array. However, the reduction in active area in each pixel would reduce the power of light falling onto each pixel which in turn reduce the photocurrent, therefore, the responsivity of a photodetector, which measures photocurrent per unit light power, is crucial when evaluating the performance of photodetectors. Therefore, one of the objectives of the project is to obtain photodetectors with high responsivity.

High-speed photodetectors are essential for fiberoptic communications, requirement for sensitivity is less important in this field. In fiberoptic communications, infrared signal with high modulation frequency in GHz is used as the information carrier. InGaAs PIN (p-doped/intrinsic/n-doped InGaAs) photodiodes are used to detect the GHz signal.

Detectivity is also an important parameter to evaluate the performance of photodetectors. It reflects in part the signal-to-noise ratio of photodetectors, which cannot be known by simply knowing the responsivity of the device. A device with a high responsivity could have a low detectivity due to a large dark current, as we will see in later section of the thesis. Similar to a minimum on/off ratio of 10^4 required for a practical field effect transistor (an electrical switch), an on/off ratio upon light on/off in a photodetector (an optical switch), must be several orders of magnitude for practical consideration [15].

Graphene-based nanomaterials could be tuned from semimetals, to semiconductors and insulators, such that the dark current of the photodetectors made from graphene-based nanomaterials can be varied. This allows us to optimize the responsivity and detectivity in photodetectors based on graphene nanomaterials, as the two parameters could have a trade-off relationship. This flexibility in graphene-based nanomaterials has motivated us to study the graphene-based nanomaterials for photodetector application.

1.2 Scope of this project

This project involves the synthesis of different types of graphene-based nanomaterials, including graphene, GO, GQDs and graphitic carbon nitride. Chemical modifications were carried out in GO and GQDs, where thermal annealing was performed to partially reduce the GO and organic conducting polymer was coupled to GQDs to form composite. The above graphene-based nanomaterials were applied for photodetectors or phototransistors. Performance of devices were evaluated.

In Chapter 2, properties of different graphene-based nanostructures, figure of merits of photodetectors and photosensing mechanisms are described.

In Chapter 3, experimental details are described, including X-ray diffraction, optical absorption spectroscopy, photoluminescence and Raman spectroscopy.

In Chapter 4, synthesis of glucose-derived multilayer GO nanosheets is introduced. The partial reduction of GO is described. Fabrication and performance evaluation of GO-based photodetectors are described.

In Chapter 5, synthesis of the polyaniline-GQDs composite is described. Then photodetectors based on the composite are compared with GQDs-only devices to illustrate the role of polyaniline in the composite.

In Chapter 6, the synthesis of polymeric graphitic carbon nitride and chemical vapor deposition of graphene are described. Heterostructure of graphene and carbon nitride nanosheets are employed as phototransistor with evaluation in the transport process in the devices given in this section.

In Chapter 7, the works in this project are concluded and future works are discussed.

Chapter 2 Properties of graphene-related nanomaterials, parameters and mechanisms of photodetectors

In this chapter, properties and synthesis of the graphene-related nanomaterials that have been utilized in this project are described. These materials include graphene, GO, GQDs and graphitic carbon nitride.

2.1 Basic properties of graphene-based nanomaterials

Graphene is a monolayer of graphite that consists of an atomically flat plane of hexagonally packed carbon atoms. It was first successfully isolated in 2004 [6], which was also the first 2D material realized experimentally. In principle, 2D materials can be obtained in any bulk crystals that have atomic layers held together by van der Waals (vdW) force and are stacked along same direction, taken as the c-axis. The weak vdW force renders the crystals easily to be cleaved along the c-axis with a small external force. Mechanical exfoliation was utilized to obtain graphene [6], which basically is the thinning of bulk graphite powders repeatedly using tape until the thicknesses of which reach monolayer. The adhesiveness of the tape serves as the external force. Up to date, apart from graphene, many other 2D materials had also been obtained by such method. One most representative family is the transition metal dichalcogenides (TMD) including MoS_2, $MoSe_2$, $MoTe_2$, WS_2, WSe_2 etc. In this project, we focused on graphene and its related nanomaterials, that have become actively investigated throughout the world since the discovery of graphene.

Many intriguing properties have been discovered in graphene. One is the ballistic transport. The low energy carriers near the Dirac point in graphene can be represented by (quasi-)massless Dirac fermions [17, 18]. This 'massless' property gives rise to the unique band structure of graphene, which is a linear dispersion relation with distinctive conical shape energy bands in the reduced space. (Bilayer and multilayer graphene have parabolic energy bands, this shows the uniqueness of monolayer graphene.) Electrons near the Dirac point in graphene can be described as massless quasi-particles that are screened from phonon scattering and travel in a constant effective Fermi velocity (v_F) of 10^6 ms^{-1} [18]. As a consequence, an intrinsic mobility as high as 10^5 cm^2 V^{-1} s^{-1} was theoretically feasible in graphene [18], and a mobility of 10^4 cm^2 V^{-1} s^{-1} was experimentally measured [19], which is much higher than that of silicon (10^2-10^3 cm^2 V^{-1} s^{-1}).

The existence of two inequivalent valleys at the *K* and *K'* Brillouin zone corners of graphene, arising from the time reversal symmetry that require opposite spin of electrons in the two valleys [20], can suppress intervalley scattering of electrons, which catch attention for a new valley degree of freedom (DoF) for carriers in graphene. The valley DoF is in analogous to the charge and spin DoF of electrons, thus create possibility for valley DoF as a new information carrier [21, 22]. Valley polarization, an imbalance in the concentration of carriers in inequivalent valleys, is necessary for this purpose. Though later it has been found that by optical selection rules (optical circular dichroism) due to broken inversion symmetry, valley polarization can be conveniently obtained in monolayer TMDs using circularly polarized light in the visible or near infrared regime, which graphene with its lack of bandgap is less ideal for using optical excitation to probe valley polarization. TMDs also have additional strong spin-orbit coupling/interaction (SOI) arising from *d*-orbital of the transition metal that is missing in graphene. The SOI gives rise to valley splitting (electrons in splitted valleys have opposite spin), where the B excitons in the higher energy valley (in holes' perspective) has proven to be robust (have long lifetime from the evidence that the photoluminescence from B excitons could be observed without using ultrafast spectroscopy) due to clogged relaxation pathway (to satisfy simultaneously a flip in both the valley and spin indexes), this may give rise to even higher DoF in valley polarization in TMDs. Nonetheless, graphene gave a kickstart of the field of valleytronics in 2D materials. (Note that the monolayer-ness of graphene and TMDs are crucial in the above discussion since their monolayers have broken inversion symmetry that is essential for valley contrasting Berry curvature, magnetic moments and optical circular dichroism [23]. Inversion symmetry is preserved in bilayer graphene and TMDs.)

Graphene is unique in the way that it has been demonstrated to absorb a constant value of ~2.3 %, defined by the fine-structure constant (α), over a broad range of the EM spectrum, from visible light to the far-infrared [24]. This makes graphene particularly valuable for manipulating and sensing terahertz, far- and mid-infrared radiations, where materials suitable for these ranges are in increasing demand [25, 26], due to the need to expand the bandwidth in wireless communication to accommodate the ever-increasing amount of wireless data transmission, and to enable a higher speed of wireless data transmission by using waves with higher frequency. The terahertz regime has been receiving a lot of attention for being used for future wireless communication, which at the present is utilizing the GHz microwave frequency. Terahertz covers from 0.3 to 30 THz, which converts to an energy of about 1-100 meV. This low energy means the heavily investigated semiconducting materials for detectors are not suitable for terahertz, in addition, detecting mechanisms different from those familiarly known for the near infrared and optical frequency have to be applied [27]. To utilize this range, reliable sources, detectors, modulators and antennas for the terahertz must be developed. Graphene terahertz detectors and modulators have been demonstrated which revealed the potential of graphene for terahertz technology [27-28].

Many of the small band gap (<1 eV) or metallic (with band overlap) 2D materials are unstable in the ambience. For example, the few-layer $MoTe_2$, WTe_2, Bi_2Te_3, $TiSe_2$, $NbSe_2$, TaS_2 and phosphorene are known to readily react with oxygen in the air [29]. The oxidized sheets have completely different electrical and optical properties with their pristine form, and that the oxidation is non-reversible, unlike GO. On the other hand, larger band gap 2D materials, like hexagonal boron nitride, MoS_2, WS_2 tends to be relatively more stable in the ambience. In this aspect, graphene stands out as a stable zero band gap 2D material. Therefore, it has huge potential for applications for transparent and flexible electrodes.

Graphene also provides a platform for chemical functionalization that could alter its electrical properties in controllable way. Unlike pristine 2H phase TMDs where the basal plane is largely chemically inert that render covalent functionalization challenging [30], graphene has a unique degree of freedom of the reversible change between sp^2 and sp^3 hybridization in the carbon atoms, such that it is feasible to create additional covalent bond without damaging the carbon basal plane by not breaking the C-C sigma bonds. The sp^3 bonding allows carbon atom bonds to different heteroatoms and functional groups [31]. In particular, the solution-processed graphene oxide has numerous polar functional groups adhered onto the basal plane that allow immobilization of electroactive species like dyes, DNA, enzymes, through covalent or non-covalent bonding, which promote the use of graphene-based materials for biosensors, photo- and electro-catalysis [32].

Among different forms of chemically modified graphene, GO has caught special attention. GO is an intermediate product created during the chemical exfoliation of graphite, which was developed to achieve large-scale mass production of graphene. However, it was found that this intermediate product could be useful on its own. It has distinct electronic properties from graphene. It is insulating and possesses a band gap [10]. In GO, some of the sp^2 bonds in graphene change into sp^3 hybridization due to the addition of functional groups to the carbon atoms like the epoxide (-O-), hydroxyl (-OH), carbonyl (=O), and carboxylate (-OOH) groups. Different degrees of reduction were performed on GO by various approaches, like varying the duration of chemical reduction and the temperature of thermal annealing. Reduction eliminates some of the oxygen functional groups to restore the sp^2 bonding, which would also increase the electrical conductivity due to the resultant delocalized electron in the p_z orbital in the sp^2 hybridization. The bandgap decreases gradually with the degree of reduction [33]. Control of reduction enables the work function of GO to be tuned [34] and could potentially be applied for optimized transport layer in photovoltaics [35]. Degree of reduction in GO is also related to interplanar distance in the vacuum-filtrated film of GO due to the varying density of the hydrophilic functional groups that would affect interlayer coupling in GO. This property has also been shown to have great potential for separation of ions in water based on GO membranes [36].

GQDs have also been actively investigated in the progress to opening a band gap in graphene. GQDs typically have diameters less than 10 nm, and usually produced by solution-based methods, for example, by electrochemical route using a graphite electrode or powders [37], or hydrothermal cutting of GO nanosheets [12]. The strong confinement of electron waves in three spatial dimensions leads to a change in the allowed energy states of the electrons, more forbidden energy states are induced in the graphene. The consequence of which is the appearance of a bandgap that does not exist in the 2D confinement in graphene. One intriguing property found in GQDs after bandgap opening is the emergence of photoluminescence. Photoluminescence with high quantum yield is essential in applications like light emitting diodes, bioimaging, anticounterfeiting etc. As a result, GQDs opened up many interesting and useful applications in the field of optoelectronics for graphene materials. The solution-based synthesis also renders the chemical engineering of GQDs more convenient. Numerous reports regarding the doping of GQDs with different elements like nitrogen, oxygen, phosphorus, boron can be found, and have been reported to induce changes in the photoluminescence properties of GQDs [38].

Another graphene-based nanomaterial is the graphitic carbon nitride (g-C_3N_4) nanosheets. The polymeric form of g-C_3N_4, which is highly defective with a C/N ratio considerably deviates from 3/4, is intensively investigated in recent years, due to the discovery of its high photochemical hydrogen evolution activity, especially under visible light when compared to TiO_2, the conventional material used in water splitting [39-41]. g-C_3N_4 also has a layered structure, with a bandgap of ~2.7 eV, which lies just outside of the ultraviolet region. The layered structure implies that it could be readily exfoliated to induce quantum confinement to increase its band gap in order to apply the material in carbon-based solar-blind ultraviolet photodetectors.

2.2 Figures of merit of photodetectors

Photodetectors are evaluated by several figures of merit including the responsivity, -3dB bandwidth, noise current, specific detectivity, noise equivalent power, rise/fall time, linear dynamic range and quantum efficiency [42, 43]. These parameters are defined in this section.

Responsivity

Responsivity (R) of a photodetector measures the photocurrent (I_{Ph}) per unit light power (P) falling onto the device active area. R has the unit AW^{-1}.

$$R = \frac{I_{Ph}}{P} = \frac{I_{light} - I_{dark}}{W * A}$$

where I_{light} is the current when light is on and I_{dark} is the dark current of the device. W is the intensity of the light source, A is the active area of the device.

Noise equivalent power

Noise equivalent power (*NEP*) measures the minimum detectable light power, which is defined as the light power that gives the signal-to-noise ratio (S/N) equals unity (0 dB), when the bandwidth (B) is 1 Hz [42]. The bandwidth has to be fixed since S/N is a function of bandwidth. Bandwidth is related to the integration time (τ_i) by

$$\mathrm{B} = \frac{1}{2\tau_i}$$

For example, if the S/N measured over an integration time of 0.5 s equals α, the S/N obtained over 50s equals $\sqrt{100}\alpha = 10\alpha$ for the same light intensity [44].

It can be written as [45]

$$NEP = \frac{I_{noise}}{R} = \frac{\sqrt{\overline{I_{noise}}^2}}{R} \qquad [\frac{A/Hz^{1/2}}{A/W}]$$

where I_{noise} is the noise current, which is the root mean square of the fluctuation in current, when bandwidth is limited to 1 Hz [42]. R is responsivity.

-3dB Bandwidth

The -3dB bandwidth (f_{-3dB}, in unit of Hz) is defined as the frequency of light modulation at which the photo-current/voltage of the device falls by -3dB (~0.707 for

V and I, or ~0.5 if output power is measured instead, using the relations $P = I^2R = V^2/R$) of the photo-current/voltage under continuous wave [46]. It can be estimated by the value $0.35/\tau_r$, where τ_r is the 10-90% rise time of the device.

The -3dB bandwidth is limited by the carrier transit time and the characteristic RC constant according to the relation [46]:

$$\frac{1}{{f_{-3dB}}^2} = \frac{1}{{f_t}^2} + \frac{1}{{f_{RC}}^2}$$

where f_t is the carrier transit time-limited bandwidth given by

$$f_t = \frac{3.5}{2\pi t_{tr}};\ t_{tr} = \frac{d}{\mu E} = \frac{d^2}{\mu V}$$

where t_{tr} is the carrier transit time, and is related to the carrier mobility (μ). d is the average distance travelled by carriers, E is the E-field in the device.

And f_{RC} is the RC-limited bandwidth, given by

$$f_{RC} = \frac{1}{2\pi RC}\ ,$$

R is the total series resistance, including series resistance of photodiode, contact resistance, load resistance etc. C is the capacitance of photodiode.

<u>Rise/fall time</u>

The rise (fall) time of the photodetectors is defined as the time interval for the response to rise (fall) from 10% (90%) to 90% (10%) of the saturated photo-current/voltage with respect to the dark current.

<u>Noise current</u>

Noise current originates from statistical fluctuation in the number of photons and electrons, and the random motion of electrons [47]. First factor gives rise to shot noise, second factor give rise to the thermal Johnson-Nyquist noise [45, 48]. These two noises are common in all circuits [49]. Other noises like the flicker noise (1/*f* noise) and popcorn noise may also present [48], which could not be neglected.

Thermal noise always exists regardless of applied voltage as it is related to random thermal vibration of electrons within the conductor at non-zero temperature. Under zero bias, the thermal (Johnson-Nyquist) noise (S_T) dominate [50]. It is given by

$$S_T = \sqrt{\frac{4k_BTB}{R_D}} \qquad [\mathrm{A/Hz^{1/2}}]$$

where k_B is the Boltzmann constant, T is the temperature, B is the bandwidth in measurement, R_D is the load resistance.

The shot noise (S_S) is a quantum effect that is related to the particle nature of photons and electrons such that the number of photons impinging the device under a 'constant' light intensity and number of electrons being injected into the device under a 'constant' bias are statistical processes. Shot noise describe the resultant photo- and dark current fluctuations. Photon out-fluxing are discrete, independent and random events and thus describe by the Poisson distribution. Shot noise comes from the background (the surroundings) and from the dark current. Shot noise is given by [51]

$$S_S = \sqrt{2q\bar{I}B} \qquad [\mathrm{A/Hz^{1/2}}]$$

where q is elementary charge, $\bar{I}$ is the average current, B is bandwidth.

Considering only the above two noise components, the noise current is expressed as

$$I_{noise} = \sqrt{\overline{\imath_{noise}{}^2}} = \sqrt{{S_S}^2 + {S_T}^2}$$

Flicker noise is caused by traps near the interfaces, especially significant for field effect transistors that have short channel.

Specific detectivity

Specific detectivity (D*) allows comparisons of the weak light detection capability of photodetectors that have different active area and bandwidth, which are not normalized in NEP. The unit is cmHz$^{1/2}$W^{-1}.

$$D^* = \frac{\sqrt{AB}}{NEP} = \frac{R\sqrt{AB}}{I_{noise}}$$

where A is the active area of device, B is the bandwidth.

If the shot noise from the dark current is the major noise contribution that limit the detectivity, below representation applies

$$D^* = \frac{R}{\sqrt{2qJ_{dark}}}$$

where R is responsivity, J_{dark} is the dark current density.

Linear dynamic range

Linear dynamic range (LDR) measures the light intensity range (in dB) in which the responsivity of the photodetectors remains constant. The responsivity of photodetectors ideally should be independent of light intensity. It is expressed as [46]

$$LDR = 20\log_{10}\frac{W_{dev}}{W_{min}}$$

where W_{min} is the lowest light intensity used in the measurement, W_{dev} is the light intensity at which the linear relationship of photocurrent vs light intensity starts to deviate.

Quantum efficiency

There are the internal quantum efficiency (IQE) and external quantum efficiency (EQE). The IQE describes the ratio of the number of charge carriers detected over the number of photons absorbed by the device. Photons that are transmitted through and reflected from the device are not included in the denominator in the calculation of IQE. To obtain IQE, the power of light over devices' active area, reflectance and transmittance of the devices have to be known. EQE describes the ratio of the number of charge carriers detected over the number of photons impinging the device. To obtain EQE, the power of light over devices' active area have to be known.

2.3 Photosensing mechanism

There are a number of mechanisms that have been analyzed to date for giving rise to photocurrent/voltage, they include the photovoltaic, photoconductive, photothermoelectric, bolometric, photogating and photoelectric effect.

Photovoltaic effect

The photovoltaic effect occurs in structures that have a built-in electric field, that helps in separating the photo-generated electron-hole pairs and gives rise to photocurrent [43, 45]. The built-in E-field establishes as a result of a large difference in Fermi level of the materials forming the junction. Typical example is a p-n junction. The depletion region formed at the p-n interface in equilibrium upon contact is where the built-in E-field exists. Magnitude of this equilibrium internal E-field can be changed using an external E-field. It would be reduced under forward bias, and enlarged under reverse bias. The build-in E-field supports the conduction of minority carriers in the semiconductor, which give rise to a non-zero current (dark current in a photodiode) under reverse-biased condition in a diode. Photodetectors that utilize a p-n junction are called photodiodes. Solar cells are a special case of photodiodes, that operate at zero bias. High IQE and very short response time can be achieved if the thickness of active layer is optimized such that the device is fully depleted, together with the satisfaction that the recombination lifetime of electron and hole are larger than the respective carrier transit time [42]. EQE and gain are capped at unity for a photodiode.

For 2D materials-based photodetectors that utilized photovoltaic effect, different device architectures can be found to achieve a built-in E-field, including local chemical doping, split gate, Schottky junction with metals [52].

Photoconductive effect

The photoconductive effect involves only one carrier type for conduction (unipolar), unlike photovoltaic effect where both carrier type conducts. The carrier type not involved in conduction is trapped [42]. If the lifetime of the un-trapped carrier type exceeds its transit time, it can circulate between the electrodes under electric bias many times within the recombination lifetime determined by the long lifetime of the trapped carriers, which can lead to photoconductive gain. Bias voltage must be applied to operate a pure photoconductor, and generally not suitable for high speed application. Phototransistors have been reported to exploit the photoconductive effect [42].

Photothermoelectric effect

The photothermoelectric effect is produced by light-induced temperature gradient of the carriers across an interface between two materials that have different Seebeck coefficients. The temperature gradient of hot carriers results in a photovoltage or photocurrent. Junction with different Seebeck coefficients on two sides can be achieved by different doping level, e.g. in a p-n junction, or partial dual gate-bottom gate configuration.

Seebeck coefficient (S) is related to the conductance (G) of the material by the Mott equation [53],

$$\mathrm{S} = -\frac{\pi^2 k^2 T}{3q}\frac{1}{G}\frac{dG}{dV_G}\frac{dV_G}{dE}\bigg|_{E=E_F}$$

The photocurrent/voltage generated from photothermoelectric effect is

$$\mathrm{V}_{PTE} = \mathrm{I}_{PTE}\mathrm{R} = (S_2 - S_1)\Delta T$$

where R is the resistance, ΔT is the temperature difference between the hot carriers across the junction.

Taking the heat flow as a radial wave, we have [53],

$$\kappa 2\pi t\Delta T = P\alpha$$

where κ is the thermal conductivity, t is the thickness of the material, P is the incident light power, α is the absorption coefficient, thus allows ΔT across the junction to be estimated.

Photothermoelectric effect in graphene

Photothermoelectric effect is sometimes considered an undesirable photo-effect, due to its slow response and low efficiency [54], especially for devices that are intended to exploit other photosensing mechanisms like photovoltaic and photoconductive effect. Nonetheless, this photo-effect is believed to be significant for graphene-based devices since graphene has strong electron-electron interaction, photoexcited electron–hole pairs lead to ultrafast (~10–50 fs) heating of the carriers in graphene [52]. Furthermore, graphene has a small electron heat capacity and weak electron-phonon interaction, which ensure a large change in electron temperature under illumination and little heat loss from electrons from electron-phonon scattering respectively.

Chapter 3 Experimental and Characterization Methods

3.1 Synthesis of various graphene-based nanomaterials

3.1.1 Synthesis of glucose-derived graphene oxide nanosheets

Thermal decomposition of glucose by hydrothermal method was employed to synthesize graphene oxide (GO) nanosheets [55, 56]. Anhydrous glucose powders (Sigma Aldrich) were dissolved in deionized (DI) water. In typical synthesis, 0.5 M glucose solution was used. 40 ml of the solution was poured into a 50 ml Teflon-lined autoclave. The autoclaves were heated at 180 ^{o}C for 3 – 4 hours. The vessels were cooled naturally to room temperature before they were opened. GO nanosheet with thickness of 20-40 nm was found at the solution-air interface. The GO film was continuous over the entire interface, limited only by the diameter of the vessels used in the experiment. It is thus expected that a larger area of the nano-thickness GO is possible by using vessels with larger diameter. Glass slides were used to retrieve the GO, which was then transferred several times to DI water to wash the nanosheet, and was finally transferred to desired substrate, then dry in air. Thickness of GO can be varied by changing any one of the followings: the duration of hydrothermal process, hydrothermal temperature and concentration of glucose solution.

3.1.2 Microwave synthesis of graphene quantum dots

Anhydrous glucose powders were dissolved completely in DI water in 11 wt% concentration. 5 ml of the solution was transferred to a glass vessel, and closed with a rubber cap. It was then put into the microwave reactor. The vessel was heated to 180 ºC with a pressure of 180 psi and a duration of 5 min. The microwave-assisted heating transforms the carbon source (glucose in this case) into GQDs [57]. The size of GQDs can be varied by changing the concentration of glucose solution, duration of microwave heating, and temperature/pressure used in heating process.

3.1.3 Chemical vapor deposition of graphene

Large area monolayer graphene was synthesized by chemical vapor deposition [58]. Copper foil was first cleaned to remove the oxide layer, then was briefly rinsed with DI water and dried immediately. Copper foil was put into a one-inch-diameter quartz tube furnace. The tube was pumped down to a pressure of ~30 Pa, then 50 sccm H_2/Ar (10%/90%) was introduced into the tube. The temperature of the tube was raised at a rate of 15 ºC/min to 1000 ºC. The copper foil was annealed at 1000 ºC for 15 min, then 25 sccm of high purity methane gas was flowed into the tube for about 10 min. When time was up, the foil was pushed out of the heating zone to introduce quick cooling.

The flow of methane gas was cut. The furnace was quickly cooled to room temperature.

3.1.4 Synthesis of graphitic carbon nitride

Melamine (99%, Sigma Aldrich) was grounded into fine powders using mortar and pestle. 5 g of melamine was put into an alumina crucible with lid. It was put into a muffle furnace and heated in air at a rate of 2 ºC/min to 550 ºC and maintained for 4 hrs, then cooled at a rate of 2 ºC/min to room temperature. A yellowish g-C_3N_4 solid was obtained. It was grounded to fine powders using mortar and pestle. 400 mg of the powder was transferred to an alumina crucible without a lid. It was heated in air to 500 ºC for 2 hrs at a heating and cooling rate of 2 ºC/min. g-C_3N_4 powders with a lighter yellow color were obtained [59].

3.2 Characterization methods of graphene-based nanomaterials

3.2.1 Atomic force microscopy

Atomic force microscopy (AFM) was employed to measure the thicknesses and morphology of materials with nano- to micro-scale features. It gives sub-nanometer resolution in the z-direction, thus in the research of 2D materials, AFM could be used to identify single atomic layer. AFM can probe bulk insulating surfaces, which is a shortcoming for scanning tunneling microscopy (STM) where samples with good electrical conductivity are required, though STM provides even higher resolution than AFM. The schematic diagram illustrating the working principle of AFM is shown in Figure 3.1 [60]. The sample is placed onto a piezoelectric stage. The stage could move along x-y-z direction in micrometer interval with high precision as it is driven by piezoelectric force. A cantilever is used to probe the sample surface. The cantilever has a sharp tip on the end touches the sample. The tip interacts with the sample surface with interatomic force as shown in Figure 3.1(b) [60]. AFM enables non-destructive mapping of morphology using the tapping (non-contact) mode. The cantilever oscillates in resonance. When the tip is close enough to the sample such that the interatomic force becomes repulsive, the cantilever would be deflected away from sample, thus no contact (or damage) is made with the sample. A laser beam is directed onto the tip of cantilever and is reflected to a photodiode array. The deflection of the cantilever due to interatomic force is detected by the photodiode array, which transform to the signal to give the morphological details of the sample. An example of AFM image showing a layered material, SnS_2, is shown in Fig. 3.2.

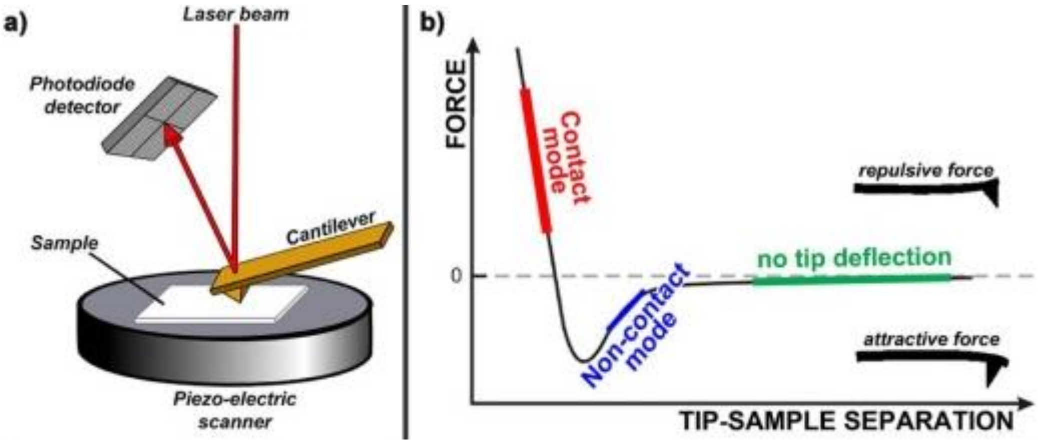

Figure 3. 1 (a) Schematic illustration of the working scheme of AFM. (b) Interatomic force as a function of separations between atoms [Retrieved from Ref. 60].

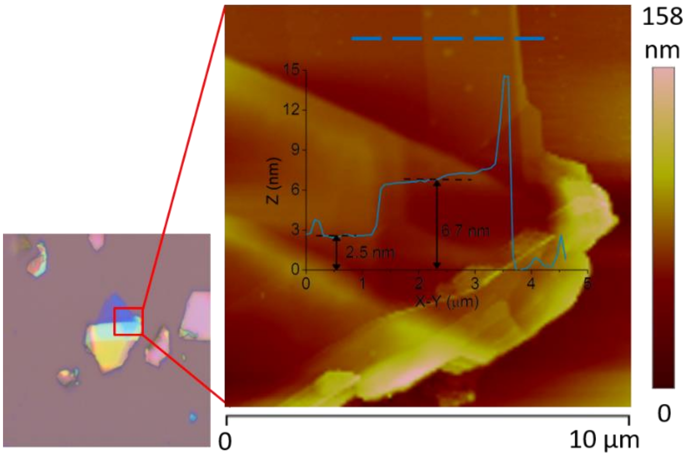

Figure 3. 2 Example of an AFM (right) image of the layered material SnS_2 deposited by mechanical exfoliation. Optical image (left) of the SnS_2 nanosheet. Red square indicates the area of the AFM measurement.

3.2.2 Raman spectroscopy

Raman spectroscopy is a versatile tool for identification of the composition, crystal orientations, investigation of chemical bonding and strains in materials. Monochromatic light from laser is directed onto the sample through objectives.

Incident light is scattered elastically and inelastically by the sample. The inelastic scattering can be divided into Stoke scattering and anti-Stoke scattering. The former has a decrease in frequency in the scattered light while the latter has an increase in frequency. Raman spectroscopy uses only the inelastically scattered light. Raman shift (Δ, cm^{-1}), the quantity measured in Raman spectra, is the change in the frequency of scattered light compared with the frequency of incident light, and it is defined by $\Delta = \frac{1}{\lambda_o} - \frac{1}{\lambda_R}$, where λ_o is the incident wavelength, λ_R is the Raman scattering wavelength. Stoke scattering has a higher probability to occur then anti-Stoke scattering.

Molecules in the sample can originally be in the ground state (which may result in elastic Rayleigh/Mie or inelastic Stoke scattering) or in some excited vibrational and rotational states (may result in inelastic anti-Stoke scattering). Inelastic scattering arises when incident photons interact with the electron cloud of the molecule and excite it to a higher virtual energy state, which then relax to a state with different vibrational or rotational states from the original state. If relaxed state is of a higher (lower) energy than before excitation, the emitted photons would be of a lower (higher) frequency than incident light, by energy conservation, gives Stoke (anti-Stoke) scattering.

Schematic diagram of the main components in a Raman spectrometer is shown in

Figure 3.3 [61]. Elastic scattered light from sample is blocked by a Rayleigh filter like holographic notch filter or edge filter. The remaining inelastic-scattered light enters a diffraction grating. The inelastic-scattered light is spatially overlapped with multi-wavelength of light, i.e. a white beam. For spectrographic analysis, different wavelengths need to be spatially separated. When light hit the reflective diffraction grating, different wavelengths are diffracted by different angles, this enables each wavelength to be detected by different pixels on the multichannel detector, which is the charge-coupled device (CCD). The Raman shift and intensity can then be calculated to give the spectrum.

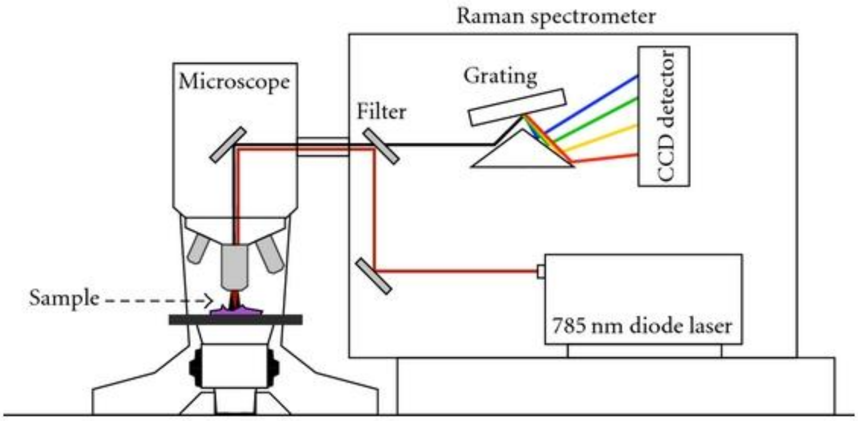

Figure 3.3 Schematic illustration of the main components in a Raman spectrometer. [Retrieved from Ref. 61].

3.2.3 X-ray diffraction

X-ray diffraction (XRD) is used to provide information on the identification, phase, strain, crystal domain size, purity/quality, orientation of crystalline materials. X-ray is used instead of other part of EM spectrum since its wavelength is comparable to the separation between crystal plane (in the order of Å). Monochromatic X-ray beam strikes a crystal that is of arbitrary orientation. It is reflected off when it hits atomic planes. The optical path difference between two adjacent reflected X-rays is $2d\sin\theta$, where d is the separation between atomic planes, 90º-θ is the incident and reflected angle of the X-ray. From classical wave mechanics, constructive interference would occur only when the optical path difference between adjacent X-ray equals to the integral multiples of wavelength (λ). (Bragg's law:$2d\sin\theta = n\lambda$, n is an integer.) The constructively interfered X-ray from reflection, with a stronger intensity, can then be detected to give X-ray peaks. The schematic diagram of an X-ray diffractometer is shown in Figure 3.4. Since d-values are determined by material and λ is fixed, 2θ is swept to allow the condition for constructive interference to be hit in the diffractometer. The detector is moved in an arc such that 2θ is swept and corresponding intensity of scattered X-ray is recorded. In this way, the sample needs not to be rotated to allow scanning through different θ, which is desirable for powder samples.

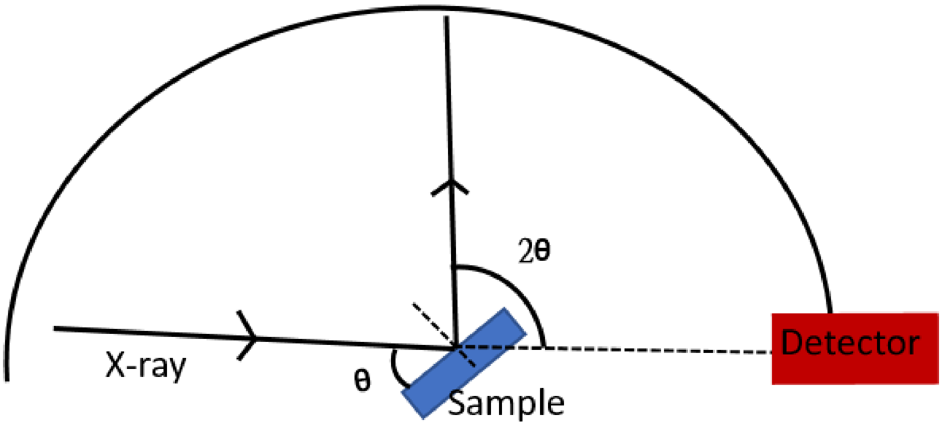

Figure 3.4 Schematic illustration of the X-ray diffractometer.

3.2.4 Photoluminescence spectroscopy

Photoluminescence (PL) is the emission of photons when the electrons relax back to ground state after it is being excited to a higher energy state by the absorption of photons from a light source. It is useful for investigating the carrier dynamics, impurity band, defects, traps, relaxation pathways etc. in the materials by various PL techniques like power-dependent, temperature-dependent, low temperature, and time-resolved PL. The emitted photons usually have a longer wavelength than the excited photons (Stoke shift). The excited photons in common practice are chosen to have energy larger than the band gap of the materials. Electrons in material excited to energy state above the conduction band edge of the material, which would in ultrafast time scale relax towards the conduction band edge by emission of phonons. Then recombination with holes in valance band edge and emit photons, thus PL provides a raw estimation of the optical band gap energy.

Bandgap measurement

Special care has to be taken as PL sometimes do not accurately reveal the optical band gap, e.g. PL peak positions may shift when using solvents with different polarities, though the solute, being the light absorber and PL emitter, remains unchanged. PL is always complementary to optical absorption spectrum. Significant difference in the energy between the absorption edge and PL peak can occasionally been encountered [62], where the PL peak is at a lower energy than the absorption edge. PL emission is sensitive to defects or impurities present in the material. PL maybe dominated by bound excitons captured by defects or impurities that have energy states situated below the conduction band edge [62]. Therefore, PL can be used to determine whether the sample is defective, and often optical absorption instead of PL is used to determine the optical band gap in the material.

Optical and electronic bandgap

However, optical band gap from optical absorption measurements cannot be used to determine the position of conduction band (CB) minimum and valance band (VB) maximum if the exciton binding energy of the material is large, for example in organic materials, and materials with strong quantum confinements. Exciton binding energy arise from the Coulomb interaction of the photo-excited electron-hole pairs. Optical bandgap is related to the electronic bandgap by the relations $\mathrm{E}_g = E_g^{opt} + E_b$, where E_g is the electronic bandgap, E_g^{opt} is the optical bandgap and E_b is the exciton binding energy. E_b of silicon is ~14 meV [63], and E_g of silicon is ~1.1 eV, thus E_b is negligible in silicon as compared with the bandgap. In this case, optical bandgap maybe used to determine energy band structure of silicon. In addition, thermal energy at room temperature ($k_B T$) is ~25 meV, which is comparable with the exciton binding energy of silicon, thus excitons readily dissociate to form free electrons and holes in silicon at room temperature, then electron-hole pairs, rather than excitons, is often used to describe photo-excited carriers in silicon. On the other hand, for instance, in CdSe quantum dots, the exciton binding energy can be as high as 1 eV as its radius is reduced to 6 nm, which is about 1/5 of its bandgap [64]. Another example is the monolayer $MoSe_2$, which has been measured with an exciton binding energy of 0.55 eV with a E_g of 2.18 eV [65]. In these examples, using the optical band gap to determine band edge positions are not feasible. X-ray/ultraviolet spectroscopies and scanning tunneling spectroscopy can be used to eliminate excitonic effects for determining band edge positions, the thus obtained electronic band gap can be compared with the optical band gap obtained from absorption spectroscopy to acquire the exciton binding energy of a material [64].

3.2.5 Optical absorption spectroscopy

When light hit an interface between two materials with different refractive indexes, it could be reflected, absorbed, and/or transmitted, which are respectively described by the quantities reflectance (R), transmittance (T) and absorptance (A) satisfying the conservative relation $R + T + A = 1$.

The Beer-Lambert law is commonly applied in an ultraviolet-visible (uv-vis) spectrometer, where by that law, transmittance, absorbance (A') and absorption coefficient (α) are given by the relations:

$$\%\mathrm{T} = \frac{I}{I_O} \times 100\%$$

$$\mathrm{A}' = -\log\frac{I}{I_O} = -\log\frac{1}{T}$$

$$\frac{I}{I_O} = e^{-\alpha t}$$

Consequently, we get $\alpha = \frac{A}{t\log e} = -\frac{\ln T}{t}$

where t is the optical path length, I is the intensity of light after passing through the sample, I_O is the incoming light intensity.

An equation that accounts also for the reflectance is also used:

$$\alpha = \frac{1}{t}\ln\frac{(1-R)^2}{T}$$

When above equation is used, both the reflectance and transmittance spectra of the sample would be measured.

Reflectance spectra in uv-vis spectroscopy measures the reflected light from the sample (I_R), using the light reflected from a highly reflective surface as the reference (I_O).

$$\%\mathrm{R} = \frac{I_R}{I_O} \times 100\%$$

However, it should be noted that the Beer-Lambert law is established upon a lot of assumptions, two of which are mentioned below. Firstly, there should be no scattering in the sample. Heavy scattering occurs in samples with rough surfaces or solution with high concentration of solute. Secondly, the sample should be homogeneous along the optical path. Otherwise, significant deviation from Beer-Lambert law would be observed.

For highly scattering samples, like powders, diffuse reflectance measurements have to be used in order to obtain accurate absorption of the sample. For the UV to visible range, $BaSO_4$ disc could be used as the reference for diffuse reflection measurement. The acquired spectrum can be converted to the absorption spectrum by the Kubelka-Munk function F(R). $F(R)=(1-R)^2/2R$, where R is the reflectance. F(R) is proportional to the absorption coefficient.

The optical band gap could be obtained by drawing the Tauc plot. Tauc plot corresponds to a plot of $(\alpha h\upsilon)^{1/n}$ vs $h\upsilon$. It is based upon the Tauc equation:

$$(\alpha h\upsilon)^{1/n} = \mathrm{A}(h\upsilon - \mathrm{E}_g^{opt})$$

where A is a constant, E_g^{opt} is the optical band gap, $h\upsilon$ is photon energy.

n=1/2 for direct band gap; n=2 for indirect band gap.

From the above relation, $(\alpha h\upsilon)^{\frac{1}{n}}$ is directly proportional to the quantity $(h\upsilon - E_g^{opt})$, passing through the origin. By plotting the x-axis with $h\upsilon$, the x-intercept of the linear extrapolation equals the optical band gap (E_g^{opt}) of the material. For highly scattering samples, $(F(R)\ h\upsilon)^{1/n}$ is plotted at the y-axis.

Chapter 4 Photodetectors based on graphene oxide nanosheets

Graphene has, in recent years, been popularly investigated for application in photodetection due to its high carrier mobility which has shown potential for high speed operation of up to 500 GHz [66]. It also demonstrates broadband photodetection from ultraviolet to far-infrared [67]. Broadband photodetection has many potential applications in imaging, sensing and communications [67]. However, its good electrical conductivity has simultaneously resulted in a large dark current (I_d) when being applied in photodetectors (e.g. It has been reported that the I_d reaches 10^{-4} A under 1 V bias [67].), which leads to low detectivity in graphene photodetectors [68].

Graphene oxide (GO) and reduced graphene oxide (RGO), which are graphene derivatives decorated with oxygen functional groups on its basal plane and edges, also shows broadband absorption [69]. A few studies have employed GO or RGO as the only active material for photodetection at different spectral ranges [70-74]. Qi *et a*l. demonstrated GO photoresponse in UV, visible light and NIR [72], but highly unstable photocurrent was found upon UV illumination, which was attributed to the reduction of GO in UV. Chitara *et al*. demonstrated GO photoresponse at 360 nm [70] and 1550 nm [71], but without visible light investigation. In addition, the variation of photoresponse over different excitation wavelengths has not been addressed clearly. It is important to understand the wavelength-dependent photoresponse in GO, and the origin of such dependence, in order to ascertain the practical application of GO for broadband photodetection. In this work, vertical junction photodetectors employing partially reduced GO (PRGO) as the only active material were fabricated. The wavelength-dependent photodetection of GO was investigated in detail. Our GO photodetectors demonstrate stable photoresponse in UV and visible light with response time at least one order of magnitude faster than the previously reported GO photodetectors [70, 72, 74].

4.1 Thermal reduction of GO nanosheets

The GO nanosheets were synthesized by a hydrothermal method described in Chapter 3 [55, 56]. GO was transferred onto ITO substrate. ITO as a transparent conductor serves as the bottom electrode of the device. The as-synthesized GO is highly insulating in nature, which can be recognized from the fact that no Hall effect measurements could be conducted from the as-synthesized GO nanosheets. GO with different annealing temperatures are designated by, for example, 800GO for GO annealed at 800 °C.

The Hall effect measurements were conducted in the Ecopia HMS5000. For Hall effect measurement, the GO nanosheets were transferred onto insulating glass substrate, then silver paste was applied at four corners of the GO nanosheets. Each electrode was separated by about 5 mm.

Thermal annealing was used to make the GO nanosheets semiconducting. Since the resistivity of ITO could be increased after heat treatment at temperature higher than 500 ºC [75], GO nanosheets were transferred to copper foil instead of ITO whenever an annealing temperature higher than 500 ºC would be used. To conduct thermal annealing, the GO/ITO or GO/Cu was placed into a tube furnace connected with a vacuum pump. The pressure in tube was pumped down, then temperature was ramped up to the desired temperature and held at that temperature for 8 min. Furnace was naturally cooled to room temperature.

The semiconducting nature of the annealed GO is confirmed by temperature-dependent Hall measurement as shown in Figure 4.1. Both 650GO and 850GO samples show an increase in conductivity (σ) with an increase in temperature, this indicates a semiconducting nature. Since increase in thermal energy increase the carrier concentration in the semiconductors, which can also be seen from the fact that Fermi level in semiconductor is a function of temperature. In contrast, for metals, a decrease in conductivity is expected for an increase in temperature, since electron-phonon scattering is enhanced at higher temperature leading to decrease in mobility while carrier concentration is temperature-independent for metals. By classical Drude model cthat describes a free electron gas, suitable to be used on metals, $\sigma_e = n_e e \mu_e$, where n_e is electron density, μ_e is electron mobility, a decrease in mobility results in decrease in conductivity. From Figure 4.1, the conductivity of 850GO areas 3 orders of magnitude higher than that of 650GO, which demonstrates the effective tuning of conductivity of GO over a large range using thermal annealing.

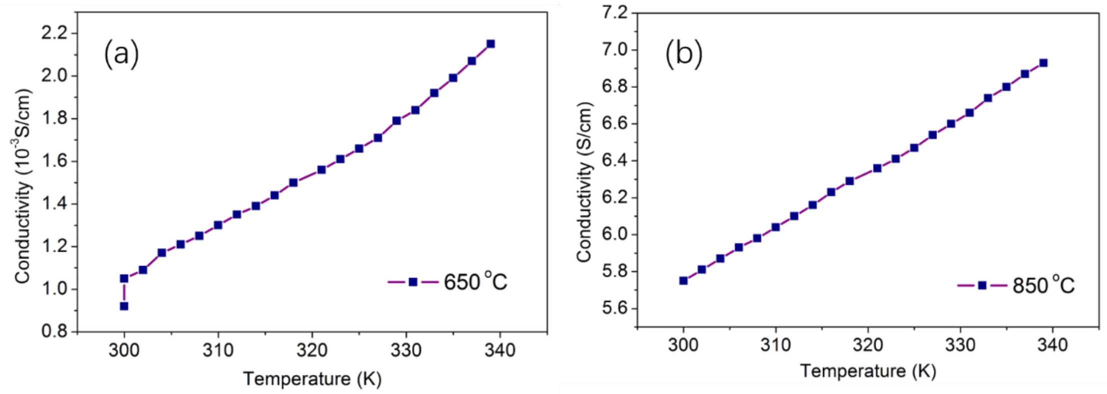

Figure 4.1 Temperature-dependent conductivity of (a) 650GO and (b) 850GO.

4.2 Fabrication of devices

GO transferred onto ITO was annealed at temperature of 450 ºC. Another GO nanosheet was transferred onto Cu foil and annealed at 650 or 700 ºC. The annealed GO on Cu foil was then transferred onto 450GO by dissolving the Cu foil in 0.5 M $FeCl_3$ solution overnight. Annealed GO floated on top of the solution. Using glass slides, it was transferred several times to DI water. Finally, the 450GO/ITO was used to pick up the 650GO or 700GO. Top electrodes, consisted of circles of 3 mm in diameter, was deposited by thermal evaporation of ~100 nm Au through a shadow mask. Schematic diagram of the device is shown in Figure 4.3(a). Light impinged the device from the ITO glass.

4.3 Results and discussions

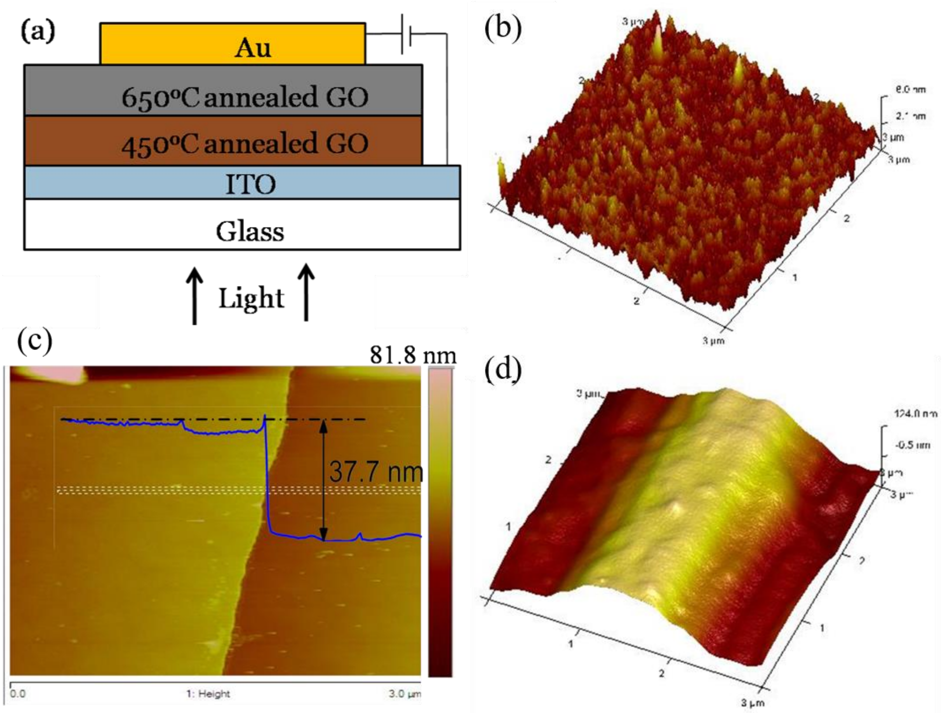

Figure 4. 2 (a) The schematic diagram of the device structure. The active area of the devices was 0.07 mm^2. (b) Topographic image of 450GO, with RMS roughness of 1.1 nm. (c) The AFM image along the edge of 650GO. The inset shows its thickness of 37.7 nm. (d) AFM topographic image of 650GO transferred from copper foil onto SiO_2/Si after annealed on copper foil, with a RMS roughness of 51 nm.

The AFM topographic image of 450GO is shown in Figure 4.2(b). The 450GO film formed from dip-coating of solution-grown GO and underwent subsequent annealing shows a very flat surface with a root-mean-square (RMS) roughness of 1.1 nm. The AFM image measuring the step height of 450GO shows that the thickness of

450GO is 36 nm. From AFM measurements, it could be concluded that the solution-grown GO nanosheets were highly continuous and smooth, cracks were only formed randomly during the dip-coating of GO onto substrate, thus GO nanosheets were suitable for device application. The AFM topographic image of 650GO is shown in Figure 4.2(d). 650GO was first transferred onto Cu foil and thermally annealed, then Cu foil was dissolved and remaining 650GO was transferred on SiO_2/Si substrate for AFM measurement. The additional transfer process from copper foil increased the roughness. RMS roughness of 650GO is 51 nm. In addition, a number of cracks are observed on GO annealed on Cu foil, which are different from the GO annealed on SiO_2 substrate. This could be due to the large difference in thermal expansion of GO and copper foil. Although the linear thermal expansion coefficient (α) of GO is not known, some insights could be obtained from the fact that α of sp^2 (graphite) and sp^3 (diamond) carbon are ~7.8$\times 10^{-6}K^{-1}$ and 1.2$\times 10^{-6}K^{-1}$ respectively, while that of copper and silica are ~17$\times 10^{-6}K^{-1}$ and 0.7$\times 10^{-6}K^{-1}$ respectively. Pristine GO, which is highly insulating, is believed to be dominated by sp^3 bonding, thus GO is expected to show a huge contrast in thermal expansion with copper but not silica.

Roughness of layer in light-harvesting devices

Roughness of layer is considered in light harvesting applications, like solar cells and photodetectors, since from the Fresnel equation in classical electrodynamics, it is known that reflectance is a function of the angle of incidence of light [76]. The relationship of reflectance on the angle of incidence is shown in Figure 4.3 (Retrieved from Ref. 76). In common practice, light incidents perpendicularly to the substrate, and from a lower refractive index material (air, n=1) to a higher refractive index material. If the active layer is smooth, the angles of incidence are small, then the reflectance is smaller than in the case where the surface is rough and the angle of incidence, comprises of a lot of angles, can be large, depending on the morphological features at the interface. For solar cells and photodetectors that consist of multiple active layers, light may enter from a higher refractive index material to a lower refractive index material as light travels through the active layers. For rough interfaces, the higher angles of incidence, which can be larger than the critical angle of the interface, would even result in total internal reflection. Therefore, for light harvesting applications, rough surfaces, as in the case of our 650GO, is not favorable.

To accurately measure the thickness of 650GO, a sample transferred directly onto SiO_2/Si from as-grown GO was used. Figure 4.2(c) shows the AFM image of the 650GO. It can be seen that GO with high annealing temperature on SiO_2/Si substrate and without a second-time transfer shows a flat surface. The thickness is 37.7 nm. Although the precise control in the thickness of GO by this solution-grown method are

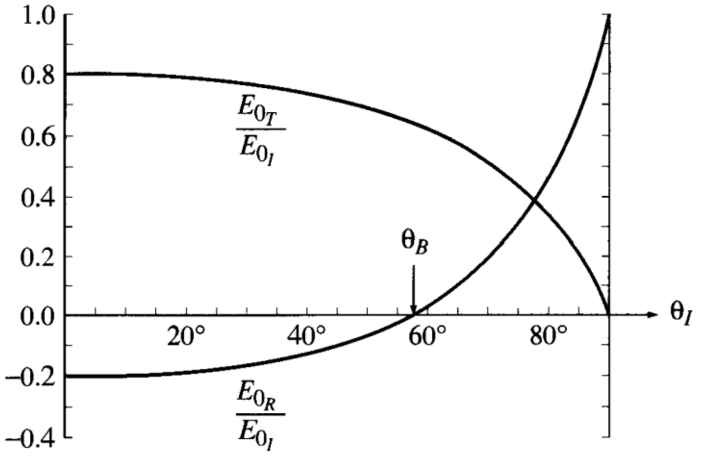

Figure 4. 3 A plot of the transmittance (E_{0T}/E_{0I}) and reflectance (E_{0R}/E_{0I}) as a function of angle of incidence (θ_I) for light entering glass (n_2=1.5) from air (n_1=1), at the air-glass interface, by the Fresnel equation. (Retrieved from Ref. 76.)

not effective, GO nanosheets thickness in the range of 20-40 nm are reproducible using the condition stated. The total thicknesses of the GO nanosheets, which made up the active layers of the devices, are about 70 nm.

The photos of the as-grown GO dip-coated onto fused silica substrate and GO films annealed at different temperatures are shown in Figure 4.4(a). The colour of the GO films deepen gradually as the annealing temperature increases. The GO films show a good coverage on substrates with large area of 1.5×1.5 cm^2. Array of devices (3x3) was synthesized on each ITO substrate with same dimension with that shown in Figure 4.4(a). From Figure 4.4(b), the glucose-derived GO films exhibit two absorption features. One is a shoulder at ~300 nm. This is assigned to the n to π* transition of C=O bond. The other is a peak at ~200 nm, which could be attributed to the π to π*

transition of *sp*^{2} C-C bond. These two peaks are in good agreement with previous reports [77-80]. It could be seen that this peak gradually red-shifted with annealing temperature, which was also observed in previous studies [78-80]. It shifts from 198 to 266 nm, from as-synthesized GO to 1000GO. Peak shift against annealing temperature is plotted in the inset of Figure 4.4(b). It approximately follows a linear relationship. This peak shift is explained by a reduction in the concentration of oxygen functional groups and restoration of the π-electron conjugation network of the GO film. The shoulder disappears at high annealing temperature and only a peak at ~260 nm could be observed. The absorbance from 200-900 nm increases with annealing temperature, which is consistent with the photos in Figure 4.4(a), where the GO films turns from yellow to black with annealing temperature. This reveals that the absorption, and hence the spectral photoresponse of GO is expected to be tunable by controlling the degree of reduction.

The Tauc plots of the GO films for different annealing temperatures are shown in Figure 4.4(c). A direct band gap in GO has been adopted in the calculation (i.e. n=1/2 has been taken, refer to section 3.2.5 for details). Since the PRGO consists of a mixed *sp*^{2} and *sp*^{3} phases [10, 81-84], in addition to large number of trap states resulted from the oxygen functional groups and defects induced by annealing [85, 86]. The GO nanosheets are spatially inhomogeneous and cannot be described by the same band gap values in microscopic domains. The optical bandgap from Tauc plot provides a macroscopic estimation for the optical band gap of the GO that are consistent with the increase in absorption in the GO. For the as-synthesized GO, 450GO, 650GO and 850GO, the optical bandgaps are 4.45, 4.07, 2.71 and 2.41 eV respectively. The optical bandgap of the GO decreases with increasing annealing temperature, which are consistent with previous studies [87, 88]. Bandgap modulation from ultraviolet to visible light regime indicates that the optical properties of the GO are tunable over a large range in addition to electrical properties mentioned in previous section.

The Raman spectra of the GO annealed at various temperatures are shown in Figure 4.4(d). Two characteristic peaks can be observed with the GO films on silica substrate. One is the G peak at ~1600 cm^{-1}. It corresponds to the in-plane vibrations of E_{2g} phonon of sp^2 carbon [81]. Another peak is found at ~1350 cm^{-1}, which is identified as the D peak and is attributed to the A_{1g} vibration of defective six-atom rings [89, 90].

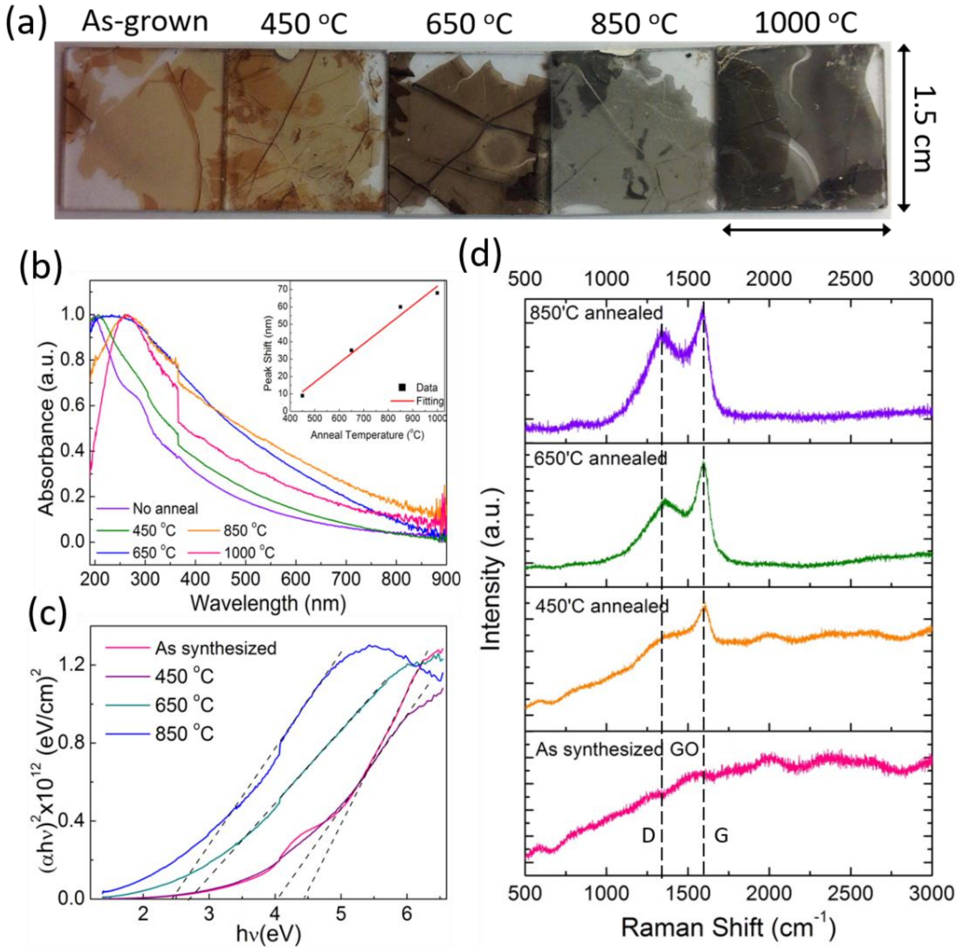

Figure 4.4 (a) Photos of GO nanosheets annealed with different temperatures. Dimension of the substrate is 1.5x1.5 cm. (b) The absorbance spectra of GO with different annealing temperatures. The kink at 365 nm is due to a change in light source in the spectrometer. (c) The Tauc plots of GO with different annealing temperatures. The x-intercepts of the dotted-lines indicate the optical bandgap. (d) Raman spectra of GO with different annealing temperatures.

A strong fluorescence background with no characteristic peak could be observed from the as-synthesized GO. Upon 450 ºC annealing, the G peak appears, which indicates the formation of *sp*^{2} domains. Defective D peak appears as a shoulder, which may be overwhelmed by the background. Huge difference could be noticed as the annealing temperature is increased from 450 ºC to 650 ºC. For both 650GO and 850GO, prominent G and D peaks are observed.

The Fourier Transform infra-red (FTIR) spectra of 45GO and 650GO are shown in Figure 4.5 (a-b). FTIR is an effective tool to investigate the functional groups on GO. The samples were prepared by mixing dried GO nanosheets with KBr powders. The mixtures were grounded to fine powders and pressed into disks for measurement. The peak at ~2920 cm^{-1} corresponds to the stretching of C-H bond [55]. Peaks at ~1710 and 1640 cm^{-1} are attributed to C=O in carboxylic group and C=C bond respectively. Absorption band at ~3400 cm^{-1} is assigned to the –OH bond. Absorption peak at ~1040 cm^{-1} is attributed to C-O in hydroxyl group [91]. The most noticeable change in functional groups at higher annealing temperature would be the diminished absorption band for C=O bond, thus indicates that the restoration of conjugation network in RGO may be contributed by the desorption of carboxylic groups.

The flat band energy band diagram of the device is shown in Figure 4.5 (c). Previous studies have reported the increase in the work function of GO with the oxygen content [92, 93]. Work function of GO and RGO were reported to be 4.9-4.96 eV and 4.79-4.88 eV respectively [94, 95]. Ultraviolet photoelectron spectroscopy (UPS) was used to measure the highest occupied molecular orbital (HOMO) for GO and RGO, which were reported to be ~1.5 eV and ~1.1 eV below the work function respectively [96]. The lowest unoccupied molecular orbital (LUMO) of GO and RGO are located by using the optical bandgap obtained above. The resultant electron band diagram

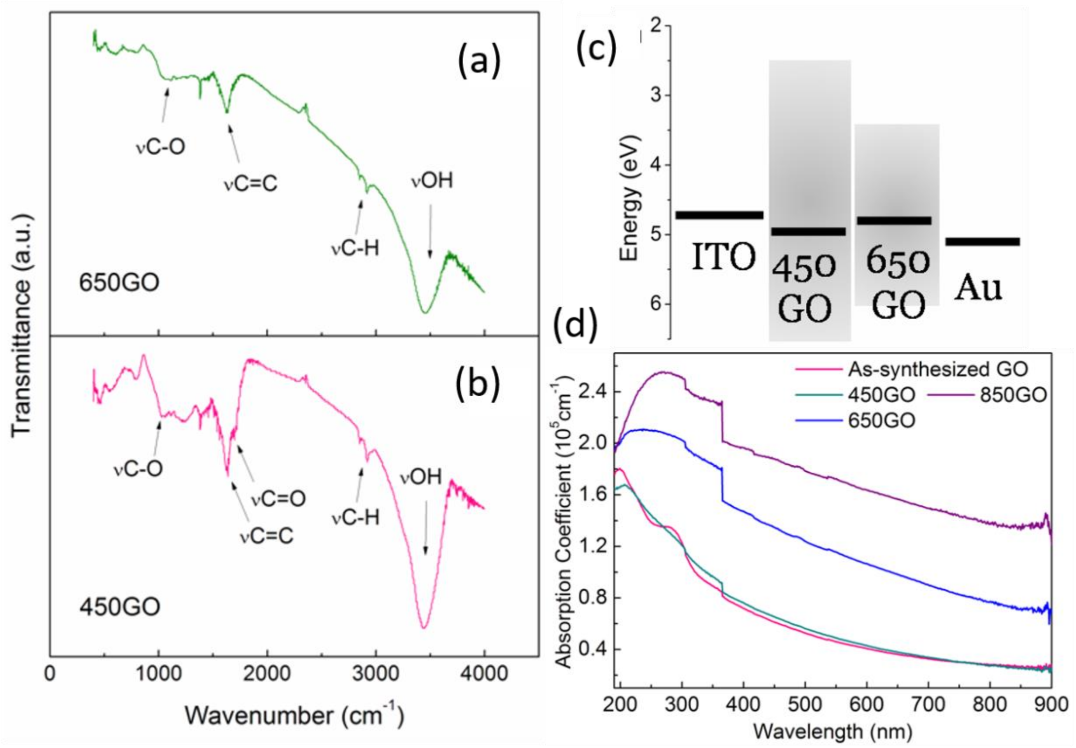

Figure 4.5 FTIR spectra of (a) 450GO and (b) 650GO. (c) The flat band diagram of the device. (d) The absorption coefficient of the GO nanosheets annealed at various temperatures. The kink at 365 nm is due to the switching of light source in the spectrometer.

allows a clearer understanding in the carrier transport in the device. Positive bias is applied to Au electrode, thus photogenerated holes are transported toward ITO cathode and electrons to the Au anode. From the absorption coefficient (α) spectra of GO in Figure 4.5(d), which is normalized against the thicknesses of different GO nanosheets, it is expected that 650GO serves as a more effective light absorber than 450GO in the device. The conduction band edge of 450GO is considerably higher than that of 650 GO. This renders the 450GO a good electron blocking layer in the device by suppressing photogenerated electrons in 650GO diffusing towards 450GO under the concentration gradient, which could reduce the probability of recombination in the device.

For comparison, a set of photodetectors employing 700GO instead of 650GO were fabricated. Photoresponse of the 700GO device is shown in Figure 4.6(a). The initiation of comparing 700GO and 650GO was originated from the result that higher annealing temperature leading to increase in the absorbance of GO, which, may potentially increase the photocurrent in the device. It is found that 700GO devices indeed give a larger photocurrent than 650GO devices under same condition of 410 nm illumination at 3.1 mW and 1 V bias, which leads to a larger responsivity. However, the 700GO device is found to have a much larger dark current in the order of 10^{-4} A (Dark current of 650GO device is at most at the order of 10^{-5} A, ranging from 10^{-5} to 10^{-7} A, as seen from Figure 4.7.), which could be attributed to the higher electrical conductivity of 700GO, considering that the only difference between the two types of devices is the replacement of 650GO by 700GO. The higher dark current leads to critical concern for the detectivity and on/off ratio in the 700GO devices. The detectivity and on/off of the 650GO and 700GO are listed in Table 4.1. For the calculation of specific detectivity (D*), it is assumed that the shot noise from dark current dominated the noise current, since moderate bias is applied and dark current level is considerably high. This gives $D^{*}=RA^{1/2}(2qI_{dark})^{-1/2}$ (Details refer to Chapter 2.). 700GO devices show a lower detectivity and on/off ratio, which indicates that 700GO device would be more inferior for detecting low light intensity than 650GO device. In view of this, 650GO was employed in all the devices involved in subsequent analysis.

A typical dark *I-V* characteristic of the device is shown in Figure 4.6(b). The non-linear *I-V* indicates that there is transport barrier(s) in the device. The current increases exponentially beyond about 1 V at both positive and negative biases, which then the large dark current (10^{-4} A) is not desirable. Thus 1 V bias was used in all the subsequent measurements unless otherwise specified.

Light intensity was measured with calibrated power meter. The area of illumination was fixed at 7 mm^2 by passing light through a shadow mask, except for 1610 nm excitation where the light source was a laser diode thus the actual illumination area of which was limited by the size of light beam.

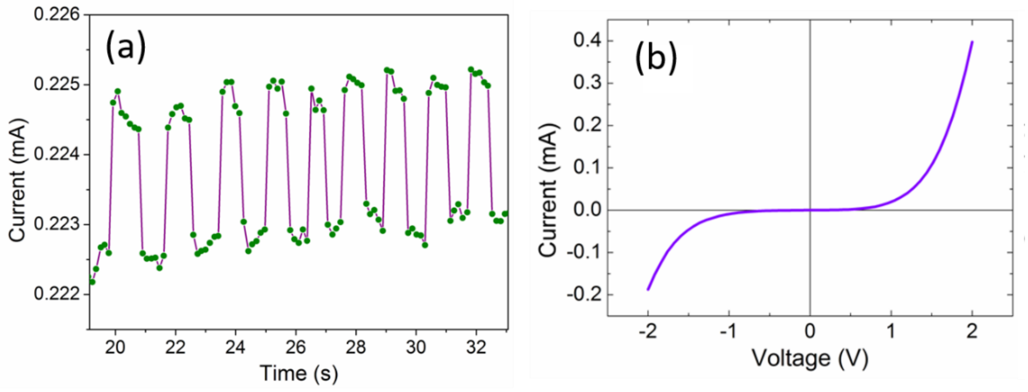

Figure 4.6 (a) Photoresponse of the 700GO/450GO device. (b) Typical dark *I-V* characteristics of the 650GO/450GO device.

Table 4.1 D* and on/off ratio of the 700GO/450GO and 650GO/450GO device structures under 410 nm excitation at 3.1 mW and 1 V bias

Device structure	D*(10^7cmHz$^{1/2}$W^{-1})	on/off
700GO/450GO	2.33	1.01
650GO/450GO	3.31	1.46

Photoresponse of the GO nanosheets-based photodetectors under UV, visible and NIR illumination are shown in Figure 4.7. The spectral range that is investigated in this work covers from 290 to 1610 nm. The photoresponse at 290 nm is shown in Figure 4.8, where a different device structure is used since ITO is opaque to 290 nm. This is the broadest range yet demonstrated on photodetectors that employed GO as the only active material. The photoresponse could be attributed solely to GO as it is the only active material in the device. The device shows satisfactory photoresponse in the UV and visible light region where the photocurrent saturated within the shortest time interval of data acquisition of the system (~105 ms), this indicates that the photocurrent is mainly contributed by the fast drift component with tiny proportion from slow diffusion of carriers [97].

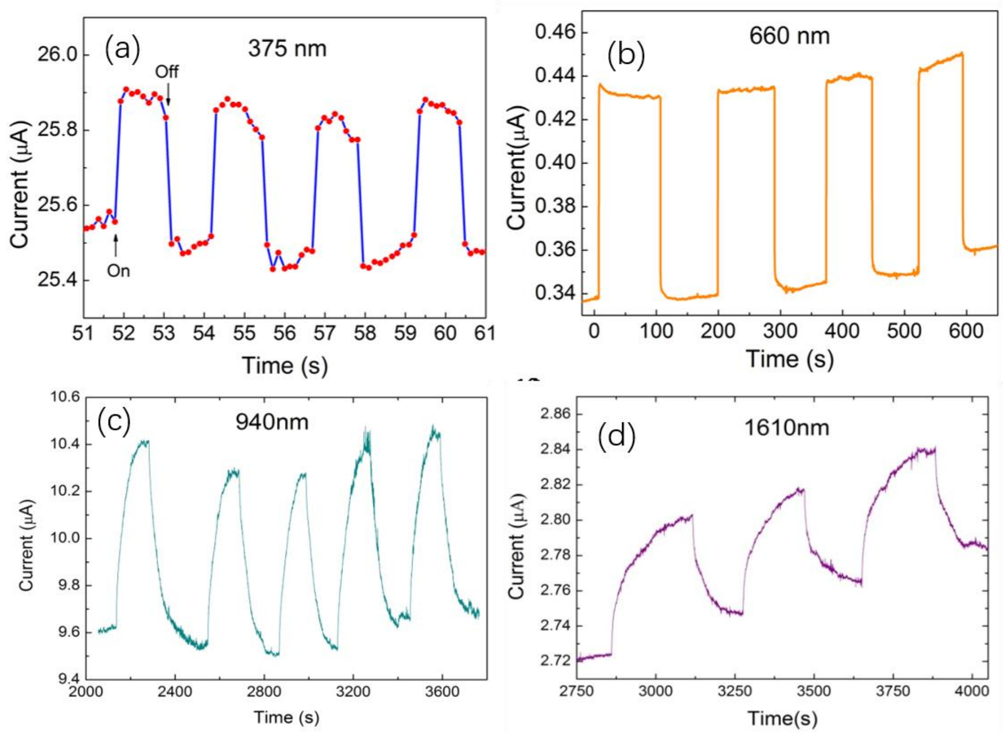

Figure 4.7 Photoresponse of the 650GO/450GO photodetector under illumination at (a) UV, (b) visible light, (c-d) NIR. The wavelengths are indicated in the figures.

The dependence of the photocurrent on the light intensity at 410 nm is shown in Figure 4.9(a). Data points are fitted with the power law $I_{ph} = aP^{\theta}$, where I_{ph} is the photocurrent, P is the light intensity. The value of θ obtained from fitting is 0.991, which is very close to 1. In the ideal scenario, $\theta = 1$, which is explained below: the range of light intensity in which the responsivity remains constant (i.e. $\theta = 1$) is described by the parameter named linear dynamic range (LDR). A large LDR is required for stable and reliable operation over large spectral range in photodetectors.

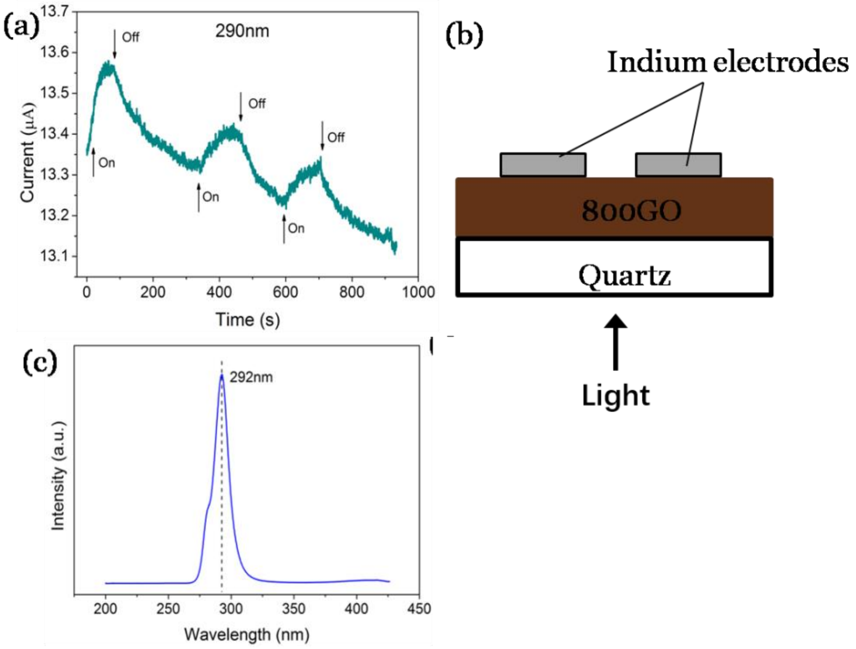

Figure 4.8 (a) Photoresponse at 290 nm illumination. (b) Structure of the device for 290 nm measurement. (c) The electroluminescence spectrum of the 290 nm LED light source.

Figure 4.9(b) shows the reproducibility of the photoresponse. A square voltage of a frequency 0.43 Hz, with the waveform against time showed in the upper part of the figure, was supplied to the light source. The corresponding photoresponse against time is shown in the lower part of the figure. The photoreponse follows closely the voltage waveform of the source, it saturates quickly when light is on. The magnitudes of photocurrent in different ON cycles are found to be nearly constant, though the dark current shows an increasing trend. A changing dark current with time is commonly observed in reported photodetectors [98, 99]. As the magnitudes of photocurrent remain largely the same over all cycles, the change in dark current over time is not attributed to the reduction of GO under light illumination [72].

The variation of responsivity with wavelength is given in Figure 4.9(c). The power at different wavelengths were fixed at 1-5 mW in this measurement, since the responsivity may also be a function of light intensity. It can be seen that the responsivity decreases with the wavelength from 375 to 940 nm, and could be well-fitted with an exponential function. The inset of Figure 4.9(c) is plotted with the responsivity in linear scale. As expected, the responsivity exhibits a similar trend with the UV-Vis absorption spectrum as shown in Figure 4.4(b). The broadband photoresponse of the device is attributed to the wide range absorption of the PRGO nanosheets. They exhibit a weak but non-zero absorption in NIR which results in the low responsivity in NIR.

Figure 4.9(d) shows the photocurrent against voltage relationship under different light intensities. This is similar to the output characteristics of field effect transistors (FET), with the light intensities interchanged with gate voltage. This analogous gives us hint on the effect induced by light in the device. The gate voltage in FET modulates the charge concentration in the channel by capacitive induction. In this device structure, charge concentration is modulated by generation of charge carriers excited by light. At low light intensity, the photocurrent exhibits higher non-linearity with voltage, it increases exponentially with voltage; when light intensity is increased to 2 and 3.9 mW, the photocurrent increases linearly with voltage. The photocurrent at low light intensity is limited by potential barriers in the device, which can be inferred from the highly non-linear dark *I*-*V*. Higher voltage induces band modulation and current increases exponentially as seen from below relationship. It describes the dependence of current density (*J*) on electric field (E) over a Schottky-type barrier based on thermionic emission of carriers [100],

$$J = AT^2 exp[\frac{E - E_B}{kT} - 1]$$

where A is Richardson's constant, k is Boltzmann's constant, *T* is temperature, E_B is the barrier height.

Increase in light intensity increases the carrier concentration in the vicinity of the barrier, which leads to enhanced modulation of barrier. This light-induced barrier modulation results from carrier accumulation lowers the barrier height [101]. At high light intensity, the linear increase in photocurrent suggests that the transport at high light intensity is not limited by potential barrier.

Figure 4.9(e) shows the responsivity as a function of light intensity. The highest responsivity of the device under 1 V bias at 410 nm is 23.6 mA/W, which is higher than the RGO/Si nanowires hybrid photodetectors [69] and is comparable to other GO-based photodetectors [70, 72]. The responsivity decreases with light intensity, which may indicate the occurrence of non-linear processes in the device under photo-excitation. This phenomenon is also observed in quantum dots-based photodetectors

[102, 103].

The time response of the device is analyzed in Figure 4.10(a). The rise time and fall time are determined to be 130 ms and 152 ms respectively at 660 nm. The response times at different excitation wavelengths are tabulated in Table 4.2. The response time in UV and visible light range are at least one order of magnitude faster than the previously reported photodetectors that applied GO as the only active material, where the reported time constants are ~30 min [70] and 5 – 20 s [72] in UV and visible light respectively. The response time shows a strong dependence on wavelength. Response time in NIR is about two orders of magnitude slower than that in UV and visible. This behaviour has also been observed in a reported work [72]. The NIR response clearly composes of a faster drift component and a slower diffusion component where the former is represented by the sharp increase in current and the latter by the exponential saturation of photocurrent. A possible reason for the slow response time at NIR is trapping of charge carriers. It has been reported that C=O functional groups and defects in GO may act as charge trapping centers [104], which results in a negative photocurrent [70], and slow response time [72]. Due to the weak absorption in NIR, assuming a constant number of trapping sites in GO, a larger proportion of photogenerated carriers from NIR excitation are trapped as compared with UV and visible excitation. Trapping increases the recombination lifetime of carriers [105] and results in long response time.

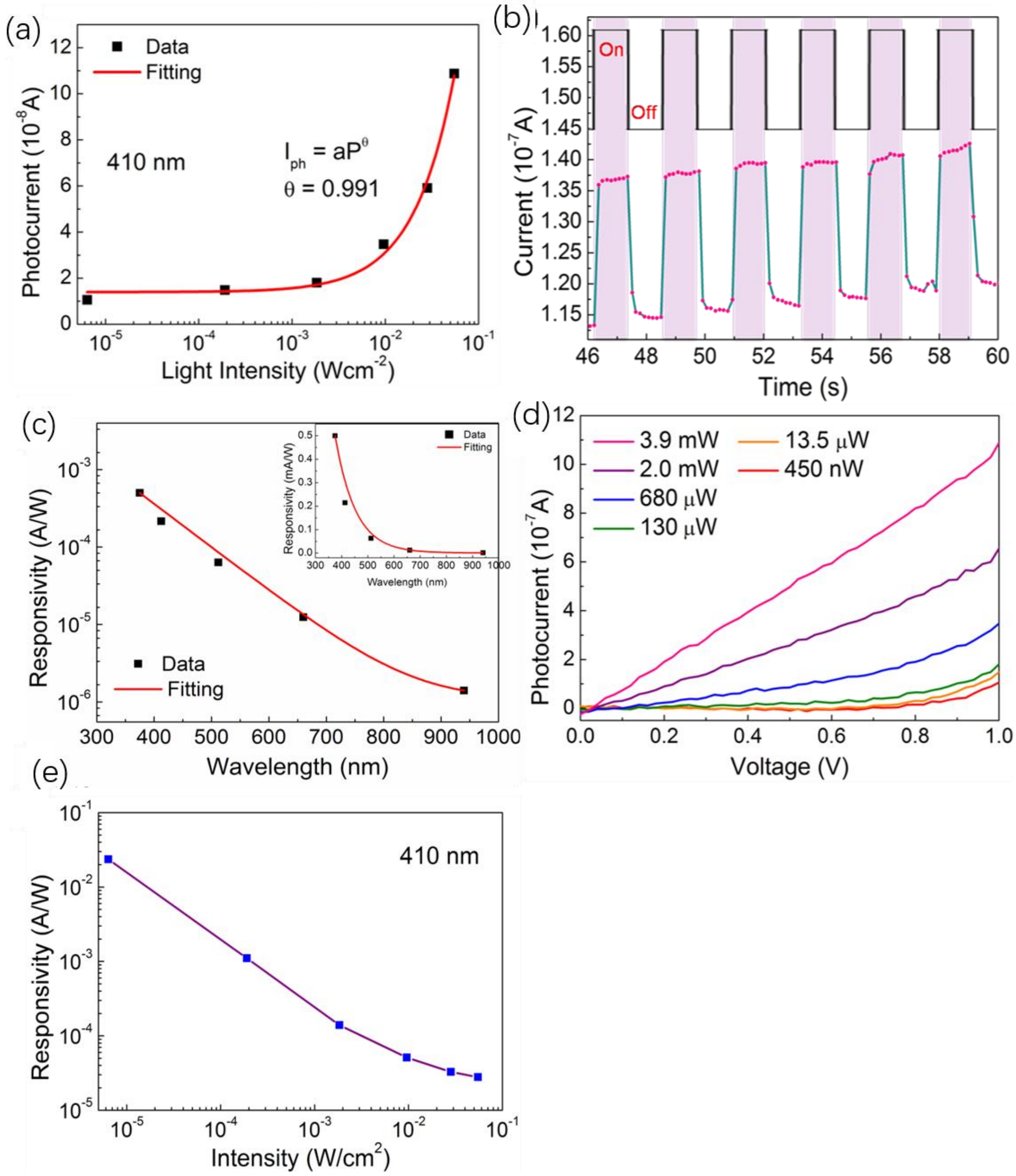

Figure 4.9 (a) Photocurrent as a function of light intensity at 410 nm. Fitting parameters are provided. (b) Good reproducibility of the GO-based photodetectors. Upper part shows the applied voltage to light source, and lower part the photoresponse. (c) Responsivity at different wavelengths. (d) Photocurrent as a function of voltage for different light intensities. (e) The variation of responsivity with light intensity. Highest responsivity is measured at the lowest light intensity with a value of 23.6 mA/W.

Figure 4.10(b) shows the GO-based device operated under self-powered mode, i.e. under zero bias. This property is investigated for the first time in GO-based photodetectors. The device demonstrates a prominent and fast response. The response is compared with the situation when the device is under 1 V bias, with same condition of excitation at 410 nm at 3.1 mW. The magnitude of photocurrent is smaller at zero bias, which is expectable, but the on/off ratio increased from 1.46 at 1V to ~10^3 at zero bias. Self-powered photodetectors are more favourable for operating in harsh condition and weight reduction. This ultrathin GO photodetector showed huge potential for self-powered photodetectors.

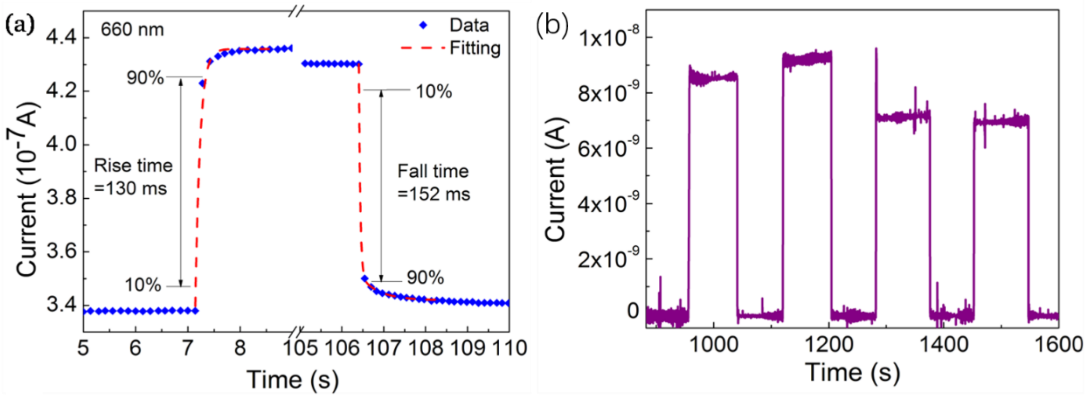

Figure 4.10 (a) Response time analysis of photoresponse at 660 nm. (b) Photoresponse of the device operating under self-powered condition.

Table 4. 2 Rise and fall times under different excitation wavelengths

Wavelength (nm)	Rise time	Fall time
375	~105ms	~105ms
660	130ms	152ms
1610	78.13s	70.99s

Chapter 5 Photodetectors based on graphene quantum dots functionalized with conducting polymer

GQDs have attracted intense interest in the past few years as they exhibit strong PL [106, 107], and couple with other properties, such as heavy metal-free, bio-compatible [108], suitable for low cost fabrication and good solubility in water. GQDs have been successfully utilized in light-emitting diodes [109, 110], solar cells [111, 112] and photodetectors [113-115]. Effective ways to synthesize GQDs with controllable properties are highly desirable for the above applications. Functionalization and making composites of GQDs have shown to be an effective way to tailor the electrical and optical properties of GQDs [116-119]. A number of works have been done on the amine-functionalization of GQDs. They demonstrated tunable PL peak position of the functionalized GQDs by varying the number of amine group on GQDs [116] or by varying the pH value to trigger the protonation of the alkyl amine group [119]. Recently, our group has synthesized the GQDs-polyaniline (PANI-GQDs) nanocomposite [120]. It has shown that the PL peak and hysteretic *I-V* behaviour of PANI-GQDs can be progressively tuned by altering the amount of aniline in the synthesis. In this work, it is further demonstrated that *I-V* hysteresis can also be obtained from pristine GQDs, such that the charge storage effect of GQDs and PANI-GQDs nanocomposite have further been compared to elucidate the effect of PANI functionalization. It is found that PANI-GQDs exhibited larger hysteresis than GQDs at different voltage scan ranges, together with the demonstration of the optically tunable hysteresis in PANI-GQDs. The optoelectronic properties of GQDs and PANI-GQDs are also compared by studying their photoresponse. PANI-GQDs exhibit a higher responsivity and shorter response time under visible light illumination as compared to GQDs.

5.1 Synthesis of PANI-GQDs nanocomposite

GQD solution was first synthesized by the method described in Chapter 3.2. Aniline monomer (5 mmol) was added into 10 ml of GQD solution [121]. Hydrochloric acid (37 %) was added dropwise into the mixture with continuous stirring until 0.5 M HCl was obtained. The mixture was sonicated for 15 min to allow uniform dispersion of aniline, which was then heated in a water bath at 80 °C for 30 min, and cooled in an ice bath. 0.1 M ammonium persulphate, which was used for its oxidizing property, was added into the mixture and stirred thoroughly. The solution was stored at 4 °C for one day for polymerization. It was then centrifuged at 3000 rpm for 20 min. Supernatant was collected and was used as the PANI-GQDs nanocomposite. Pure PANI was synthesized by the same procedure but with DI water replacing GQDs solution and without undergoing centrifugation.

5.2 Fabrication of devices

Interdigitated electrodes were fabricated on 300 nm SiO_2/Si substrate by standard photolithography. The electrode consisted of 20 fingers, each separated by 25 μm and having a width of 30 μm. Ti/Au (10/100 nm) was deposited by magnetron sputtering, which was followed by lift-off process in acetone. Substrates with electrodes were cleaned with oxygen plasma to remove any residue photoresist, then equal volume (100 μL) of pure GQD or PANI-GQD solution was spin-coated onto the electrodes at 2000 rpm. The devices were dried in ambient condition for one day then heated at 90 °C for 30 min. The devices were then used for measurements.

5.3 Results and discussions

5.3.1 Characterization of GQDs and PANI-GQDs

The transmission electron microscopy (TEM) image of GQDs is shown in Figure 5.1(a). The GQDs disperse uniformly on the grid. No sign of aggregation is observed. The diameters of GQDs span from 2 to 7 nm, with an average of 4.58 nm. Figure 5.1 (b) shows the high-resolution TEM image of a GQD. Lattice spacing is measured to be 0.21 nm, which corresponds to the [110] planes of graphite [122]. The TEM images of PANI-GQDs are found in Figure 5.1(c-d). The polymer forms separate islands with GQDs embedded in it, a typical one is shown in Figure 5.1(c). The average diameter of GQDs inside the nanocomposite is measured to be 4.54 nm. Like pure GQDs sample, the GQDs in the nanocomposite do not show sign of aggregation. The functionalization with PANI does not significantly impact the distribution and size of the GQDs, which agreed with the discussion in previous work by our group [123]. High resolution TEM image of the nanocomposite could not be obtained as the high beam intensity under high magnification was found to damage the nanocomposite.

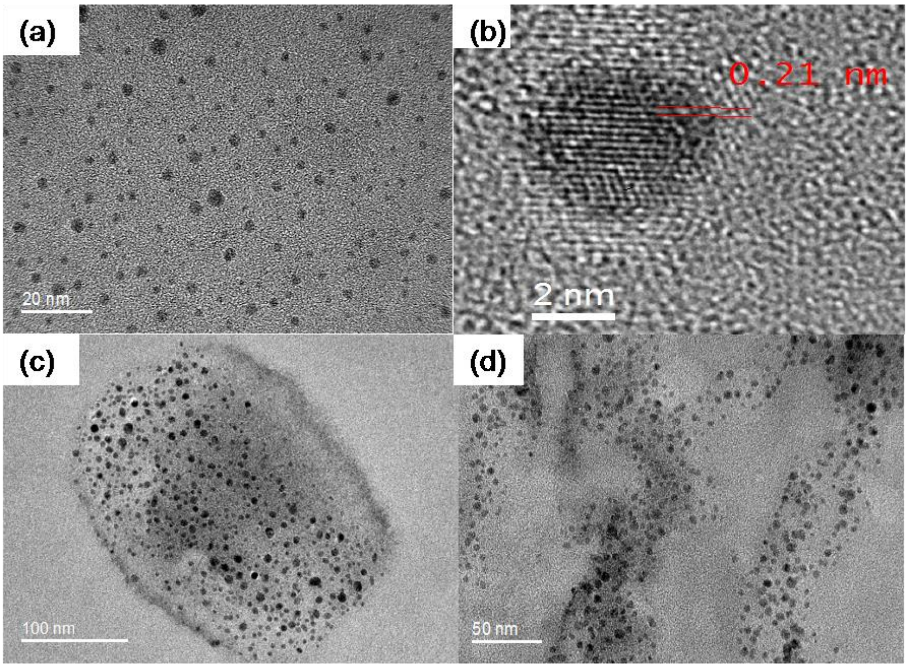

Figure 5.1 (a) TEM image of the as-deposited GQDs on carbon film-coated copper grid. (b) High resolution TEM image of a GQD showing a lattice spacing of 0.21 nm. (c-d) TEM images of the PANI-GQDs nanocomposite.

Figure 5.2 shows the X-ray photoelectron spectroscopy (XPS) spectra of the as-deposited GQDs and PANI-GQDs. From the full range XPS spectra, the PANI-GQDs have extra peaks belonging to nitrogen and sulfur, apart from the carbon and oxygen peaks that are also observed in GQDs. This is expected as the extra elements are originated from PANI, given that the chemical formula of PANI is ($[C_6H_4NH]_2[C_6H_4N]_2)_n$.The C1s peaks (Figure 5.2 (c-d)) is deconvoluted into five peaks that are located at 284.8 eV (*sp^2* carbon), 285.4 eV (*sp^3* carbon), 286.3 eV (C–OH), 287.8 eV (C–O–C) and 288.9 eV (C=O). The *sp^2* peak of the PANI-GQD is more prominent than that of the GQD, which could be attributed to the extended π-conjugation network in PANI. The N1s peak of PANI is deconvoluted to three peaks at 399.2 eV (pyridinic N), 400.6 eV (pyrrolic N), and 402.2 eV (graphitic N).

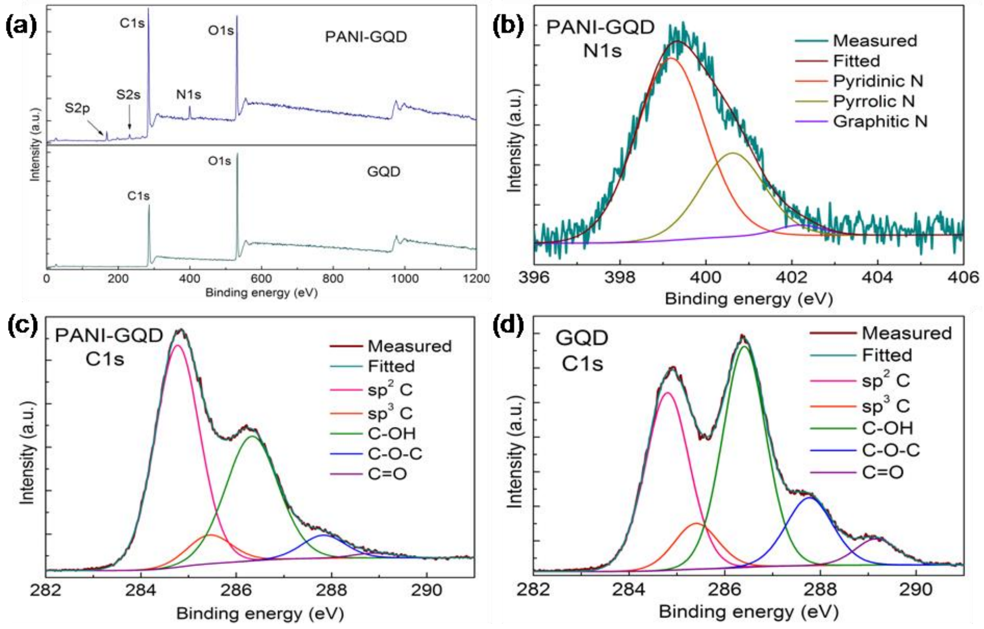

Figure 5.2 (a) Full-scan XPS spectra of the PANI-GQDs (top) and GQDs (bottom). (b) XPS N1s spectrum of the PANI-GQDs. XPS C1s spectra of the (c) PANI-GQDs and (d) GQDs.

The influence of the functionalization of GQDs with PANI is analyzed through optical absoprtion spectra. In Figure 5.3 (a), normalized absorption of GQDs and PANI-GQDs samples are stacked together for comparison. GQDs show two absorption peaks. One locates at ~228 nm, which could be attributed to the π to π* transition of C–C; another peak locates at 284 nm, which corresponds to n to π* transition of C=O bond respectively [57]. These two peaks are also observed in PANI-GQDs, but one additional peak at ~365 nm is found from the PANI-GQDs sample. The appearance of the new absorption peak, which is not found in the pure PANI, could be explained by the formation of a charge transfer complex [124, 125]. The amine group presented in aniline is bonded to the GQDs after functionalization [123]. The valance electron pair in the amine group could promote electron donation to the GQDs [119]. The absorption of PANI-GQDs with different amounts (1-5 mmol) of aniline monomer added in the nanocomposite are shown in Figure 5.3(b). The peak at ~284 nm which arises from C=O bond has intensity decreases monotonically with the increase in aniline. The number of amine group bonded on the GQDs are expected to increase with aniline concentration. This suggests that the amine group has displaced some of the C=O group on GQDs. Furthermore, the extra peak is found to red-shift with increase in aniline concentration as shown in the inset, which verifies that the origin of the new peak is closely related to the functionalization.

The FTIR spectra of GQDs and PANI-GQDs nanocomposite are shown in Figure 5.3(c). Absorption peaks at ~1020 and 1160 cm^{-1} correspond to the C-O and C-N bonds respectively. The peaks at 1400-1450 and 1650 cm^{-1} correspond to the C=C and C=O bonds respectively. Some features of GQDs and PANI could be found in PANI-GQDs. The C=O peak is observed in PANI-GQDs and GQDs but not in PANI which indeed has no carbonyl group. Moreover, in the range 1000-1450 cm^{-1}, GQDs exhibit a broad absorption band due to the abundant C-O bonds from carboxyl and hydroxyl groups, while PANI-GQDs and PANI exhibit a sharp peak which is resulted from the C=C bond. This is in agreement with the C1s XPS spectra where the C=O, C-O-C and C-OH peaks are less prominent in PANI-GQDs as compared with GQDs.

Figure 5.3(d) shows the PL spectra of the GQDs (dotted lines) and PANI-GQDs (solid lines) for a range of excitation wavelength. Equal volume (600 μl) of PANI-GQDs and GQDs solution were transferred to cuvettes without dilution in order to compare their PL. The PL characteristics of the GQDs and PANI-GQDs exhibit a few differences. The maximum PL intensity of GQDs is found at 450 nm with 360 nm excitation while that of PANI-GQDs peaks at 600 nm with 450 nm excitation. Another feature is that the location of PL peak for PANI-GQDs red-shifts from that of GQDs under same excitation wavelength. The red-shift is persistent over the entire range of excitation wavelength used in the measurement from 325 to 640 nm. Functionalization of GQDs with NH_3 [116] and PEG-diamine [119] have also reported the red-shift in PL when compared with pristine GQDs, and was attributed to electron transfer from amine group to GQDs. The amine group in aniline is also expected to induce similar charge transfer effect thus gives rise to the PL modification after functionalization. In addition, for excitation wavelength from 325 to 420 nm, the PL of the GQDs has higher magnitudes than PANI-GQDs, while for longer excitation wavelength from 450 to 640 nm, with corresponding emission wavelength from 600 to 660 nm, the PL of the PANI-GQDs are stronger than GQDs. In other words, the PANI-GQDs exhibit stronger PL than GQDs when being excited by the red end of the visible light spectrum. This property is advantageous for bio-imaging applications, because intense excitation in ultraviolet and the blue end of the visible region may induce damages to biomaterials [118, 126].

The time-resolved PL measurement of the GQDs and PANI-GQDs are shown in Figure 5.4 (a). The decay curves were fitted with a triple exponential function to extract the decay time using below equation:

$$\mathrm{f(t)} = \sum_{i=1}^{3} A_i e^{-\frac{t}{\tau_i}}$$

where t is time, A_i are some constants, and τ_i are the time constants.

Then the average PL lifetime $\langle\tau\rangle$ is calculated from the τ_i obtained above:

$$\langle\tau\rangle = \frac{A_1{\tau_1}^2 + A_2{\tau_2}^2 + A_3{\tau_3}^2}{A_1\tau_1 + A_2\tau_2 + A_3\tau_3}$$

The PANI-GQDs solution exhibits a longer PL lifetime than GQDs. The average decay times for PANI-GQDs and GQDs are 3.98 and 3.51 ns respectively.

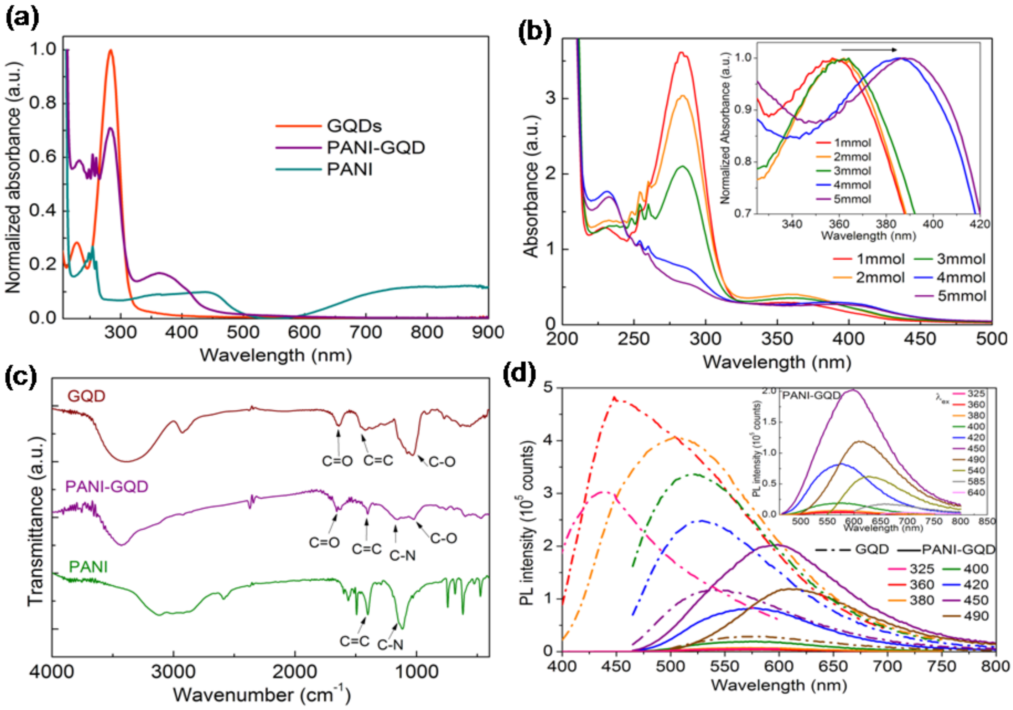

Figure 5.3 (a) Normalized absorption spectra of the GQDs, PANI-GQDs and PANI. (b) Absorption spectra of the PANI-GQDs with amount of aniline monomer varied from 1 to 5 mmol. (c) FTIR spectra of the GQDs, PANI-GQDs and PANI. (d) PL spectra of the GQDs and PANI-GQDs under different excitation wavelengths as tabulated in the figure.

The origin of the PL of the GQDs can be attributed to intrinsic state emission as a result of quantum confinement, and also emission from defect states [127]. One type of defect states is the various functional groups in the atomic plane and on the surface of the GQDs. GQDs with higher defect density were reported to have a PL peak at a longer wavelength than GQDs with less defects [127]. PL lifetime is also elongated in the defect states. In view of the longer emission wavelength and the longer PL lifetime in PANI-GQDs as compared to GQDs, the increase in decay lifetime of the nanocomposite is explained by surface states engineering due to functionalization which changes the defect state emission.

Figure 5.4(b) shows the PL spectra of the PANI-GQDs synthesized using different amounts of aniline. The peaks red-shift monotonically from 525 to 650 nm with increasing aniline concentration from 1-5 mmol under same excitation wavelength at 450 nm. This demonstrates that the PL of PANI-GQDs nanocomposite is intrinsically tunable.

The Raman spectrum of the PANI-GQDs nanocomposite is shown in Figure 5.4(c). It exhibits two peaks that are commonly found in carbon-containing materials, and are also observed in pristine GQDs [128]. They are the D peak at ~1350 cm^{-1} and the G peak at ~1600 cm^{-1}. The origin of these peaks can be referred to Chapter 4.

The thermogravimetric analysis (TGA) of the PANI, PANI-GQDs and GQDs carried out in argon atmosphere are shown in Figure 5.4(d). The weight losses of PANI-GQD, GQD and PANI when heated up to 900 ^{o}C are 54%, 80% and 86% respectively. The weights of the GQDs and PANI reduce significantly in the range of 200-400 ^{o}C, which is attributed to the decomposition of functional group. However, the weight of the PANI-GQDs only shows a mild decrease for temperature above 300 ^{o}C, which demonstrates a higher thermal stability.

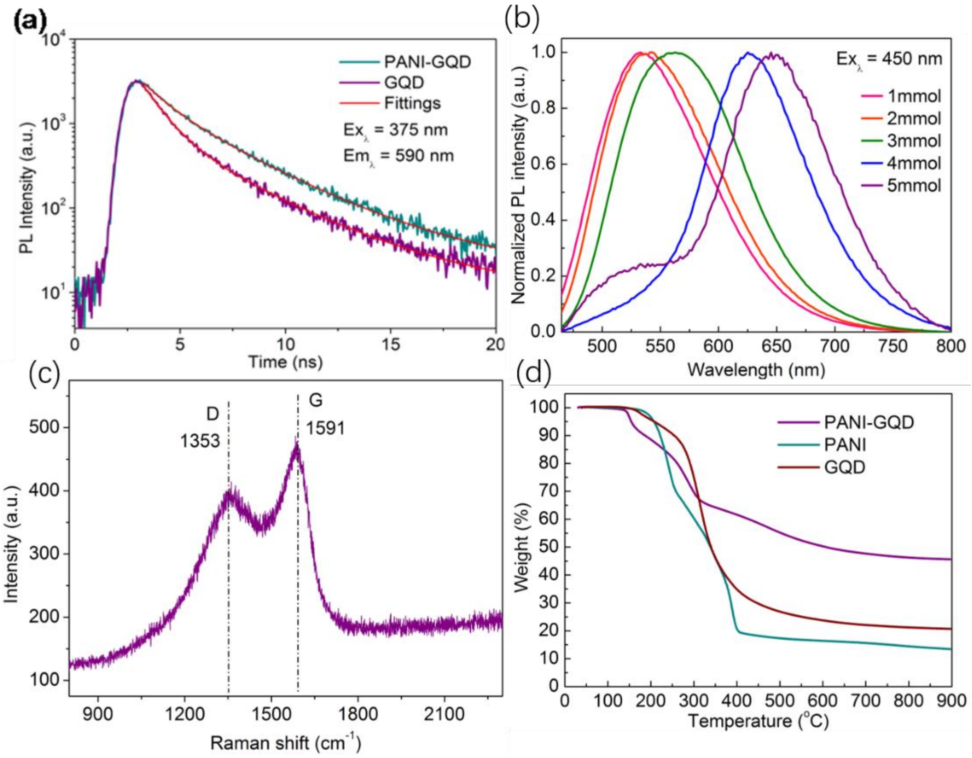

Figure 5.4 (a) The time-resolved PL measurements of the GQDs and PANI-GQDs. (b) PL measurements with excitation wavelength at 450 nm of the PANI-GQDs synthesized with different amounts of aniline. (c) Raman spectrum of the PANI-GQDs recorded under 488 nm laser. (d) TGA of the GQDs, PANI-GQDs and PANI in argon atmosphere.

5.3.2 Electrical measurements

The electrical measurements and photoresponse of the PANI-GQDs and GQDs devices are analyzed in this section. All electrical measurements were conducted with Keithley 2400 in the ambience at room temperature. Figure 5.5(a) shows the *I-V* curves of the GQDs and PANI-GQDs. The *I-V* curve measured in the dark for both types of device show significant hysteresis, which are persistent for all 20 consecutive cycles in the measurements. In addition, the PANI-GQDs exhibits a large hysteresis than GQDs for all cycles. The hysteresis of *I-V* curves in this work are not the pinched *I-V* curves that are observed in memristors as they do not pass through the origin [129]. Instead, their shapes are commonly found in cyclic voltammetry measurement for evaluating capacitors. The hysteretic *I-V* curves implied that both the GQDs and PANI-GQDs devices behave like symmetric all solid-state capacitors, in which charges are stored during voltage sweep [130]. The area enclosed in the hysteretic loop is related directly to the specific capacitance of the devices [131]. As shown in Figure 5.5(b), under the same scan rate, the PANI-GQDs devices have a larger hysteretic area of about 2 to 3 orders of magnitude than the GQDs devices for various voltage scan ranges. Thus the nanocomposite PANI-GQDs show a higher charge storage capacity than GQDs. *I-V* measurement for pure PANI with same device configuration is shown in the inset of Figure 5.5 (a). A linear curve with no hysteresis is obtained, thus the enhanced capacitive property is not due to pure PANI that is present in the PANI-GQDs, and could be attributed to the nanocomposite. Although a better capacitive performance of the PANI-GQDs is revealed, detailed analysis of this property, like performance under variation of scan rate, cycling stability etc., is not the main goal of this work and is left for future investigation.

In previous work by our group, the hysteresis of PANI-GQDs was shown to increase with the amount of aniline used in synthesis. In this work, it is further demonstrated that the hysteresis is optically tunable. Figure 5.5(c) shows the *I-V* measurement of the PANI-GQDs devices under different light intensity at 405 nm. It is observed that the device is photo-responsive in which the photocurrent increases with light intensity at a fixed scan range of ±1 V. The part at larger voltage value is enlarged and shown in the inset of Figure 5.5(d) to show more clearly the photocurrent.

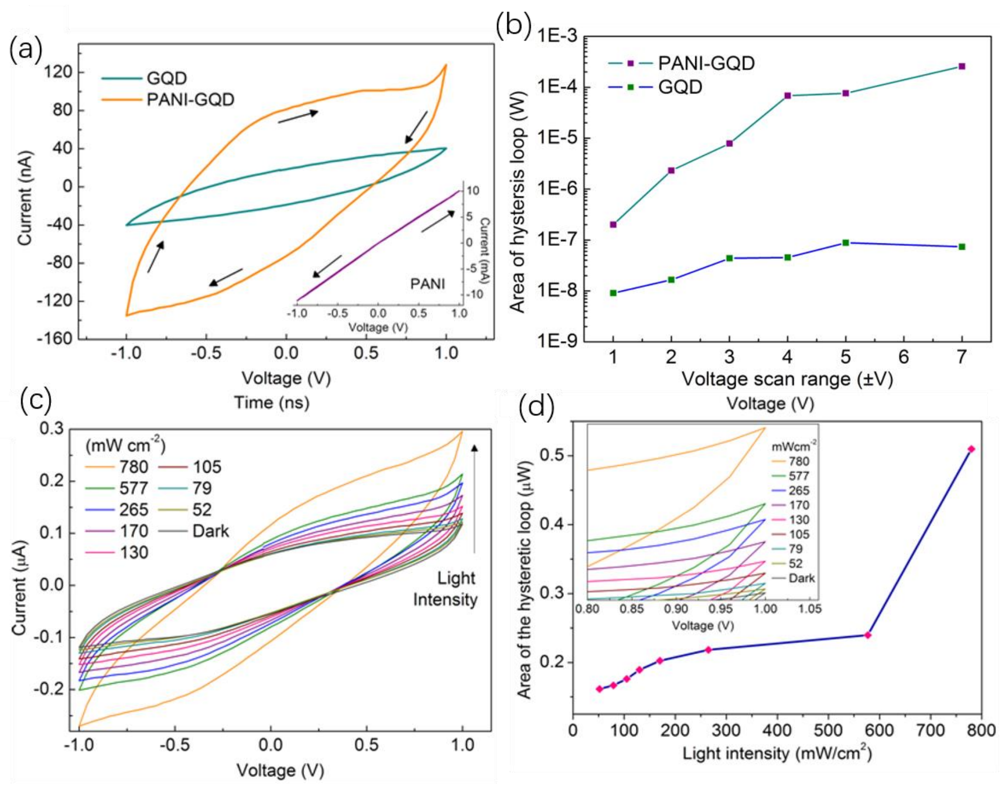

Figure 5.5 (a) The *I-V* curves of the GQDs and PANI-GQDs devices. Inset shows the *I-V* curve of pure PANI with same device architecture. (b) The enclosed area in the hysteretic *I-V* loops of the GQDs and PANI-GQDs for different voltage scan range at fixed scan rate. (c) The optically tunable *I-V* curves of PANI-GQDs device. (d) Area enclosed in the hysteretic loops in (c), which reveals that the charge stored in the device is optically tunable. Inset shows the enlarged curves in (c) at the higher voltage values.

The area in the hysteretic loop is calculated in Figure 5.5(d), it demonstrates that the amount of charge stored in the devices could be increased by ~3.3 folds as the light intensity is increased from 52 to 780 mWcm^{-2}.

In view of the large differences in the optical absorption, PL and electrical properties between the GQDs and PANI-GQDs demonstrated in previous section, the photoresponse of the GQDs and PANI-GQDs devices are further compared in this section. It is shown that the functionalization of GQDs with PANI lead to an enhancement in photoresponse.

The temporal response of the PANI-GQDs and GQDs at 405 nm and 532 nm are shown in Figure 5.6 (a) and (b) respectively. Both types of devices show satisfactory photoresponse in the way that current increases when light is on, saturates when illumination is continued, and falls back to dark current level when light is turned off. However, drastic contrast is observed in the photoresponse of the PANI-GQDs and GQDs for both wavelengths. Firstly, GQDs device shows a lower dark current than PANI-GQDs device by ~2-6 folds. Secondly, the PANI-GQDs device demonstrates larger photocurrents than GQDs for both 405 nm and 632 nm at 1 V bias and same light intensity. At 405 nm (Figure 5.6 (a)), the responsivity of the PANI-GQDs is an order of magnitude higher than that of GQDs. At 532 nm (Figure 5.6 (b)), the responsivity of the PANI-GQDs is 7 folds higher than that of GQDs. Since specific detectivity $D^* = R/(2qJ_{dark})^{1/2}$ when assuming that the shot noise is dominated by dark current as stated in Chapter 2, the detectivity of the PANI-GQDs devices are also higher than that of GQDs for both 405 nm and 532 nm.

The response times of the PANI-GQDs and GQDs are analyzed in Figure 5.6 (c) and (d) respectively. The temporal response curves are fitted with the equations: $I(t) = I_{dark} + A_1 \exp(t/\tau_{r1}) + A_2 \exp(t/\tau_{r2})$ for the growth part and $I(t) = I_{dark} + A_3 \exp(-t/\tau_{d1}) + A_4 \exp(-t/\tau_{d2})$ for the decay part, where t is time, A are some constants, $\tau_{r1,2}$ and $\tau_{d1,2}$ are the rise and decay time constants respectively. It is found that both the rise and decay times of the PANI-GQDs are faster than the GQDs at 405 nm and 1 V bias. The values of the time constants are provided in the figure. In summary, the rise time of the PANI-GQDs device is two folds faster and the decay time is four folds faster than the GQDs device.

A collection of the photoresponse parameters of the GQDs and PANI-GQDs devices at 1 V bias are tabulated in Table 5.1. The improved responsivity and response time of the PANI-GQDs are attributed to an enhancement in the inter-connection of the GQDs by the conducting polymer. As revealed in the TEM images, pristine GQDs are spatially isolated from each other due to electrical repulsion of the functional groups on the surface of the GQDs. On the other hand, the GQDs are embedded in nano-size, island-like conducting polymer matrices in the PANI-GQDs nanocomposite.

The polymer with extensive delocalized π-electrons facilitates charge transport within the polymer matrices which enables the photoresponse to have a pronounced improvement.

The dependence of photocurrent on light intensity for the PANI-GQDs device is investigated as shown in Figure 5.6(e). Data points are fitted with the power law $I_{ph} = aP^{\theta}$, where I_{ph} is the photocurrent, and P is the light intensity. The value of θ is 0.89, which differs considerably from 1, for light intensity ranges from ~50 to ~800 mWcm^{-2}. In Figure 5.6 (f), it can be seen that under fixed light intensity, the photocurrent and therefore the responsivity is effectively increased in the PANI-GQDs device by increasing the bias voltage. The responsivity of the PANI-GQDs device at a bias voltage of 2.5 V and 405 nm is 18 μA/W. The photocurrent and responsivity increase by six folds as the bias voltage is increased from 0.5 to 2.5 V.

As shown in Figure 5.7 (a), when the bias voltage is equal or below 3 V, the PANI-GQDs device exhibits a positive photocurrent. However, when the bias voltage is increased to above 4 V, negative photocurrent is obtained, as seen from Figure 5.7 (b), where this light intensity is fixed in the bias-dependent measurements. Above 4 V, when light is turned on, the current first experiences a sharp rise, but after less than 0.5 s, it decreases continuously until a negative photocurrent is achieved. The negative photocurrent is indicated in the figure. When light is turned off, the current increases back to the dark current level.

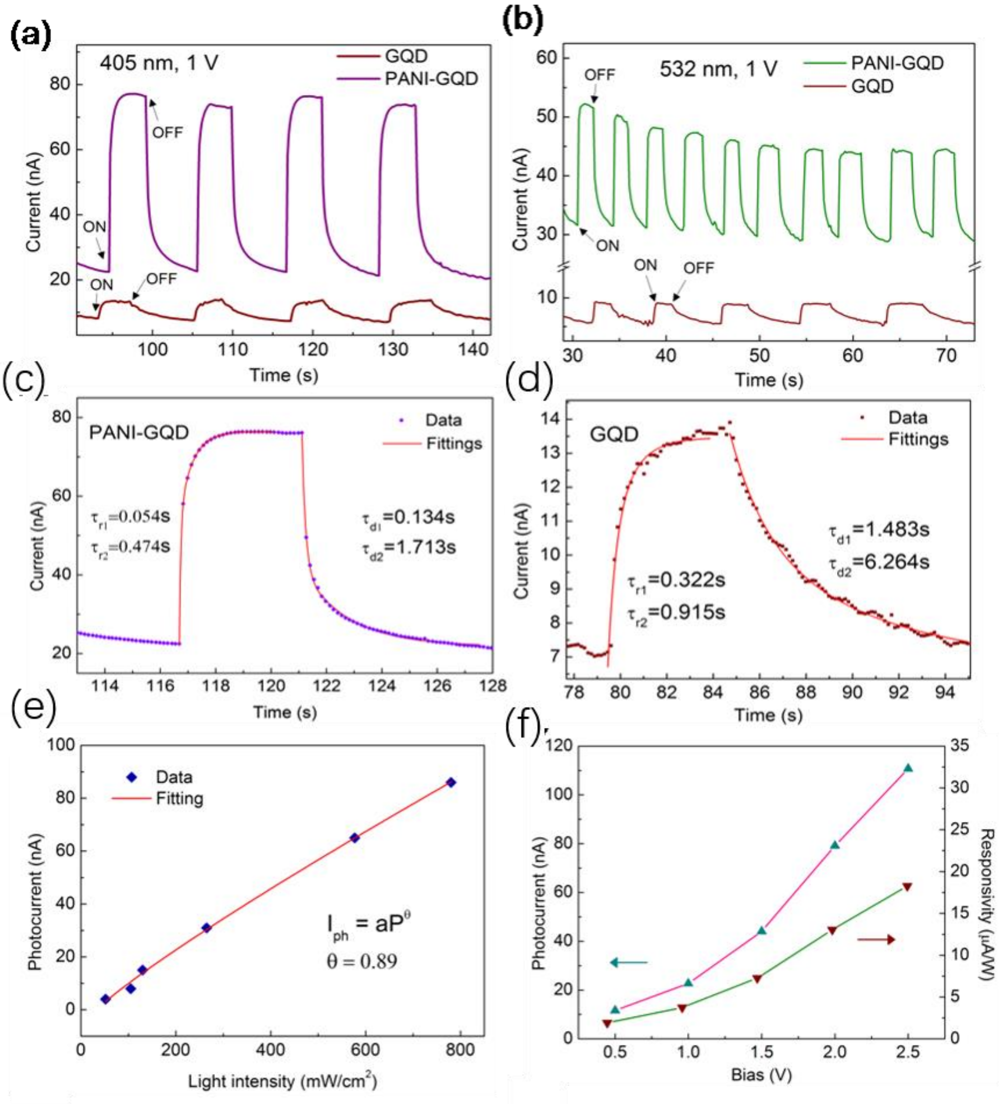

Figure 5.6 Photoresponse of the PANI-GQDs and GQDs upon on-off cycles at (a) 405 nm and (b) 532 nm. Response time analysis of the (c) PANI-GQDs and (d) GQDs devices. (e) The dependence of the photocurrent on light intensity. (f) Photocurrent and responsivity against bias voltage.

Furthermore, the negative photocurrent could be reverted to positive photocurrent when bias voltage is changed from 4 V back to below 3 V, therefore the photocurrent could be switched between negative and positive reversibly by controlling the bias voltage. This phenomenon is found to be largely related to the GQDs but not the

Table 5.1 Summary of the photoresponse at 1 V of the PANI-GQDs and GQDs devices

Device	I_{ph} at 405 nm (nA)	R at 405 nm (μA/W)	I_{ph} at 532 nm (nA)	R at 532 nm (μA/W)	τ_{r1}/τ_{r2} (s)	τ_{d1}/τ_{d2} (s)
PANI-GQDs	52.66	8.69	23.00	1.05	0.054/0.47	0.13/1.71
GQDs	5.06	0.835	3.41	0.155	0.32/0.92	1.48/6.26

functionalization as it is also observed in the pure GQDs device with the same crossover voltage of 3-4 V, as demonstrated in Figure 5.7 (c), though the magnitude of negative photocurrent is larger in the PANI-GQDs devices. This switching behavior in the sign of the photocurrent has not been reported in GQDs-based devices to the best of our knowledge.

When the bias voltage is below 4 V, the positive photocurrent is observed to decrease slowly with time as shown in Figure 5.7(a). In view of this, a prolonged illumination of over 240 s is carried out at 1 V bias to investigate if negative photocurrent would also be obtained at lower bias voltage. The results are shown in Figure 5.7 (d) and (e). Both the PANI-GQDs and GQDs maintain a positive photocurrent after prolonged illumination at 1 V.

Voltage-sensitive switching in the sign of photocurrent has been reported for a film of metal nanoparticles functionalized with ligands on the surface [132], where the originally charge-neutral ligands become charged at higher applied bias. The charged ligands have a lower charge-trapping energy level. Electrons are excited to this new

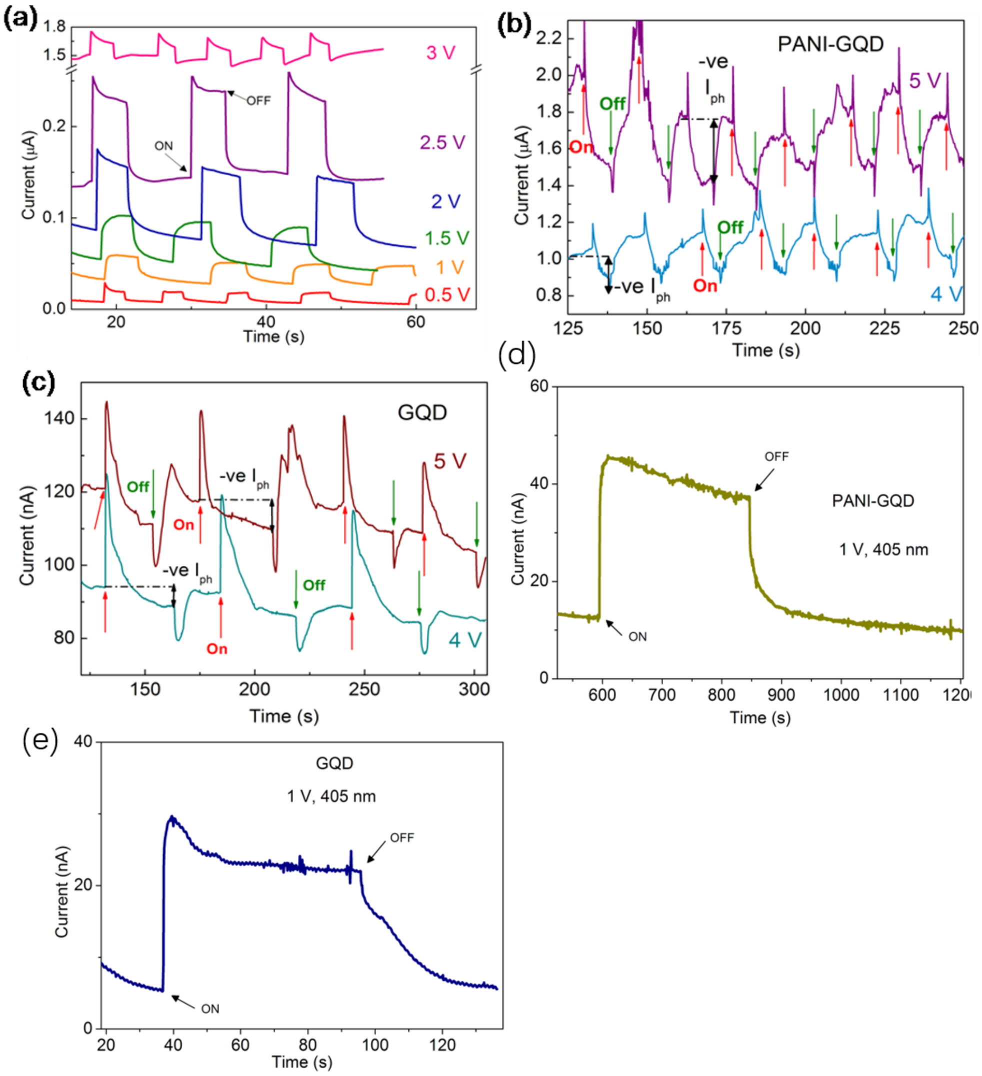

Figure 5.7 (a) Positive photocurrent of the PANI-GQDs for bias voltages from 0.5 to 3 V. (b) Negative photocurrent of the PANI-GQDs at 4 to 5 V bias. (c) Negative photocurrent of the GQDs at 4 to 5 V bias. Prolonged illumination of the (d) PANI-GQDs and (e) GQDs device.

level under light and are trapped, resulting in a negative photocurrent [132]. Another work on Ag nanoparticles embedded below graphene reported the switch of photocurrent from negative to positive as bias was changed from 10 mV to 1 V, and was attributed to the desorption of charge trapping adsorbates due to illumination and plasmons-enhanced electric field [133].

The above reports motivated us to investigate the photoresponse of the devices in N_2 atmosphere which would elucidate the effect of desorption of highly polar adsorbates like water originated from the ambient air on the transport characteristics of the device. The devices were heated in N_2 at 90 ^{o}C for 30 min prior to measurements to drive away adsorbates. Surprisingly, as shown in Figure 5.8 (b), the PANI-GQDs device becomes highly insulating in the N_2 environment---with the dark current reduced by several orders of magnitude as compared to that in the ambience, and no photoresponse could be observed even at a higher bias voltage of 7 V. When the devices were transferred back to the ambience, photoresponse could be observed again. Polar adsorbates are shown to have tremendous effect on the electrical transport of the GQDs, but their role in the photocurrent switching behavior remains unclear.

Another attempt to elucidate the origin of photocurrent switching is shown in Figure 5.8 (a). The *I-V* loop of the PANI-GQDs is swept for different voltage scan ranges from ±1 to ±7 V. Measurements were conducted in the dark. For the voltage scan ranges of ±1 to ±3 V, the current changes monotonically with voltage. However, for the voltage scan ranges of ±4 to ±7 V, an obvious negative differential resistance (NDR) could be observed. A current drop commences as the voltage increased to about 3.3 V. This can be observed more clearly with the inset in Figure 5.8(a) where the ±3 and ±4 V ranges are selectively enlarged. The onset of NDR at 3-4 V is consistent with the voltage for photocurrent switching discussed above.

This is attributed to the presence of charge trapping states in the GQDs. Trapping states are initiated at 3-4 V. At such bias, under illumination, photogenerated carriers are excited to the trapping energy level. These trapped charges further interact with free carriers injected from electrodes by electron-electron scattering, such that negative photocurrent is observed.

The origin for the initiation of trapping states at 3-4 V is not known and requires further investigation. Previous works suggest that there could be a change in the charging states of the functional groups presented on the GQDs that create new trapping energy level, or desorption of adsorbates at this voltage [132, 133], which provide us insights for future investigations.

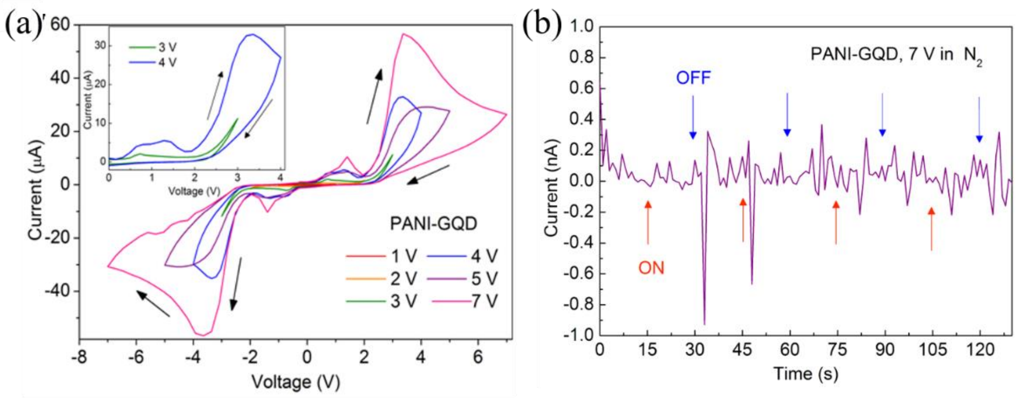

Figure 5.8 (a) Positive photocurrent of the PANI-GQDs for bias voltages from 0.5 to 3 V. (b) Negative photocurrent of the PANI-GQDs at 4 to 5 V bias. (c) Negative photocurrent of the GQDs at 4 to 5 V bias. Prolonged illumination of the (d) PANI-GQDs and (e) GQDs device.

Chapter 6 Phototransistors based on graphene/ g-C_3N_4 nanosheets heterostructure

Graphitic carbon nitride (g-C_3N_4) has attracted intense interest in recent years in the field of hydrogen evolution reaction (HER) under visible light illumination [134]. One of the most heavily studied materials for HER is TiO_2. TiO_2 has a band gap in the UV region. UV only comprises of 2-3 % of the solar spectrum measured on the ground, while visible light constitutes 44-47 % of it. As a result, it has long been a goal to develop HER photocatalysts that utilize also the visible light region [13].

g-C_3N_4 is a layered material with an inter-layer distance of 0.32 nm. The lattice structure of perfect g-C_3N_4 with heptazine building unit is shown in Figure 6.1. The polymeric g-C_3N_4, which is found to have potential for visible light HER, can be synthesized by a facile thermal treatment of nitrogen-rich precursors like melamine, dicyandiamide etc. It is commonly reported to have hydrogen incurred in the final structure of polymeric g-C_3N_4, as hydrogen is found in the chemical formula of the popularly-used precursors mentioned above. Polymeric g-C_3N_4 is known to possess disorders with respect to the perfect g-C_3N_4 lattice due to incomplete polymerization of the precursor. Nonetheless, the polymeric g-C_3N_4 has a suitable bandgap and band structure that make it a good visible light HER catalyst. Its bandgap is ~2.7 eV, such that it could absorb the blue end of visible light, in addition, the conduction and valence band edge are at the energy levels where the oxidation and reduction potential of water lie inside the bandgap of polymeric g-C_3N_4.

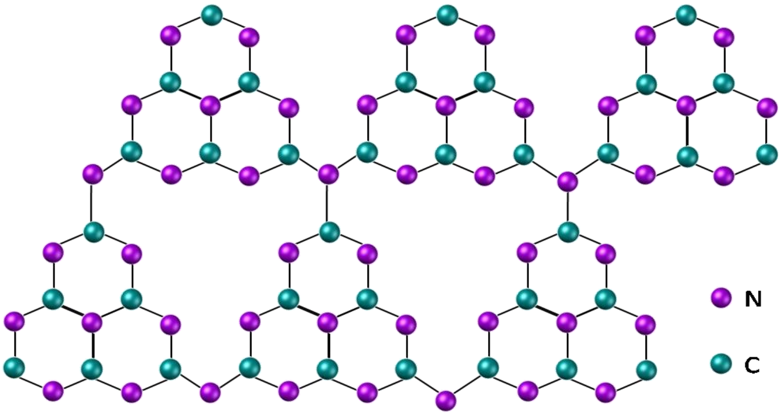

Figure 6.1 An atomic layer of g-C_3N_4 with heptazine building units. Layers are bonded to each other by weak van der Waals force.

On the other hand, photovoltaic applications and light emitting diodes of g-C_3N_4 have been reported [135-137]. Therefore, apart from HER, g-C_3N_4 is shown to have potential for optoelectronic applications. It has been reported that g-C_3N_4 nanostructures are a more efficient light absorber than its bulk counterpart, and a higher photoresponse has been obtained as compared to the bulk [138]. These precedential studies motivate us to investigate UV photodetectors based on the g-C_3N_4 nanosheets.

ZnO nanostructures has used to be a popular choice for UV sensing material. It has a bandgap of 3.37 eV [139], which inevitably makes it less sensitive to the UVA spectrum from 3.1 to 3.3 eV. This energy range is above the bandgap of g-C_3N_4. (UVA covers electromagnetic wave with energy 3.1 - 3.9 eV.) In this regard, g-C_3N_4 could be promising to fill in this gap as efficient UVA sensing material. Furthermore, g-C_3N_4 has a layered structure, which implies that its bandgap maybe enlarged to desirable extent by managing its thickness and/or lateral dimension. This could enable fine tuning of its bandgap such that a visible-blind UVA detector maybe anticipated from g-C_3N_4.

One of the difficulties in utilizing nanostructures for optoelectrical applications is inefficient charge conduction. Bulk g-C_3N_4 has been reported to have a low conductivity of the order 10^{-11} S/m [140]. Studies of nanostructures, especially films made of colloidal quantum dots, have shown that quantum dots do not support band-like transport, and have lower mobility than bulk films [141]. Therefore, employing g-C_3N_4 nanosheets for electrical conduction may significantly hinder the transport of photoexcited carriers and leads to large carrier loss via recombination. One way to tackle this problem is to complement the nanostructures with high mobility material. In this project, graphene was selected for this purpose.

6.1 Fabrication of devices

Synthesis of graphene by CVD method and bulk g-C_3N_4 powders are described in previous section. The g-C_3N_4 powders were further processed into nanosheets by sonication. The g-C_3N_4 powders were dispersed in IPA at a concentration of 1 mg/ml, and was ultrasonicated for 12 hrs and then centrifuged at 3000 rpm for 10 min. The supernatant was collected and the g-C_3N_4 nanosheets were used for device fabrication [142].

Poly(methyl methacrylate) (PMMA) was spin-coated onto graphene/copper foil before transfer of graphene. Copper foil was dissolved in ammonium persulfate (0.1 M) solution overnight. The graphene/PMMA was transferred to DI water bath for 3 times before finally transferred to 300 nm SiO_2/Si substrate. It was dried in ambient condition overnight and then heated at 110 °C for 15 min to enhance the adhesion of graphene to the substrate. PMMA was dissolved in 60 °C acetone bath for at least 4 hrs. Interdigitated electrodes were fabricated on graphene using standard photolithography. The electrodes consisted of 21 fingers, each with a width of 25 μm, a separation of 15 μm and a length of 1150 μm. Au (~100 nm) was deposited by thermal evaporation and the photoresist was lifted-off in acetone. 150 μl of g-C_3N_4 solution was dropped-casted onto the electrodes and the solvent was evaporated at 65 °C. The device was then transferred to a nitrogen-filled glove box and was heated at

150 ºC for 2 hrs to remove adsorbates before measurements. Electrical measurements were carried out with a semiconductor parameter analyzer (Agilent 4156C) and the light source was a 370 nm LED. In wavelength-dependent responsivity measurement, the light sources were five LEDs with peak wavelength at 410, 550, 660, 895 and 940 nm. Optical power was measured with a calibrated power meter.

6.2 Results and discussions

6.2.1 Characterization of g-C_3N_4, graphene and their hybrid

The TEM images of the g-C_3N_4 nanosheets are shown in Figure 6.2. The nanosheets are irregular in shapes. As seen from (b), some sheets appear porous and crumpled. From a higher resolution TEM image in (d), no lattice fringes could be observed from the sheets, suggesting that they are highly disordered.

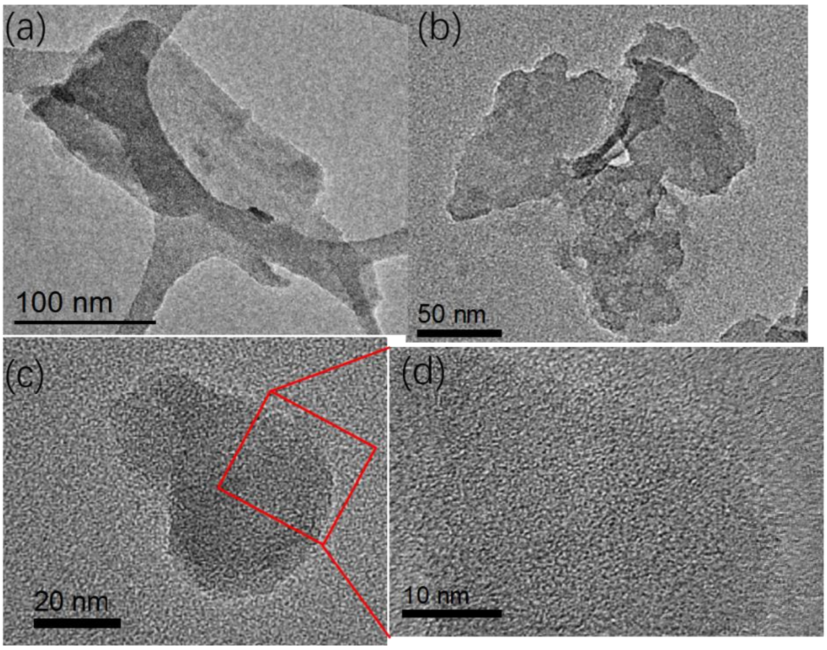

Figure 6.2 (a-c) TEM images of the g-C_3N_4 nanosheets. Porous structure can be seen in (b). (d) is the enlarged part of (c) indicated with the red square. No lattice fringes could be observed from the g-C_3N_4 nanosheets.

The thicknesses of the g-C_3N_4 nanosheets are further investigated by AFM as shown in Figure 6.3.The nanosheets show no aggregation. The height analysis of the three nanosheets marked by dotted lines, are shown in (b), where the nanosheets have thicknesses ranging from 2.6 to 7 nm. The height distribution of the g-C_3N_4 nanosheets are analyzed as shown in (d). Thicknesses of 50 nanosheets from the AFM images in (a) and (c) were measured. The height distribution followed a Gaussian distribution. The heights of the nanosheets were below 20 nm and the majority were 4-8 nm thick. The lateral size of the g-C_3N_4 nanosheets are evaluated as shown in (e), which ranges from 30 to 200 nm. The TEM and AFM images verify that the g-C_3N_4 nanosheets were successfully synthesized and that liquid phase sonication is an effective route to produce g-C_3N_4 nanosheets.

The scanning electron microscopy (SEM) image of the g-C_3N_4 nanosheets/graphene heterostructure is shown in Figure 6.3(f). Graphene covers the whole image. The darker strips in the image are the puckers from the monolayer graphene transferred onto SiO_2/Si substrate. The g-C_3N_4 nanosheets are the dark-color dots. It could be seen that the nanosheets are distributed uniformly on graphene over large area (~10 μm^2 for the area of the figure), no aggregation of g-C_3N_4 is observed, which is consistent with the AFM images.

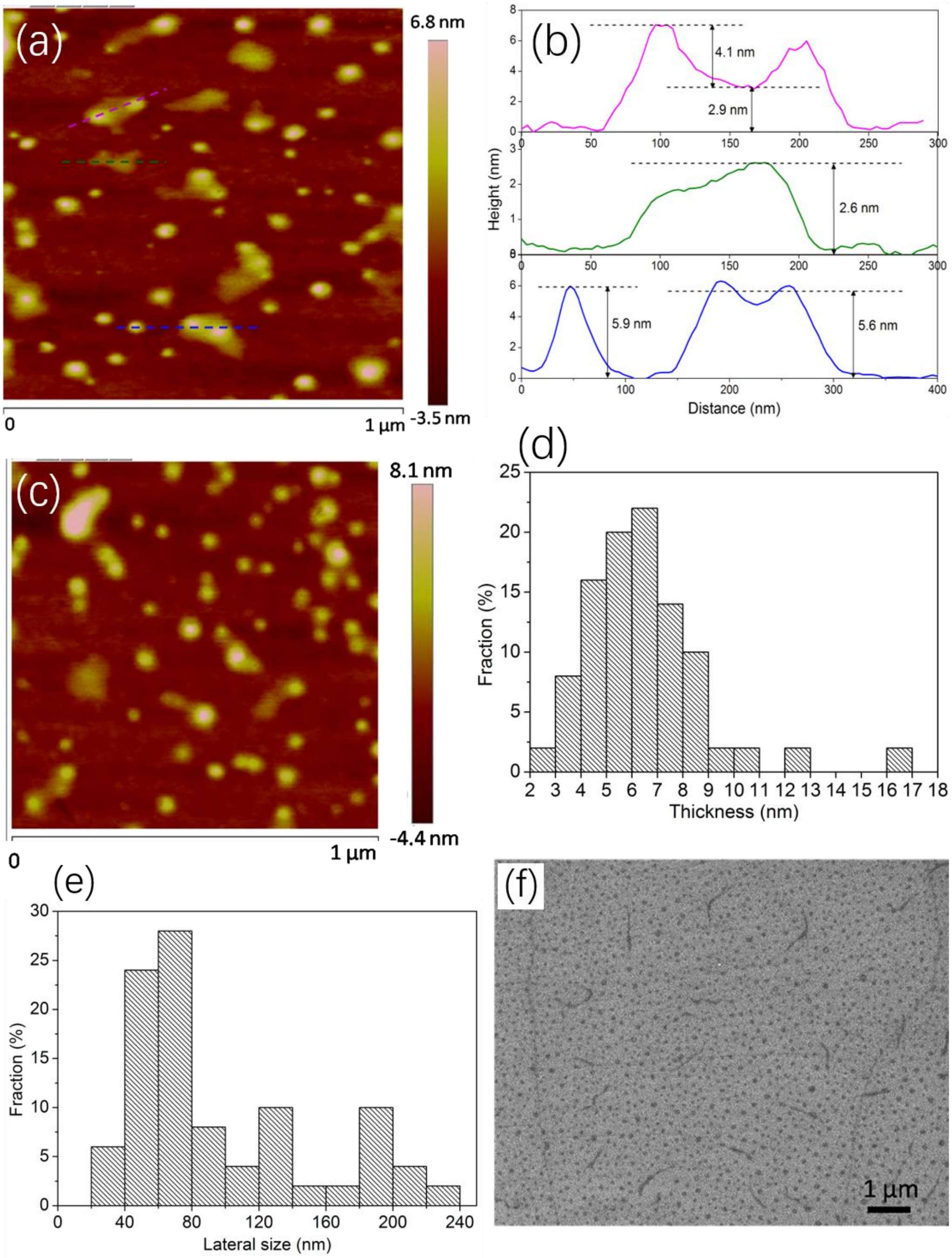

Figure 6.3 (a) and (c) AFM images of the g-C_3N_4 nanosheets. (b) The height analysis of the nanosheets marked with dotted lines in (a). (d) Height analysis obtained by measuring 50 g-C_3N_4 nanosheets. (e) Lateral size distribution of the g-C_3N_4 nanosheets. (f) SEM image of the g-C_3N_4 nanosheets/graphene heterostructure.

The XRD pattern of the g-C_3N_4 powders is shown in Figure 6.4(a). The peak at $2\theta=27.5^{o}$ is assigned to the set of (002) planes of graphitic substances with conjugated aromatic structure. The corresponding interlayer distance is 0.324 nm, which is consistent with reported studies [134, 143]. The peak is broad which may indicate stacking disorder that is well-known for attractive force originated from the non-directional π-πinteraction [144]. Another less pronounced peak at 2θ=12.9° is also commonly found in g-C_3N_4 and is assigned to the set of (100) plane. The interlayer distance is 0.686 nm and is related to the in-plane nitrogen repeating units [143].

The FTIR of the g-C_3N_4 powders was carried out to investigate the chemical bonding in the material. Figure 6.4(b) shows the sharp absorption peak at 809 cm^{-1} corresponds to the characteristic out-of-plane vibration of the tri-s-triazine rings of g-C_3N_4 [145]. The peaks at 1246 cm^{-1} and 1325 cm^{-1} are attributed to stretching of C-N(-C)-C and C-NH-C respectively [138, 145]. Absorption band from 1400 to 1700 cm^{-1}, which consists of 4 peaks, are assigned to stretching of C=N and C-N [146].

Complementary to the FTIR study, XPS was carried out to gain more insight on the chemical constituents in the g-C_3N_4 nanosheets. Full-scan XPS in Figure 6.5(a) shows that the g-C_3N_4 nanosheets are composed of mainly nitrogen and carbon, and also a small amount (2.2 at%) of oxygen. The C/N atomic ratio is 0.70. This is in agreement with previous studies on polymeric g-C_3N_4, which reported a C/N atomic ratio ranging from 0.67 to 0.72 [136, 145, 147]. Incursion of small proportion of oxygen is commonly reported for polymeric g-C_3N_4. The oxygen maybe originated from adsorbed water and oxygen on the nanosheets [138, 146]. The N1s spectrum is deconvoluted with 3 peaks. The peak at 398.5 eV is resulted from sp^2- bonded nitrogen atoms in the triazine ring. The peak at 400.2 eV is resulted from tertiary nitrogen

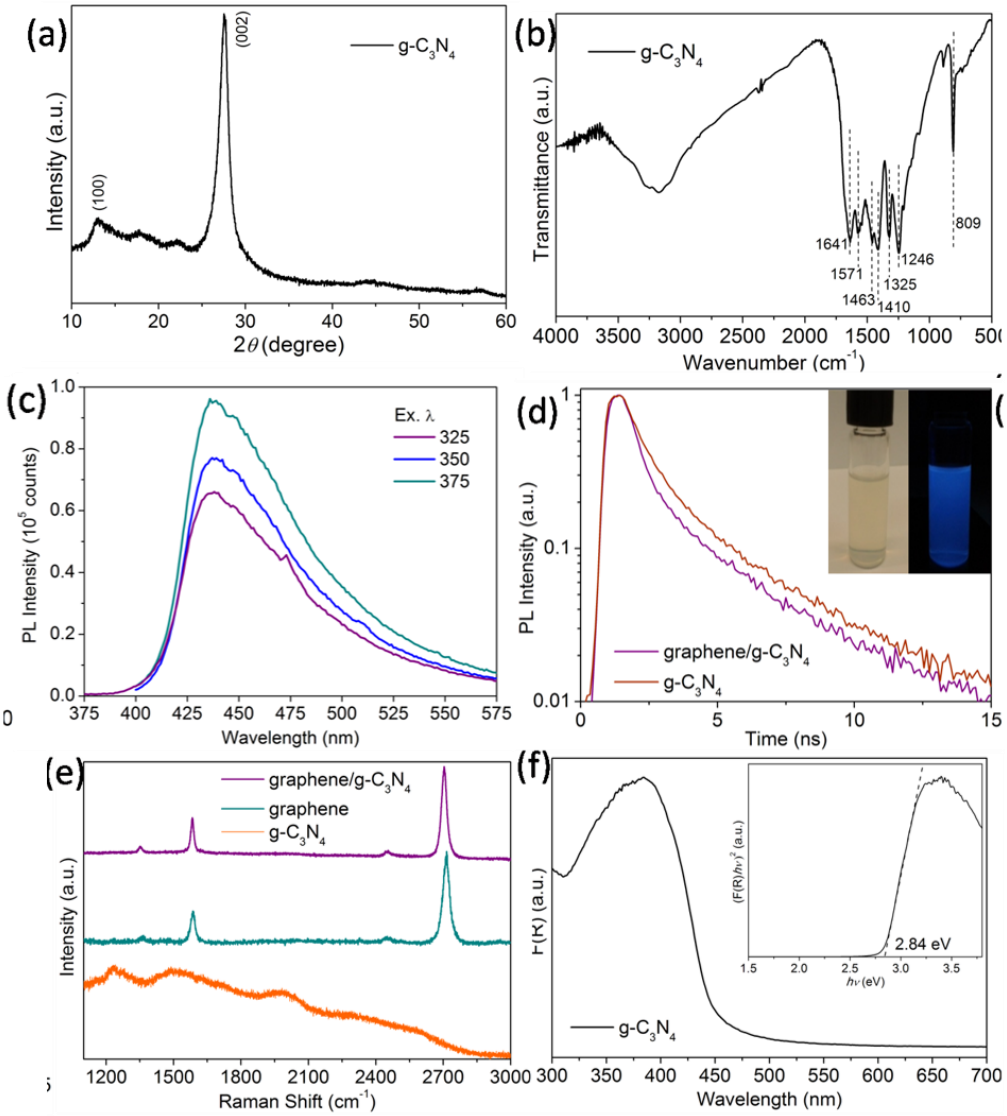

Figure 6.4 (a) The XRD spectrum of the g-C_3N_4 bulk powders. (b) FTIR of theg-C_3N_4 bulk powders. (c) PL spectra of the g-C_3N_4 nanosheets solution at different excitation wavelengths. (d) Time-resolved PL spectra of the g-C_3N_4 nanosheets and g-C_3N_4 nanosheets/graphene heterostructure. Inset is the photo of g-C_3N_4 nanosheets solution under white light (left) and UV light at 365 nm (right). (e) The Raman spectra of the g-C_3N_4 nanosheets, graphene and g-C_3N_4 nanosheets/graphene heterostructure. (f) The diffuse reflectance spectrum of the g-C_3N_4 bulk powders. Inset is the Tauc plot to find the optical band gap of the g-C_3N_4 bulk powders.

while the weaker peak at 404.6 eV is assigned to charge localization in cyano-group [148]. The C1s spectrum is deconvoluted with 2 peaks. The larger peak at 288.0 eV is assigned to sp^2 carbon in N=C(-N)$_2$ bonds. The peak at 284.6 eV is assigned to adventitious carbon in the graphitic domains [145].

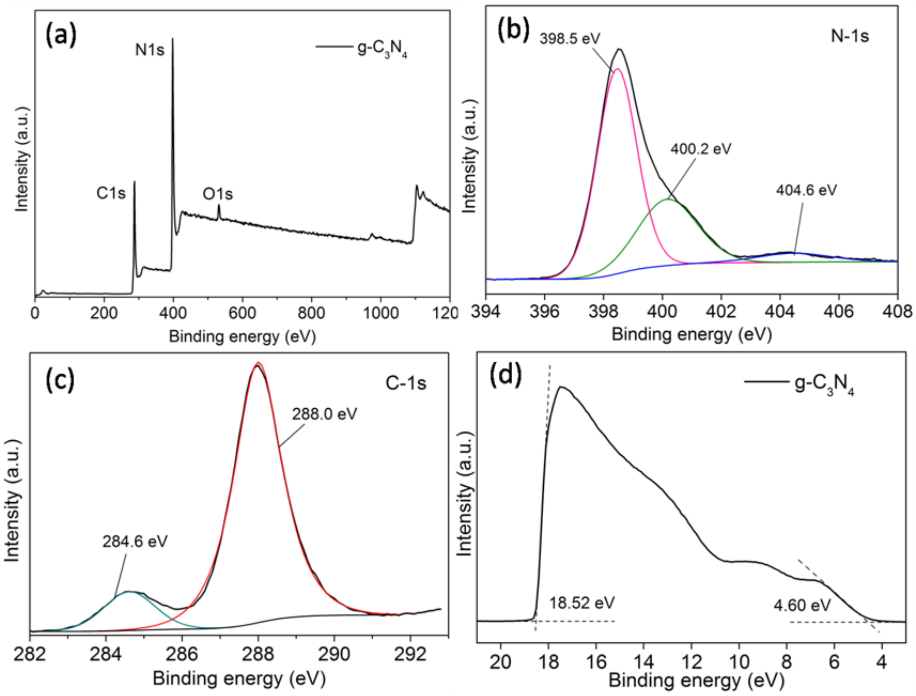

Figure 6.5 XPS and UPS spectra of the g-C$_3$N$_4$ nanosheets. (a) Full scan XPS spectrum. (b) The N-1s XPS spectrum. (c) The C-1s XPS spectrum. (d) The UPS spectrum.

The optical properties of the g-C$_3$N$_4$ nanosheets are characterized in the following section. The g-C$_3$N$_4$ nanosheets dispersed in IPA exhibits a blue PL with the peak locates at ~440 nm under UV excitation from 325 to 375 nm as shown in Figure 6.4 (c) and the inset of Figure 6.4(d). The PL peak position does not show significant shift with excitation wavelength, though it is observed that the PL intensity increases as the excitation wavelength red-shifted. This could be explained by the enhanced absorption of g-C_3N_4 from 325 to 375 nm as shown in the uv-vis spectrum in Figure 6.4 (f). The PL quantum yield of the g-C_3N_4 nanosheets was measured, with a value of 7.92%.

The emergence of PL indicates that exciton could be efficiently generated in the g-C_3N_4 nanosheets, but the crucial problem for the applications in photovoltaics, photodetection and photocatalysis would be to extract free carriers from the photogenerated excitons. One way is to form hybrid materials where the interface between the hybrid materials could have built-in electric field to facilitate charge transfer [135]. One of the signatures of charge transfer would be a quench in the PL intensity and a decrease in PL lifetime [149, 150]. Several computational works have already predicted a significant charge transfer between graphene and g-C_3N_4 monolayer due to the formation of electron-hole puddles between g-C_3N_4/graphene interface as a result of the non-uniform electron distribution in the g-C_3N4 lattice [151, 152].

The charge transfer property is investigated by the time-resolved PL measurement of the g-C_3N_4 nanosheets and g-C_3N_4 nanosheets/graphene heterostructure as shown in Figure 6.4(d). The average decay lifetime of the pristine g-C_3N_4 nanosheets and the hybrid are calculated to be 4.34 and 3.90 ns respectively, through a method described in Chapter 3. The fitting parameters are tabulated in Table

6.1. The shorter PL lifetime of the g-C_3N_4 nanosheets/graphene heterostructure than pristine g-C_3N_4 nanosheets could be ascribed to the transfer of charges from g-C_3N_4 nanosheets to graphene in a timescale shorter than the PL lifetime, such that radiative recombination is suppressed [153].

Table 6.1 Fitting parameters for time-resolved PL measurements

Sample	τ_1 (ns)/ A_1	τ_2 (ns)/ A_2	τ_3 (ns)/ A_3	<τ> (ns)
g-C_3N_4 nanosheets/graphene	0.55/ 9209	2.98/ 2342	12.84/ 204	3.90
g-C_3N_4 nanosheets	0.75/ 7901	3.12/ 2969	14.77/ 211	4.34

The Raman spectra of the graphene, g-C_3N_4 nanosheets, and g-C_3N_4 nanosheets/graphene heterostructure are shown in Figure 6.4 (e). g-C_3N_4 nanosheets exhibit a strong fluorescent background when excited by 488 nm laser which overwhelm its characteristic peaks. Graphene has the G peak at 1590 cm^{-1} and the 2D peak at 2700 cm^{-1}. The former is resulted from in-plane vibration of sp^2 carbon and the latter is related to the second order scattering at the Brillouin zone boundary [154]. The intensity ratio of I_{2D}/I_G is larger than two, which indicates that the graphene is monolayer. No appreciable difference is observed in the Raman of the heterostructure as compared to that of graphene. It is worth mentioning that the D peak at 1350 cm^{-1}, which is related to defects in graphene, did not increase in intensity, thus indicates that the quality of graphene remains high after the introduction of g-C_3N_4 nanosheets.

The absorption spectrum of the g-C_3N_4 is shown in Figure 6.4(f), where the diffuse reflectance spectrum was measured and then converted to absorption using the Kubelka-Munk function (F(R)). The F(R) values are proportional to the absorption coefficient. As seen from the figure, the g-C_3N_4 absorbs strongly in the UVA region. Absorption begins at 440 nm and peaks at 385 nm. The inset shows the Tauc plot, in which the optical band gap is determined to be 2.84 eV. This value coincides with the PL peak at 440 nm.

6.2.2 Electrical measurements

Figure 6.6(a) shows the schematic diagram of the device structure. The degenerately doped silicon was used as the back gate. A photo of the interdigitated electrode employed in the device is shown in the inset of Figure 6.7(a). Electrical measurements were conducted in nitrogen atmosphere unless otherwise specified.

Transfer characteristics of the device is shown in Figure 6.6(b). Under UV light illumination, the transfer curve migrates towards negative gate voltage direction. As the light intensity is increased gradually, the curve shifts continuously towards the left. This illustrates that the graphene is n-doped under the generation of electron-hole pairs in the device [139]. This further implies that electron is transferred to graphene from $g\text{-}C_3N_4$ nanosheets under illumination, since $g\text{-}C_3N_4$ nanosheets are the major light absorber in the device when considering that graphene is only one-atom thick. This is in agreement with the findings from time-resolved PL measurement where charge transfer existed in the $g\text{-}C_3N_4$ nanosheet/graphene heterostructure. To further ascertain that electrons are transferred from $g\text{-}C_3N_4$ to graphene, the band diagram of the $g\text{-}C_3N_4$ nanosheet/graphene heterostructure is analyzed in Figure 6.6(c). From the ultraviolet electron spectroscopy (UPS) measurement in Figure 6.5 (d), the valance band edge (VB) of the $g\text{-}C_3N_4$ nanosheets is found to be at -7.3 eV. (The He Iα emission line with energy 21.22 eV was used in the UPS measurement.) Neglecting excitonic influence, using the optical band gap value determined above, the conduction band edge (CB) is found to be at -4.46 eV. The Fermi level (E_F) of the $g\text{-}C_3N_4$ was reported to be at ~2.39 eV above VB [155] while that of graphene is at ~4.6 eV [156]. Upon reaching equilibrium, a built-in electric field exists at the $g\text{-}C_3N_4$/graphene interface. This E-field assists photogenerated electron-hole pairs to dissociate at the interface, as it promotes electrons drifting towards graphene, while holes are drifted towards $g\text{-}C_3N_4$ in an opposite direction with electrons. Figure 6.6(d) demonstrates that the photocurrent can be controlled by the gate voltage to a large extent. The photocurrent switches sign when the gate voltage is swept pass the Dirac point. Photocurrent equals zero when the gate voltage is nearby the Dirac point. This variation of photocurrent is explained with the change in the Fermi level position due to the gate voltage which is schematically illustrated inside the Figure 6.6 (d). The density of states for free carriers changes with the Fermi levels position in graphene. While gate voltage modulates the Fermi level of graphene, the difference in the free carriers density between devices under illumination and in dark lead to the negative to positive change of photocurrent. It has been shown that gate voltage could change the sign of photocurrent, which has also been reported in some phototransistors, and this normally could not be achieved by modulating only the source-drain voltage. The sign of photocurrent (+/-) could be used as the on/off signature when using graphene-based devices as photoswitches which generally has low I_{light}/I_{dark} ratio (I is the current) due to large dark current.

The normalized responsivity at various wavelengths is shown in Figure 6.7(a). Light intensity is maintained at 200 µW/cm^2 at different wavelengths. The responsivity follows a trend similar to the absorption of g-C_3N_4, this verifies that the g-C_3N_4 nanosheets are the major light absorber in the device, as graphene has a nearly constant absorption of only ~2.3% in this wavelength range, as mentioned in Chapter 2. Responsivity increases for wavelength shorter than ~410 nm, thus demonstrates that the devices are especially suitable for UVA detection.

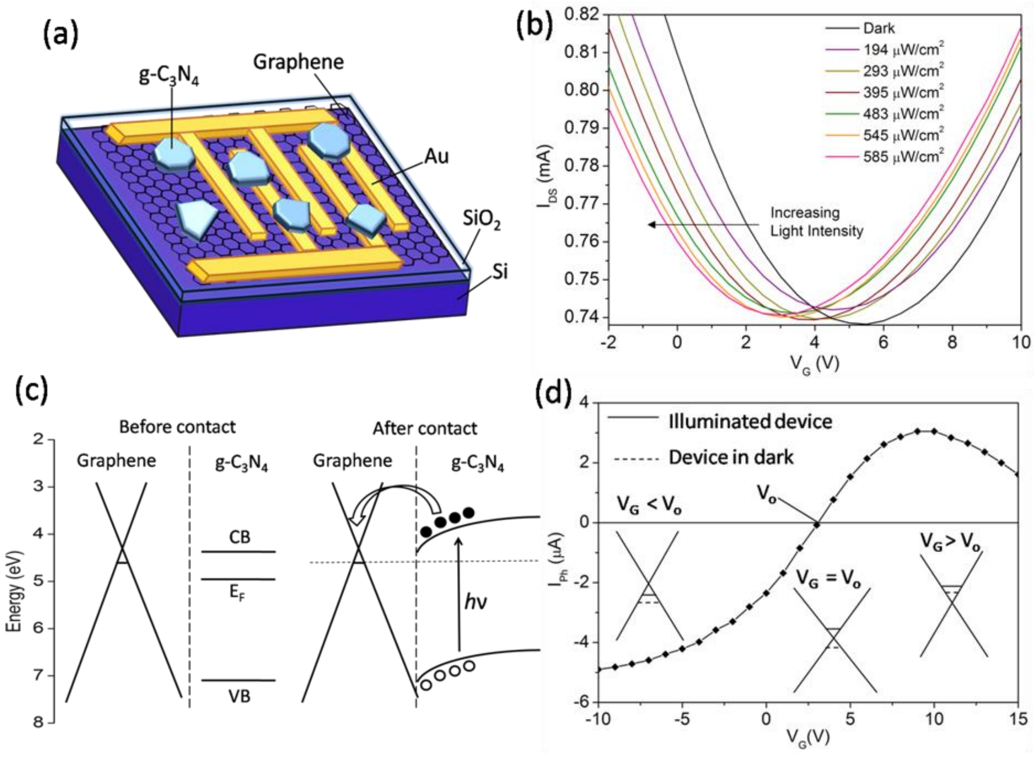

Figure 6.6 (a) Schematic diagram of the device structure. (b) Transfer curves of the device under various light intensities. The applied V_{DS} is 0.5 V and excitation wavelength is 370 nm. (c) Band diagram analysis of the g-C_3N_4 nanosheets/graphene hybrid. (d) Photocurrent as a function of the gate voltage. V_O denotes the gate voltage where photocurrent is zero.

From Figure 6.7(b), the photocurrnet increases with source-drain voltage (V_{DS}) in a linear way, where the gate voltage (V_G) is 5 V and light intensities are varied over 3 orders of magnitude. The relation between V_{DS} and the transit time (τ_{tr}) of electrons in the channeal is $\tau_{tr} = L^2/\mu V_{DS}$ [157], where μ is the carrier mobility, L is the channel length. Increase in V_{DS} reduces the electron transit time in channel, thus photocurrent increases under same recombination lifetime of electron.

In Figure 6.8(a), the responsivity increases when light intensity decreases, which has been observed before [121, 158]. Photogenerated free carriers will compensate the

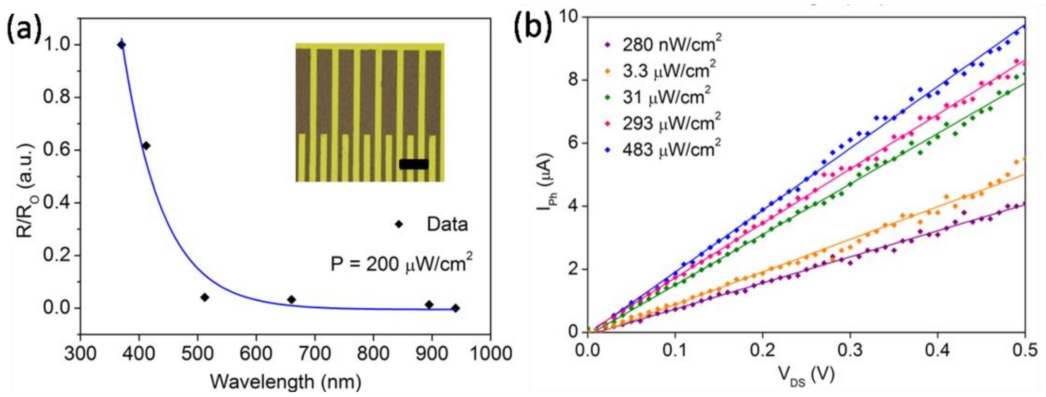

Figure 6.7 (a) The normalized responsivity at different wavelengths in the UV-Vis-NIR region. Inset shows a photo of the interdigitated electrodes employed in the device. Scale bar is 100 μm. (b) Photocurrent as a function of source-drain voltage at various light intensities spanned over 3 orders of magnitude.

built-in electric field, this effect becomes more prominent as light intenisty increases, therefore charge separation will be retarded. The highest responsivity reaches 4×10^3 AW^{-1}. A responsivity larger tha 1 AW^{-1} implies that there are more than one charge detected for each photon impinging the device. This parameter is often described by the gain. It is related to responsivity by the equation $R = I_{Ph}/P = \eta qG/h\nu$ [157], where $h\nu$ is the photon energy, q is the electron charge, η is the external quantum efficiency. The devices are found to exhibit a gain of at least 10^4.

Internal electric field promotes the dissociation of photogenerated electron-hole pairs. Electrons are drifted to graphene while holes are trapped in g-C_3N_4 nanosheets. Defects present in g-C_3N_4 is one of the sources of trap states, which could be generated as a result of the imperfect polymerization of g-C_3N_4 [159]. Trapped holes in g-C_3N_4 induce a negative charge in graphene through capacitive coupling, which is analoguous to applying a positive gate voltage to graphene, this is termed the photogating effect [160]. The induced negative charge is fulfilled by electrons circulating multiple times in the high mobility graphene channel within the recombination lifetime or the trapping lifetime of holes. This gives rise to the high gain in the device.

The dependence of photocurrent on light intensity is shown in Figure 6.8 (b). The data points were fitted with the power law $I_{ph} = aW^{\theta}$, where W is the light intensity. The value of θ obatined from fitting is 0.392. Therefore the photocurrent is highly non-linear with intensity. This is expected as the photogating effect is a non-linear process [161], unlike the photovoltaic effect.

Another important characterization of photodetectors would be their response under on/off cycles of light. This gives information on the response speed, the on/off ratio and bandwidth of the devices. In particular, in devices that involve trapping, persistent photoconductivity (PPC) may often be encountered [162, 163], where the change in current due to illumination does not recover back to the dark current level after light is turned off for a long period of time (seconds to minutes). Although this phenonmenon maybe useful in studying material-substrate interface or photoresponse mechanism, it is not practical for photodetector applications.

The photoresponse of the g-C_3N_4 nanosheets/graphene phototransistors is shown in Figure 6.8(c). The applied V_G and V_{DS} are 8 V and 0.5 V respectively. The g-C_3N_4 nanosheets/graphene heterostructure shows a large positive photocurrent of ~15 μA when the light is on (indicated by light-blue color in the figure), which recover back to dark current level when the light is off. For the graphene-only device, a smaller negative photocurrent could be observed under prolonged illumination and same biasing condition, which is opposite to the positive photocurrent in the hybrid device. This demonstrates that the g-C_3N_4 nanosheets play an important role in the photoresponse of the hybrid device.

The heterostructure exhibits synergistic effect that outperformed the individual component. This is achieved through utilizing the advantage of individaul component, which is the strong UV absorption in the g-C_3N_4 nanosheets and the high mobility of graphene. Electron-hole pairs are generated at the g-C_3N_4 nanosheets and graphene acted as the carrier transport layer in the devces.

Analysis of the response time of the devices is shown in Figure 6.8(d). Rise and decay time constants are obtained by fitting the data points with equations $I(t) = I_{dark} + A_1exp(t/\tau_{r1}) + A_2exp(t/\tau_{r2})$ for rise and $I(t) = I_{dark} + A_3exp(-t/\tau_{d1}) + A_4exp(-t/\tau_{d2})$ for decay, where t is time, $\tau_{r1,2}$ and $\tau_{d1,2}$ are the rise and decay time constants respectively. The device has a modest rise time constant τ_{r1} of 0.74s. The recovery time is slower than rise time by ~10 times. The time constants are listed in the figure. A much longer decay time can be attributed to the long relaxation lifetime of the trapped carriers. When the light is turned off, without new photogenerated carriers refilling the trapping sites, capacitive coupling relaxes slowly. The decay time constants can be a reference for the trapping lifttime of holes in the g-C_3N_4 nanosheets.

A lot of studies have reported that devices employing nanostructure would actively interact with the ambient environment due to their high surface-to-volume ratio with large a surface area expose to the surroundings [99, 139]. Since the active materials in the devices in this work are all nanostructures, photoresponse measurements have also been carried out in the ambience for comparison. Figure 6.9(a) shows the photoresponse of the g-C_3N_4 nanosheets/graphene devices. A negative photocurrent is found, and no positive photocurrent could be obtained by tuning the gate voltage across ±60V. Nonetheless, photoreponse is reproducible, it returns back to dark current level when the light is gone. In addition, the magnitude of negative photocurrent in the hybrid device is larger than that of the graphene-only device as shown in Figure 6.9(b), where a regular period of on and off of light is employed. The proposed mechanism for the large difference between the photoresponse in nitrogen atmosphere and air is shown in Figure 6.9(c-d). In ambient air, oxygen molecules adsorb on top of graphene are negatively charged or polarized, which diminishes the hole mobility in graphene through impurity scattering [162]. UV irradiation triggers the desorption of negatively-charged oxygen molecules by capturing photogenerated holes [99], this is more likely to occur on the surface of the g-C_3N_4 as it is more photoresponsive than graphene. The decrease in holes makes the g-C_3N_4 more negative and acts as additional scattering sites to holes in graphene, the hole mobility in graphene is further reduced under UV light and results in a negative photocurrent.

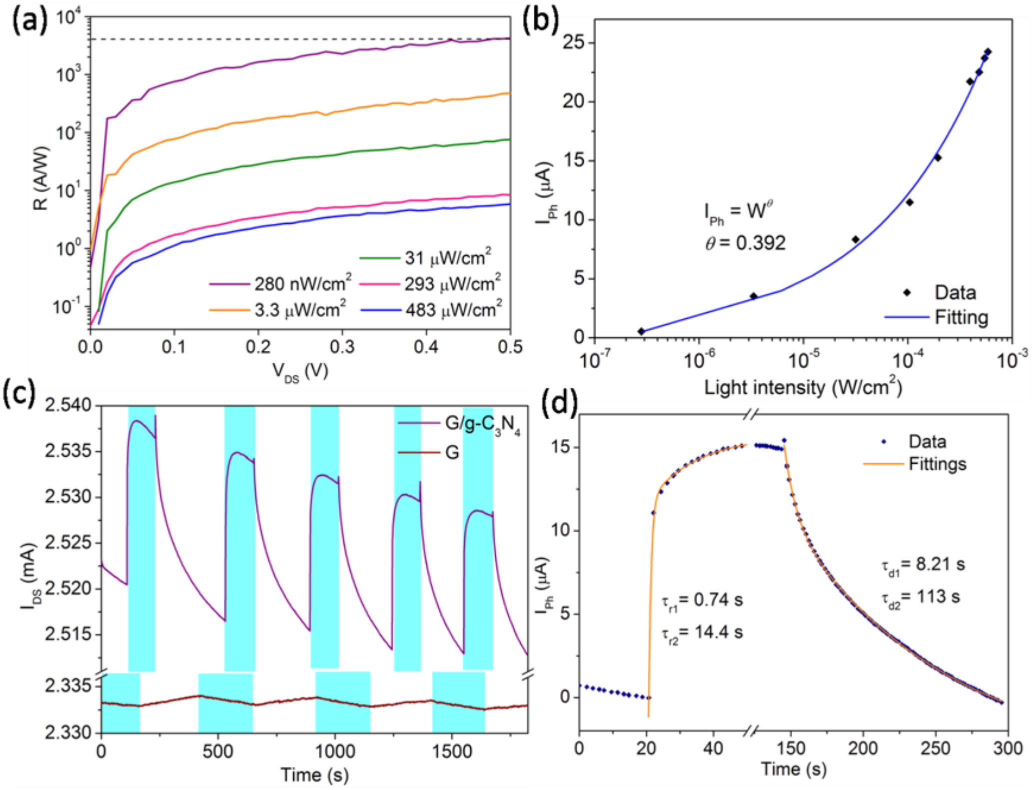

Figure 6.8 (a) Responsivity for different light intensities. The maximum responsivity obtained is indicated by the dotted line. (b) Dependence of photocurrent on light intensity. Blue line is the fitting by power law. (c) Response of the g-C_3N_4 nanosheets/graphene heterostructure devices and the graphene-only device. Blue regions are time interval when the light is switched on and white regions are time when the light is switched off. (d) Fittings to extract the rise and decay time constants of the g-C_3N_4 nanosheets/graphene devices. Time constants were tabulated in the figure.

The stability of the g-C_3N_4 nanosheets/graphene phototransistors was investigated. The devices were stored in the ambient air in dark for more than 130 days

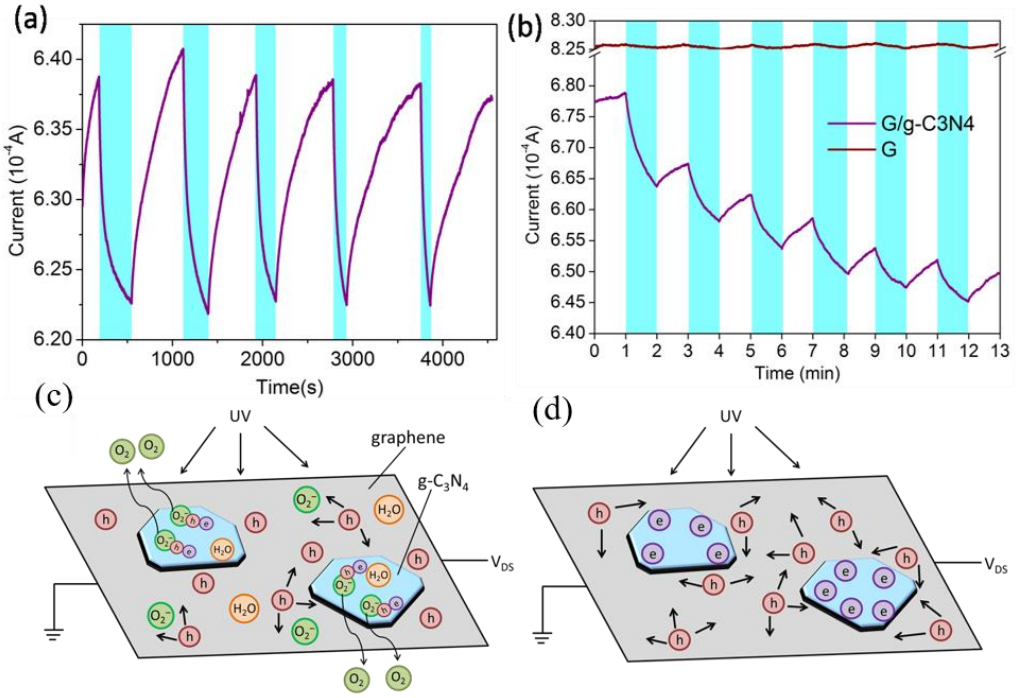

Figure 6.9 (a) Photoresponse of the g-C_3N_4 nanosheets/graphene device in the ambient air. (b) Comparison of the negative photocurrent from the graphene-only device and g-C_3N_4 nanosheets/graphene devices under periodic on and off of light in 60 s intervals. (c) Illustration of the desorption of oxygen under UV light in the air. (d) Illustration of the enhanced scattering of holes in graphene in the air under UV.

and the photoresponse were measured. The results are shown in Figure 6.10. The devices were transferred into nitrogen glovebox and underwent same mild heating treatment as the fresh devices before measurements. Figure 6.10(a) shows the left-shift of transfer curves with increasing light intensity which is consistent with fresh devices. A responsivity of the order 10^3 A/W could still be obtained as shown in Figure 6.10(b). Reproducible photoresponse under on and off of light is observed as before as shown in Figure 6.10(c). Large, positive photocurrent of 25 μA is found. These show that the g-C_3N_4 nanosheets/graphene phototransistors has high stability in air and demonstrate no sign of degradation after at least 130 days.

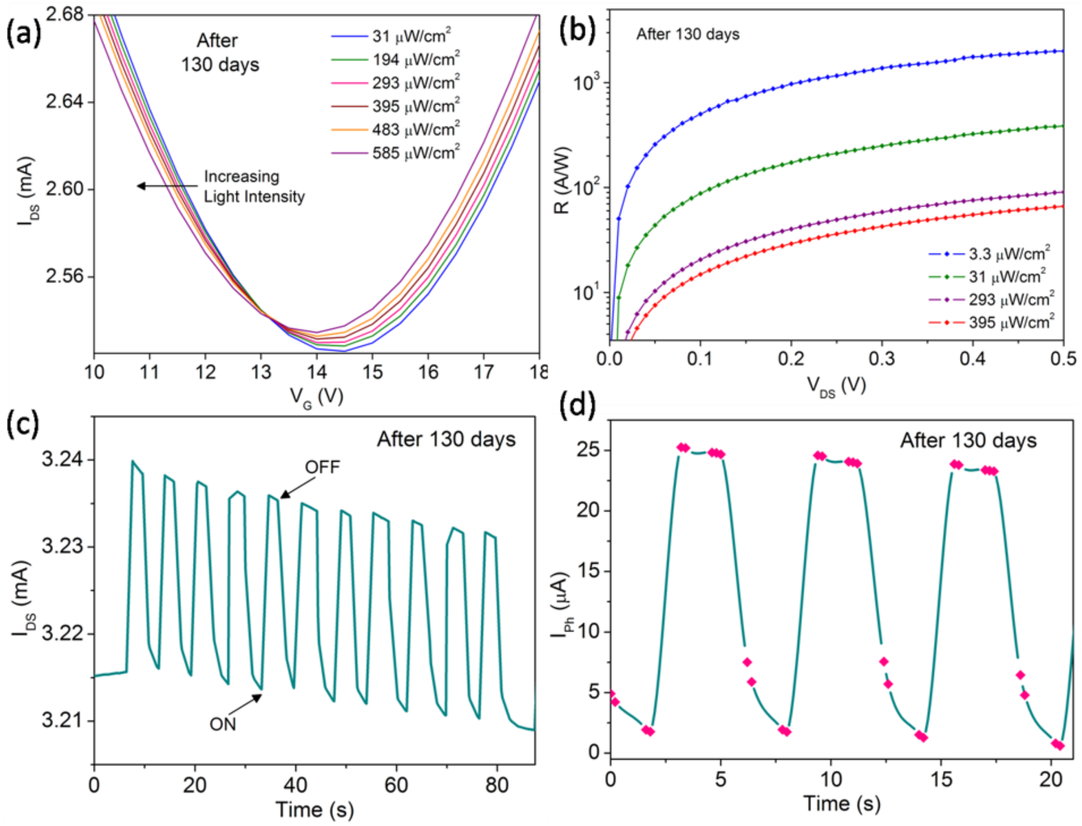

Figure 6.10 Photoresponse measurements of the device that was stored in air for 130 days. (a) Transfer characteristics at different light intensities. (b) A responsivity of the order 10^3 A/W could be obtained, which is same as the freshly made device (c) Reproducible photocurrent upon on/off cycles. (d) A large, positive photocurrent of 25 μA could be obtained.

Chapter 7 Conclusions and future works

7.1 Conclusions

In this project, graphene-based nanostructures of various forms including 2-D monolayer, 0-D quantum dots and multilayer nanosheets have been employed for photodetection. The layered nature in these graphene-based materials enables engineering in their thicknesses which simultaneously engineer their electronic structures. In addition, different device architectures for photodetectors have been investigated, including the vertical junction PRGO nanosheet devices with build-in electric field; the lateral architecture of PANI-GQDs devices with symmetrical structure having large exposed surface area that get photoresponse from interaction with the ambience; and the phototransistors based on g-C_3N_4 nanosheets/graphene with large gate-tunable photocurrent.

The versatility of carbon nanostructures for photodetection has been revealed. The PRGO nanosheets have tunable spectral ranges for detection. A satisfactory responsivity of 23 mA/W has been obtained from the ultrathin active layer of ~50-70 nm in the devices, and a response time of ~100 ms has been acquired, which is at least one order of magnitude faster than reported GO-based photodetectors. Another way to tailor the optoelectronic properties of graphene-based nanomaterials has been achieved through the chemical functionalization of GQDs. Composite formation of GQDs with PANI has been adopted to show the enhanced capability of GQDs. The PANI-GQDs nanocomposite exhibited a responsivity an order of magnitude higher than the GQDs. Rise and decay time scales of PANI-GQDs device is also two and four folds faster than GQDs device respectively. The photocurrent in the PANI-GQDs and GQDs devices switch sign at large bias voltage, which is an interesting property that could be exploited as signal carrier. Lastly, heterostructure made of two graphene-based nanomaterials, monolayer graphene and graphitic carbon nitride nanosheets, are investigated for phototransistors. A high responsivity of an order 10^3 A/W could readily be obtained from the devices. The sign of the photocurrent could be controlled by gate voltage which could be one way to circumvent the low on/off ratio in graphene devices that allow them to be applied as photoswitches by utilizing the sign of photocurrent. It has been shown in this project that graphene nanostructures are highly flexible to be made suitable for different photodetection mechanisms that enable gain or linearity depending on needs.

7.2 Future works

Some graphene-based nanostructures, like monolayer graphene, RGO and the glucose-derived PRGO introduced in this project, have demonstrated potential for long wavelength photodetection in the infrared and/or terahertz regime. These spectral ranges have important applications in telecommunications, military, space technology etc., and after all, silicon technology has already been developed very maturely and efficiently for detection in the NIR-visible-UV regime. It is therefore valuable and scientifically important to explore photodetection for the long wavelength spectrum mentioned above.

It has been reported that defects in graphene could enhance the responsivity for photodetection, including in the mid-infrared region [164]. In fact, for our prototype devices employing PRGO, where optimization in the annealing temperature and device structure have not yet been carried out, the photocurrent reaches 80 nA at 1610 nm. The PRGO is believed to be highly defective, due to the amorphous nature in the as-synthesized GO, thermal annealing that lead to random changes of sp^3 to sp^2 domains, and multiple transfer processes employed in device fabrication. In future work, the potential of PRGO for mid-infrared and terahertz photodetection would be investigated as it has already shown reasonable response in the NIR regime. The relations of defects (defect types, density, energy level of defects, formation ways etc.) with photoresponse and the control of defects in PRGO would be a few interesting and useful topics of investigation.

References

1. H. W. Kroto, J. R. Heath, S. C. O'Brien, R. F. Curl and R. E. Smalley, *Nature*, 1985, **318**, 162-163.
2. T. Ebbesen and A. P M, *Nature*, 1992, **358**, 16.
3. B. C. Thompson and J. M. Frechet, *Angew Chem Int Ed Engl*, 2008, **47**, 58-77.
4. R. S. Ruoff, D. Qian and W. K. Liu, *Comptes Rendus Physique*, 2003, **4**, 993-1008.
5. B. Q. Wei, R. Vajtai and P. M. Ajayan, *Applied Physics Letters*, 2001, **79**, 1172-1174.
6. K. S. Novoselov, A. K. Geim, S. V. Morozov, D. Jiang, Y. Zhang, S. V. Dubonos, I. V. Grigorieva and A. A. Firsov, *science*, 2004, **306**, 666-669.
7. Y. Zhu, S. Murali, W. Cai, X. Li, J. W. Suk, J. R. Potts and R. S. Ruoff, *Adv Mater*, 2010, **22**, 3906-3924.
8. S. Pei and H.-M. Cheng, *Carbon*, 2012, **50**, 3210-3228.
9. B. Partoens and F. M. Peeters, *Physical Review B*, 2006, **74**.
10. C. Gómez-Navarro, R. T. Weitz, A. M. Bittner, M. Scolari, A. Mews, M. Burghard and K. Kern, *Nano letters*, 2007, **7**, 3499-3503.
11. X. Li, X. Wang, L. Zhang, S. Lee and H. Dai, *science*, 2008, **319**, 1229-1232.
12. D. Pan, J. Zhang, Z. Li and M. Wu, *Adv Mater*, 2010, **22**, 734-738.
13. X. Wang, K. Maeda, X. Chen, K. Takanabe, K. Domen, Y. Hou, X. Fu and M. Antonietti, *Journal of the American Chemical Society*, 2009, **131**, 1680-1681.
14. K. Mathieson, J. Loudin, G. Goetz, P. Huie, L. Wang, T. I. Kamins, L. Galambos, R. Smith, J. S. Harris, A. Sher and D. Palanker, *Nat Photonics*, 2012, **6**, 391-397.
15. X. An, F. Liu, Y. J. Jung and S. Kar, *Nano Lett*, 2013, **13**, 909-916.
16. F. P. García de Arquer, A. Armin, P. Meredith and E. H. Sargent, *Nature Reviews Materials*, 2017, **2**, 16100.
17. K. S. Novoselov, A. K. Geim, S. V. Morozov, D. Jiang, M. I. Katsnelson, I. V. Grigorieva, S. V. Dubonos and A. A. Firsov, *Nature*, 2005, **438**, 197-200.
18. A. K. Geim and K. S. Novoselov, *Nature materials*, 2007, **6**, 183-191.
19. Y. Zhang, Y. W. Tan, H. L. Stormer and P. Kim, *Nature*, 2005, **438**, 201-204.
20. H. Z. Lu, W. Yao, D. Xiao and S. Q. Shen, *Phys Rev Lett*, 2013, **110**, 016806.
21. A. Rycerz, J. Tworzydło and C. W. J. Beenakker, *Nature Physics*, 2007, **3**, 172-175.
22. D. Xiao, W. Yao and Q. Niu, *Phys Rev Lett*, 2007, **99**, 236809.
23. X. Xu, W. Yao, D. Xiao and T. F. Heinz, *Nature Physics*, 2014, **10**, 343-350.
24. R. R. Nair, P. Blake, A. N. Grigorenko, K. S. Novoselov, T. J. Booth, T. Stauber, N. M. Peres and A. K. Geim, *Science*, 2008, **320**, 1308-1308.

25. T. Kleine-Ostmann and T. Nagatsuma, *Journal of Infrared, Millimeter, and Terahertz Waves*, 2011, **32**, 143-171.
26. H.-J. Song and T. Nagatsuma, *IEEE Transactions on Terahertz Science and Technology*, 2011, **1**, 256-263.
27. L. Vicarelli, M. S. Vitiello, D. Coquillat, A. Lombardo, A. C. Ferrari, W. Knap, M. Polini, V. Pellegrini and A. Tredicucci, *Nat Mater*, 2012, **11**, 865-871.
28. B. Sensale-Rodriguez, R. Yan, M. M. Kelly, T. Fang, K. Tahy, W. S. Hwang, D. Jena, L. Liu and H. G. Xing, *Nature Communications*, 2012, **3**, 780.
29. A. K. Geim and I. V. Grigorieva, *Nature*, 2013, **499**, 419-425.
30. X. Chen, N. C. Berner, C. Backes, G. S. Duesberg and A. R. McDonald, *Angew Chem Int Ed Engl*, 2016, **55**, 5803-5808.
31. J. E. Johns and M. C. Hersam, *Accounts of chemical research*, 2012, **46**, 77-86.
32. D. Chen, H. Feng and J. Li, *Chem Rev*, 2012, **112**, 6027-6053.
33. K. P. Loh, Q. Bao, G. Eda and M. Chhowalla, *Nat Chem*, 2010, **2**, 1015-1024.
34. L. Sygellou, G. Paterakis, C. Galiotis and D. Tasis, *The Journal of Physical Chemistry C*, 2016, **120**, 281-290.
35. Z. Liu, J. Li, Z.-H. Sun, G. Tai, S.-P. Lau and F. Yan, *ACS nano*, 2011, **6**, 810-818.
36. J. Abraham, K. S. Vasu, C. D. Williams, K. Gopinadhan, Y. Su, C. T. Cherian, J. Dix, E. Prestat, S. J. Haigh, I. V. Grigorieva, P. Carbone, A. K. Geim and R. R. Nair, *Nat Nanotechnol*, 2017, **12**, 546-550.
37. Y. Sun, S. Wang, C. Li, P. Luo, L. Tao, Y. Wei and G. Shi, *Phys Chem Chem Phys*, 2013, **15**, 9907-9913.
38. J. Shen, Y. Zhu, X. Yang and C. Li, *Chem Commun (Camb)*, 2012, **48**, 3686-3699.
39. Y. Wang, X. Wang and M. Antonietti, *Angew Chem Int Ed Engl*, 2012, **51**, 68-89.
40. Q. Xiang, J. Yu and M. Jaroniec, *The Journal of Physical Chemistry C*, 2011, **115**, 7355-7363.
41. S. C. Yan, Z. S. Li and Z. G. Zou, *Langmuir*, 2009, **25**, 10397-10401.
42. G. Konstantatos and E. H. Sargent, *Nat Nanotechnol*, 2010, **5**, 391-400.
43. C. Xie, C. Mak, X. Tao and F. Yan, *Advanced Functional Materials*, 2017, **27**, 1603886.
44. F. Perry, *Boston Electronics Corporation*, 2003, **72**.
45. F. Guo, B. Yang, Y. Yuan, Z. Xiao, Q. Dong, Y. Bi and J. Huang, *Nat Nanotechnol*, 2012, **7**, 798-802.
46. A. Armin, M. Hambsch, I. K. Kim, P. L. Burn, P. Meredith and E. B. Namdas, *Laser & Photonics Reviews*, 2014, **8**, 924-932.
47. A. H. Titus, M. C. Cheung and V. P. Chodavarapu, in *Photodiodes-World Activities in 2011*, InTech, 2011.
48. X. Gong, M. Tong, Y. Xia, W. Cai, J. S. Moon, Y. Cao, G. Yu, C.-L. Shieh, B. Nilsson

and A. J. Heeger, *Science*, 2009, **325**, 1665-1667.

49. D. V. Perepelitsa, *Dept. of Physics, MIT*, 2006.
50. M. S. Arnold, J. D. Zimmerman, C. K. Renshaw, X. Xu, R. R. Lunt, C. M. Austin and S. R. Forrest, *Nano letters*, 2009, **9**, 3354-3358.
51. G. Konstantatos, J. Clifford, L. Levina and E. H. Sargent, *Nature Photonics*, 2007, **1**, 531-534.
52. F. H. Koppens, T. Mueller, P. Avouris, A. C. Ferrari, M. S. Vitiello and M. Polini, *Nat Nanotechnol*, 2014, **9**, 780-793.
53. X. Xu, N. M. Gabor, J. S. Alden, A. M. van der Zande and P. L. McEuen, *Nano Lett*, 2010, **10**, 562-566.
54. Z. Sun and H. Chang, *ACS nano*, 2014, **8**, 4133-4156.
55. L. Tang, X. Li, R. Ji, K. S. Teng, G. Tai, J. Ye, C. Wei and S. P. Lau, *Journal of Materials Chemistry*, 2012, **22**, 5676-5683.
56. S. K. Lai, L. Tang, Y. Y. Hui, C. M. Luk and S. P. Lau, *Journal of Materials Chemistry C*, 2014, **2**, 6971-6977.
57. L. Tang, R. Ji, X. Cao, J. Lin, H. Jiang, X. Li, K. S. Teng, C. M. Luk, S. Zeng and J. Hao, *ACS nano*, 2012, **6**, 5102-5110.
58. X. Li, W. Cai, J. An, S. Kim, J. Nah, D. Yang, R. Piner, A. Velamakanni, I. Jung and E. Tutuc, *Science*, 2009, **324**, 1312-1314.
59. P. Niu, L. Zhang, G. Liu and H. M. Cheng, *Advanced Functional Materials*, 2012, **22**, 4763-4770.
60. U. Maver, T. Velnar, M. Gaberšček, O. Planinšek and M. Finšgar, *TrAC Trends in Analytical Chemistry*, 2016, **80**, 96-111.
61. M. B. Fenn, P. Xanthopoulos, G. Pyrgiotakis, S. R. Grobmyer, P. M. Pardalos and L. L. Hench, *Advances in Optical Technologies*, 2011, **2011**.
62. C. Wei, X. Chen, D. Li, H. Su, H. He and J. F. Dai, *Sci Rep*, 2016, **6**, 33890.
63. W. Martienssen and H. Warlimont, *Springer handbook of condensed matter and materials data*, Springer Science & Business Media, 2006.
64. R. W. Meulenberg, J. R. Lee, A. Wolcott, J. Z. Zhang, L. J. Terminello and T. Van Buuren, *ACS nano*, 2009, **3**, 325-330.
65. M. M. Ugeda, A. J. Bradley, S. F. Shi, F. H. da Jornada, Y. Zhang, D. Y. Qiu, W. Ruan, S. K. Mo, Z. Hussain, Z. X. Shen, F. Wang, S. G. Louie and M. F. Crommie, *Nat Mater*, 2014, **13**, 1091-1095.
66. F. Xia, T. Mueller, Y.-m. Lin, A. Valdes-Garcia and P. Avouris, *Nature nanotechnology*, 2009, **4**, 839-843.
67. C.-H. Liu, Y.-C. Chang, T. B. Norris and Z. Zhong, *Nature nanotechnology*, 2014, **9**, 273-278.
68. Z. Xu, S. Lin, X. Li, S. Zhang, Z. Wu, W. Xu, Y. Lu and S. Xu, *Nano Energy*, 2016,

23, 89-96.

69. Y. Cao, J. Zhu, J. Xu, J. He, J. L. Sun, Y. Wang and Z. Zhao, *Small*, 2014, **10**, 2345-2351.
70. B. Chitara, S. Krupanidhi and C. Rao, *Applied Physics Letters*, 2011, **99**, 113114.
71. B. Chitara, L. Panchakarla, S. Krupanidhi and C. Rao, *Advanced Materials*, 2011, **23**, 5419-5424.
72. X. Qi, X. Zou, Z. Huang, L. Ren, G. Hao, Y. Liu, X. Wei and J. Zhong, *Applied Surface Science*, 2013, **266**, 332-336.
73. S. Ghosh, B. K. Sarker, A. Chunder, L. Zhai and S. I. Khondaker, *Applied Physics Letters*, 2010, **96**, 163109.
74. S.-K. Chang-Jian, J.-R. Ho, J.-W. J. Cheng and Y.-P. Hsieh, *AIP Advances*, 2012, **2**, 022104.
75. N. Nishimoto, Y. Yamada, Y. Ohnishi, N. Imawaka and K. Yoshino, *physica status solidi (a)*, 2013, **210**, 589-593.
76. D. J. Griffiths, *Introduction to electrodynamics*, Prentice Hall, 1962.
77. J. Paredes, S. Villar-Rodil, A. Martînez-Alonso and J. Tascon, *Langmuir*, 2008, **24**, 10560-10564.
78. X. Zhao, Q. Zhang, D. Chen and P. Lu, *Macromolecules*, 2010, **43**, 2357-2363.
79. Y. Zhang, H.-L. Ma, Q. Zhang, J. Peng, J. Li, M. Zhai and Z.-Z. Yu, *Journal of Materials Chemistry*, 2012, **22**, 13064.
80. Q. Shou, J. Cheng, L. Zhang, B. J. Nelson and X. Zhang, *Journal of Solid State Chemistry*, 2012, **185**, 191-197.
81. L. G. Cancado, A. Jorio, E. H. Ferreira, F. Stavale, C. A. Achete, R. B. Capaz, M. V. Moutinho, A. Lombardo, T. S. Kulmala and A. C. Ferrari, *Nano Lett*, 2011, **11**, 3190-3196.
82. A. C. Ferrari and J. Robertson, *Physical review B*, 2000, **61**, 14095.
83. G. Eda, Y. Y. Lin, C. Mattevi, H. Yamaguchi, H. A. Chen, I. Chen, C. W. Chen and M. Chhowalla, *Advanced materials*, 2010, **22**, 505-509.
84. D. Joung and S. I. Khondaker, *The Journal of Physical Chemistry C*, 2013, **117**, 26776-26782.
85. C. Mattevi, G. Eda, S. Agnoli, S. Miller, K. A. Mkhoyan, O. Celik, D. Mastrogiovanni, G. Granozzi, E. Garfunkel and M. Chhowalla, *Advanced Functional Materials*, 2009, **19**, 2577-2583.
86. S. Kaniyankandy, S. Achary, S. Rawalekar and H. N. Ghosh, *The Journal of Physical Chemistry C*, 2011, **115**, 19110-19116.
87. H. Chang, Z. Sun, Q. Yuan, F. Ding, X. Tao, F. Yan and Z. Zheng, *Advanced Materials*, 2010, **22**, 4872-4876.
88. Y. Shen, S. Yang, P. Zhou, Q. Sun, P. Wang, L. Wan, J. Li, L. Chen, X. Wang and S.

Ding, *Carbon*, 2013, **62**, 157-164.

89. L. G. Cançado, A. Jorio, E. Martins Ferreira, F. Stavale, C. Achete, R. Capaz, M. Moutinho, A. Lombardo, T. Kulmala and A. Ferrari, *Nano letters*, 2011, **11**, 3190-3196.
90. A. C. Ferrari, J. Meyer, V. Scardaci, C. Casiraghi, M. Lazzeri, F. Mauri, S. Piscanec, D. Jiang, K. Novoselov and S. Roth, *Physical review letters*, 2006, **97**, 187401.
91. C. Liu, F. Hao, X. Zhao, Q. Zhao, S. Luo and H. Lin, *Scientific Reports (Nature Publisher Group)*, 2014, **4**, 3965.
92. Z. Yin, S. Wu, X. Zhou, X. Huang, Q. Zhang, F. Boey and H. Zhang, *Small*, 2010, **6**, 307-312.
93. M. Mishra, R. K. Joshi, S. Ojha, D. Kanjilal and T. Mohanty, *The Journal of Physical Chemistry C*, 2013, **117**, 19746-19750.
94. S.-S. Li, K.-H. Tu, C.-C. Lin, C.-W. Chen and M. Chhowalla, *ACS nano*, 2010, **4**, 3169-3174.
95. J. M. Yun, J. S. Yeo, J. Kim, H. G. Jeong, D. Y. Kim, Y. J. Noh, S. S. Kim, B. C. Ku and S. I. Na, *Advanced Materials*, 2011, **23**, 4923-4928.
96. G. Singh, D. Sutar, V. D. Botcha, P. K. Narayanam, S. Talwar, R. Srinivasa and S. Major, *Nanotechnology*, 2013, **24**, 355704.
97. J. P. Clifford, G. Konstantatos, K. W. Johnston, S. Hoogland, L. Levina and E. H. Sargent, *Nature nanotechnology*, 2009, **4**, 40-44.
98. N. Liu, H. Tian, G. Schwartz, J. B.-H. Tok, T.-L. Ren and Z. Bao, *Nano letters*, 2014, **14**, 3702-3708.
99. K. Zheng, F. Meng, L. Jiang, Q. Yan, H. H. Hng and X. Chen, *Small*, 2013, **9**, 2076-2080.
100. K. Eda, *Journal of Applied Physics*, 1978, **49**, 2964-2972.
101. G. Agostinelli, D. L. Bätzner and M. Burgelman, *Thin Solid Films*, 2003, **431-432**, 407-413.
102. S.-H. Cheng, T.-M. Weng, M.-L. Lu, W.-C. Tan, J.-Y. Chen and Y.-F. Chen, *Scientific reports*, 2013, **3**.
103. Z. Sun, Z. Liu, J. Li, G. a. Tai, S. P. Lau and F. Yan, *Advanced materials*, 2012, **24**, 5878-5883.
104. H. Chang, Z. Sun, M. Saito, Q. Yuan, H. Zhang, J. Li, Z. Wang, T. Fujita, F. Ding and Z. Zheng, *ACS nano*, 2013, **7**, 6310-6320.
105. G. Konstantatos, I. Howard, A. Fischer, S. Hoogland, J. Clifford, E. Klem, L. Levina and E. H. Sargent, *Nature*, 2006, **442**, 180-183.
106. M. Hassan, E. Haque, K. R. Reddy, A. I. Minett, J. Chen and V. G. Gomes, *Nanoscale*, 2014, **6**, 11988-11994.
107. X. Li, S. P. Lau, L. Tang, R. Ji and P. Yang, *Journal of Materials Chemistry C*, 2013,

1, 7308-7313.

108. Y. Zhang, C. Wu, X. Zhou, X. Wu, Y. Yang, H. Wu, S. Guo and J. Zhang, *Nanoscale*, 2013, **5**, 1816-1819.
109. D. I. Son, B. W. Kwon, D. H. Park, W.-S. Seo, Y. Yi, B. Angadi, C.-L. Lee and W. K. Choi, *Nature nanotechnology*, 2012, **7**, 465-471.
110. S. H. Song, M. H. Jang, J. Chung, S. H. Jin, B. H. Kim, S. H. Hur, S. Yoo, Y. H. Cho and S. Jeon, *Advanced Optical Materials*, 2014, **2**, 1016-1023.
111. D. H. Wang, J. K. Kim, S. J. Kim, B. H. Hong and J. H. Park, *Nanoscale*, 2014, **6**, 15175-15180.
112. V. Gupta, N. Chaudhary, R. Srivastava, G. D. Sharma, R. Bhardwaj and S. Chand, *Journal of the American Chemical Society*, 2011, **133**, 9960-9963.
113. Z. Huang, Y. Shen, Y. Li, W. Zheng, Y. Xue, C. Qin, B. Zhang, J. Hao and W. Feng, *Nanoscale*, 2014, **6**, 13043-13052.
114. L. Tang, R. Ji, X. Li, G. Bai, C. P. Liu, J. Hao, J. Lin, H. Jiang, K. S. Teng and Z. Yang, *ACS nano*, 2014, **8**, 6312-6320.
115. J. Shen, Y. Zhu, X. Yang, J. Zong, J. Zhang and C. Li, *New Journal of Chemistry*, 2012, **36**, 97-101.
116. H. Tetsuka, R. Asahi, A. Nagoya, K. Okamoto, I. Tajima, R. Ohta and A. Okamoto, *Advanced Materials*, 2012, **24**, 5333-5338.
117. F. Jiang, D. Chen, R. Li, Y. Wang, G. Zhang, S. Li, J. Zheng, N. Huang, Y. Gu and C. Wang, *Nanoscale*, 2013, **5**, 1137-1142.
118. S. Zhu, J. Zhang, S. Tang, C. Qiao, L. Wang, H. Wang, X. Liu, B. Li, Y. Li and W. Yu, *Advanced Functional Materials*, 2012, **22**, 4732-4740.
119. S. H. Jin, D. H. Kim, G. H. Jun, S. H. Hong and S. Jeon, *ACS nano*, 2013, **7**, 1239-1245.
120. C. Luk, B. Chen, K. Teng, L. Tang and S. Lau, *Journal of Materials Chemistry C*, 2014, **2**, 4526-4532.
121. S. K. Lai, C. M. Luk, L. Tang, K. S. Teng and S. P. Lau, *Nanoscale*, 2015, **7**, 5338-5343.
122. L. Tang, R. Ji, X. Li, K. S. Teng and S. P. Lau, *Particle & Particle Systems Characterization*, 2013, **30**, 523-531.
123. C. M. Luk, B. L. Chen, K. S. Teng, L. B. Tang and S. P. Lau, *J. Mater. Chem. C*, 2014, **2**, 4526-4532.
124. Y. Sun, S. R. Wilson and D. I. Schuster, *Journal of the American Chemical Society*, 2001, **123**, 5348-5349.
125. X.-h. Li, B. Wu, J.-e. Huang, J. Zhang, Z.-f. Liu and H.-l. Li, *Carbon*, 2003, **41**, 1670-1673.
126. B. E. Cohen, *Nature*, 2010, **467**, 407-408.

127. Z. Huang, Y. Shen, Y. Li, W. Zheng, Y. Xue, C. Qin, B. Zhang, J. Hao and W. Feng, *Nanoscale*, 2014, **6**, 13043-13052.

128. G. Haider, P. Roy, C.-W. Chiang, W.-C. Tan, Y.-R. Liou, H.-T. Chang, C.-T. Liang, W.-H. Shih and Y.-F. Chen, *Advanced Functional Materials*, 2016, **26**, 620-628.

129. A. Cosmin Obreja, D. Cristea, I. Mihalache, A. Radoi, R. Gavrila, F. Comanescu and C. Kusko, *Applied Physics Letters*, 2014, **105**, 083303.

130. I. Nam, S. Park, G.-P. Kim, J. Park and J. Yi, *Chemical Science*, 2013, **4**, 1663.

131. F. SuongáOu, *Chemical Communications*, 2008, 2373-2375.

132. H. Nakanishi, K. J. Bishop, B. Kowalczyk, A. Nitzan, E. A. Weiss, K. V. Tretiakov, M. M. Apodaca, R. Klajn, J. F. Stoddart and B. A. Grzybowski, *Nature*, 2009, **460**, 371-375.

133. C.-Y. Liu, K. Liang, C.-C. Chang and Y. Tzeng, *Optics express*, 2012, **20**, 22943-22952.

134. X. Wang, K. Maeda, A. Thomas, K. Takanabe, G. Xin, J. M. Carlsson, K. Domen and M. Antonietti, *Nature materials*, 2009, **8**, 76-80.

135. Y. Zhang and M. Antonietti, *Chemistry–An Asian Journal*, 2010, **5**, 1307-1311.

136. Y. Zhang, T. Mori, L. Niu and J. Ye, *Energy & Environmental Science*, 2011, **4**, 4517-4521.

137. J. Xu, M. Shalom, F. Piersimoni, M. Antonietti, D. Neher and T. J. Brenner, *Advanced Optical Materials*, 2015, **3**, 913-917.

138. X. Zhang, X. Xie, H. Wang, J. Zhang, B. Pan and Y. Xie, *Journal of the American Chemical Society*, 2012, **135**, 18-21.

139. W. Guo, S. Xu, Z. Wu, N. Wang, M. Loy and S. Du, *Small*, 2013, **9**, 3031-3036.

140. Y. Zhang, T. Mori, J. Ye and M. Antonietti, *Journal of the American Chemical Society*, 2010, **132**, 6294-6295.

141. P. Guyot-Sionnest, *J Phys Chem Lett*, 2012, **3**, 1169-1175.

142. S. K. Lai, C. Xie, K. S. Teng, Y. Li, F. Tan, F. Yan and S. P. Lau, *Advanced Optical Materials*, 2016, **4**, 555-561.

143. J. Liu, Y. Liu, N. Liu, Y. Han, X. Zhang, H. Huang, Y. Lifshitz, S.-T. Lee, J. Zhong and Z. Kang, *Science*, 2015, **347**, 970-974.

144. G. Algara-Siller, N. Severin, S. Y. Chong, T. Björkman, R. G. Palgrave, A. Laybourn, M. Antonietti, Y. Z. Khimyak, A. V. Krasheninnikov and J. P. Rabe, *Angewandte Chemie*, 2014, **126**, 7580-7585.

145. D. Gao, Q. Xu, J. Zhang, Z. Yang, M. Si, Z. Yan and D. Xue, *Nanoscale*, 2014, **6**, 2577-2581.

146. H. Xu, J. Yan, X. She, L. Xu, J. Xia, Y. Xu, Y. Song, L. Huang and H. Li, *Nanoscale*, 2014, **6**, 1406-1415.

147. W. Ho, Z. Zhang, W. Lin, S. Huang, X. Zhang, X. Wang and Y. Huang, *ACS applied*

materials & interfaces, 2015, **7**, 5497-5505.

148. S. Yang, Y. Gong, J. Zhang, L. Zhan, L. Ma, Z. Fang, R. Vajtai, X. Wang and P. M. Ajayan, *Advanced materials*, 2013, **25**, 2452-2456.
149. R. Saran, M. N. Nordin and R. J. Curry, *Advanced Functional Materials*, 2013, **23**, 4149-4155.
150. L. Peng, L. Hu and X. Fang, *Advanced Functional Materials*, 2014, **24**, 2591-2610.
151. A. Du, S. Sanvito, Z. Li, D. Wang, Y. Jiao, T. Liao, Q. Sun, Y. H. Ng, Z. Zhu and R. Amal, *Journal of the American Chemical Society*, 2012, **134**, 4393-4397.
152. X. Li, Y. Dai, Y. Ma, S. Han and B. Huang, *Physical Chemistry Chemical Physics*, 2014, **16**, 4230-4235.
153. R. Wang, L. Gu, J. Zhou, X. Liu, F. Teng, C. Li, Y. Shen and Y. Yuan, *Advanced Materials Interfaces*, 2015, **2**.
154. Y. Y. Hui, G. a. Tai, Z. Sun, Z. Xu, N. Wang, F. Yan and S. P. Lau, *Nanoscale*, 2012, **4**, 3118-3122.
155. J. Chen, S. Shen, P. Guo, P. Wu and L. Guo, *Journal of Materials Chemistry A*, 2014, **2**, 4605-4612.
156. Y.-J. Yu, Y. Zhao, S. Ryu, L. E. Brus, K. S. Kim and P. Kim, *Nano letters*, 2009, **9**, 3430-3434.
157. F. Liu and S. Kar, *ACS nano*, 2014, **8**, 10270-10279.
158. Y. Lee, J. Kwon, E. Hwang, C. H. Ra, W. J. Yoo, J. H. Ahn, J. H. Park and J. H. Cho, *Advanced materials*, 2015, **27**, 41-46.
159. P. Wu, J. Wang, J. Zhao, L. Guo and F. E. Osterloh, *Journal of Materials Chemistry A*, 2014, **2**, 20338-20344.
160. G. Konstantatos, M. Badioli, L. Gaudreau, J. Osmond, M. Bernechea, F. P. G. De Arquer, F. Gatti and F. H. Koppens, *Nature nanotechnology*, 2012, **7**, 363-368.
161. M. S. Marcus, J. M. Simmons, O. M. Castellini, R. J. Hamers and M. A. Eriksson, *Journal of Applied Physics*, 2006, **100**, 084306.
162. C. Biswas, F. Güneş, D. D. Loc, S. C. Lim, M. S. Jeong, D. Pribat and Y. H. Lee, *Nano letters*, 2011, **11**, 4682-4687.
163. K. Roy, M. Padmanabhan, S. Goswami, T. P. Sai, G. Ramalingam, S. Raghavan and A. Ghosh, *Nature nanotechnology*, 2013, **8**, 826-830.
164. B. Y. Zhang, T. Liu, B. Meng, X. Li, G. Liang, X. Hu and Q. J. Wang, *Nat Commun*, 2013, **4**, 1811.